# SYNERGISTIC EFFECTS OF $B_4C$ AND ZnO NANOMATERIALS AS ELECTRODES FOR SUPERCAPACITORS

by

MERVE AKTÜRK

Submitted to the Graduate School of Engineering and Natural Sciences
in partial fulfillment of the requirements for the degree of
Doctor of Philosophy

Sabancı University
July 2022

# SYNERGISTIC EFFECTS OF $B_4C$ AND ZnO NANOMATERIALS AS ELECTRODES FOR SUPERCAPACITORS

Approved by:

Date of Approval: July 26, 2022

# ABSTRACT

## SYNERGISTIC EFFECTS OF $B_4C$ AND ZnO NANOMATERIALS AS ELECTRODES FOR SUPERCAPACITORS

MERVE AKTÜRK

Materials Science and Nanoengineering Ph.D. Dissertation, July 2022

Dissertation Supervisor: Assoc. Prof. Emre Erdem

Keywords: boron carbide, zinc oxide, electron paramagnetic resonance, point defects, supercapacitors, energy storage systems.

Boron carbide ($B_4C$) is one of the world's hardest bulk materials with excellent stability in extreme chemical and thermal conditions. Despite its discovery in the 19th century and numerous studies since 1930s, its atomic structure, electronic properties and electrochemical behavior are yet one of the most debated topics among chemists, physicists and materials scientists. The difficulty in distinguishing the absolute accurate atomic positions with common characterization techniques is mainly due to the very close similarity of the scattering cross-sections of $^{11}B$ and $^{12}C$, and the point defects formed within the crystal which affects the atomic arrangements and the charge densities in the elementary cells. Similarly, significant efforts have been devoted to reveal the unique electronic, optical, structural and magnetic properties of zinc oxide (ZnO) which is an n-type semiconductor and has been used in various applications including energy storage devices, particularly supercapacitors (SCs). The development of efficient and long-life electrodes from sustainable materials for SCs is of the utmost importance to satisfy the increasing energy demands. In this Ph.D. dissertation, $B_4C$ and ZnO were selected as electrodes for SCs due to their interesting defective properties that contribute to the enhanced capacitive performances by modifying their electronic and atomic structure. First, modified sol-gel synthesis of $B_4C$ nanostructures from aqueous solutions of B and C sources was described. The pure $B_4C$ phase was obtained by the heat treatment at temperatures $\leq$1500 °C which is lower than the conventional sintering temperatures ($\geq$ 2000 °C). Then, extensive thermal and microstructural characterizations were carried out to reveal the crystal structure, lattice parameters, mean particle size, and the microstructure of the synthesized $B_4C$ powders. Complementary X- and Q-band EPR analyses of defect centers in $B_4C$ and ZnO were performed to reveal the effects of intrinsic defects on the electrochemical performance of the SCs. The synthesized $B_4C$ and ZnO were

assembled in a custom-made all-in-one supercapacitor device, and their synergistic effects on the electrochemical performance was investigated by CV, EIS, and GCPL techniques.

# ÖZET

## $B_4C$ VE ZnO NANOMALZEMELERİNİN SİNERJİK ETKİLERİ VE SÜPERKAPASİTÖR ELEKTROTLARI OLARAK KULLANIMI

MERVE AKTÜRK

Malzeme Bilimi ve Nanomühendislik, Doktora Tezi, Temmuz 2022

Tez Danışmanı: Doç. Dr. Emre Erdem

Anahtar kelimeler: Bor karbür, çinko oksit, elektron paramanyetik rezonans, noktasal kusurlar, süperkapasitörler, enerji depolama sistemleri.

Bor karbür ($B_4C$), aşırı kimyasal ve termal koşullarda mükemmel kararlılığa sahip olup, dünyanın en yüksek sertlik değerine sahip malzemelerinden biridir. 19. yy.'da keşfedilmiş olmasına ve 1930'lardan bu yana çok sayıda çalışmaya konu edilmesine rağmen, bor karbürün atomik yapısı, elektronik özellikleri ve elektrokimyasal davranışı halen kimyagerler, fizikçiler ve malzeme bilimciler arasında en çok tartışılan konular arasındadır. $B_4C$ yapısındaki atomik pozisyonların alışılagelmiş yöntemler kullanılarak kesin doğrulukla ayırt edilememesindeki zorlukların başlıca sebepleri; $^{11}B$ ve $^{12}C$ atomlarının saçılma tesir kesitlerinin oldukça birbirlerine yakın değerlerde olması ve kristal içerisinde temel hücrelerdeki yük yoğunluğunu ve atomik pozisyonları etkileyen noktasal kusurların oluşmasıdır. Benzer çabalar bir n-tipi yarı iletken olan ve enerji depolama araçları (bilhassa süperkapasitörler) dahil olmak üzere birçok uygulamada kullanılmakta olan çinko oksit (ZnO) malzemesinin kendine has elektronik, optik, yapısal ve manyetik özelliklerinin ortaya koyulması için de harcanmıştır.

Süperkapasitörler için verimli ve uzun ömürlü elektrotların sürdürülebilir malzemeler kullanılarak geliştirilmesi artan enerji talebinin karşılanması açısından oldukça yüksek öneme sahiptir. Bu doktora tezinde elektrot malzemeleri olarak $B_4C$ ve ZnO seçilmesinin başlıca nedeni bu malzemelerin elektronik ve atomik yapılarında değişikliğe sebep olan ve böylece iyileştirilmiş kapasitif performanslara ulaşmalarını sağlayan ilgi çekici kusur özelliklerine sahip olmalarıdır. İlk olarak $B_4C$ nanoyapılarının B ve C kaynağı olarak hazırlanan sulu çözeltilerden modifiye sol-jel yöntemi ile sentezi açıklanmıştır. Saf $B_4C$ fazı geleneksel $B_4C$ üretim sıcaklıklarından (≥ 2000 °C) daha düşük olan 1500 °C veya daha düşük sıcaklıklarda ısıl işlem ile üretilmiştir. Ardından, sentezlenen $B_4C$ tozların kristal yapılarının, kafes parametrelerinin, ortalama tane boyutlarının ve mikroyapısal özelliklerinin

ortaya koyulması amacı ile kapsamlı termal ve mikroyapısal karakterizasyon çalışmaları gerçekleştirilmiştir. $B_4C$ ve ZnO yapısındaki özgün (tabii) kusurların süperkapasitörlerin elektrokimyasal performansları üzerine olan etkisinin ortaya koyulması amacı ile tamamlayıcı X ve Q-bant EPR analizleri yapılmıştır. Sentezlenen $B_4C$ ve ZnO tozları özel yapım (all-in-one) süperkapasitörlere montajlanmış ve iki elektrodun sinerjik etkilerinin elektrokimyasal performans üzerine etkileri CV, EIS ve GCPL teknikleri kullanılarak araştırılmıştır.

# Acknowledgements

It was so hard and challenging journey, but I loved every moment of it, especially the part of getting our research published in the prestigious scientific journals which was so rewarding after all that hard work and is the best opportunity to share our knowledge with scientist all over the world. I would like to take this opportunity to express my sincere gratitude to everyone who advised, encouraged, motivated, supported and helped me along the way.

First, I would like to express my sincere gratitude to my supervisor, my Doktorvater Prof. Emre Erdem, who supported me at every step of my journey, shared his knowledge and experiences, and taught me how to be a good scientist with a strong work ethic. He was so kind and patient throughout this journey and was available whenever I needed his professional guidance. I know that our collaboration will continue forever.

I would also like to thank to my dissertation committee members Assist. Prof. Feray Bakan Mısırlıoğlu, Prof. Ebru Menşur Alkoy, Prof. Mustafa TUNCER and Prof. Nurdan Demirci Sankır for their insightful comments and constructive feedback to improve my research.

I am very grateful to the faculty members of Sabancı University Materials Science and Nanoengineering Program who have inspired me with their teaching and improved my academic qualifications. Special thanks to Prof. Cleva Ow-Yang, Prof. Selmiye Alkan Gürsel, Prof. Burç Mısırlıoğlu and Prof. Mehmet Ali Gülgün: I sincerely appreciate your efforts in supporting those who need your professional guidance along the way. I also thank to Prof. Ersin Göğüş for all his valuable comments and discussions we had.

My sincere thanks go to my fellows İpek Deniz Yıldırım, Ameen Uddin Ammar, and Mohamad Hasan Aleinawi for their help and assistance in the lab and for being such a great research group.

Many thanks to our previous FENS laboratory specialist Dr. Nursel Karakaya, and current lab specialists Bilge Esenkal and Anıl Tez for their help in the laboratories.

I also thank Prof. Cengiz Kaya for his support in the beginning of my doctoral studies.

I would like to extend my sincere thanks to all our collaborators with whom we have shared experiences and carried out many projects. A big thank you to Dr. Arpad Mihai Rostas for

his help with the UV-light and temperature dependent EPR, Q-band EPR measurements and for all the insightful and cheerful discussions we had which I benefited a lot. I would also like to thank to Behzat Alperen Çimen and Ferhan Can from the Turkish Energy, Nuclear and Mineral Research Agency-Nuclear Energy Research Institute for help with high temperature DTA/TGA analysis of boron carbide samples.

“A journey is best measured in friends, rather than miles.” Tim Cahill said. I couldn’t agree more. It was my friends Dr. Arzu Coşgun Ergene, Mervenaz Şahin, Lyn Zemberekçi and Wael Ali Saeed Aldulaimi who turned this journey into an adventure. I appreciate all the fruitful discussions, all the good memories we collected, and the joyful times we spent together. I am so lucky knowing you. Arzu deserves a special thank you because we went through all those hard times together; we laughed, we tried, we challenged, we cried, we planned, and look, we did it!

I would like to thank TUBITAK for funding my work in the project “Defect-induced electrode materials for the design of battery like supercapacitor devices: SUPERBATS” under the grant number of 118C243.

Finally, I deeply appreciate the constant support of my family. My beloved mom, the most precious woman in my life, thank you for your unconditional love and support throughout my life, and all the efforts to raise me as a decent person and an independent, confident, strong woman. And my husband, my forever soulmate Emre, I cannot express my feelings enough about your patience during the most difficult times and sleepless nights, and all the days we spent apart due to my busy schedule during all this time. I love you.

As this chapter of my life comes to a close, I know that there are many more yet to be written.

*to my beloved mother Raziye Say,*
*and my forever soulmate Emre Aktürk*

# TABLE OF CONTENTS

# LIST OF TABLES

# LIST OF FIGURES

# LIST OF SYMBOLS AND ABBREVIATIONS

SC: Supercapacitor
EDLC: Electric Double Layer Capacitor
CNT: Carbon nanotubes
DI: Deionized water
MBA: Mannitol-to-boric acid molar ratio
HEBM: High-energy ball milling
BPR: Ball-to-powder weight ratio
XRD: X-ray diffraction
ICSD: Inorganic Crystal Structure Database
CIF: Crystallographic information file
COD: Crystallography Open Database
FTIR: Fourier Transform Infrared Spectroscopy
ATR: Attenuated Total Reflectance
SEM: Scanning Electron Microscopy
EDX: Energy-Dispersive X-ray Spectroscopy
SE: Secondary electron
BSE: Backscattered electron
FE-SEM: Field Emission Scanning Electron Microscope
FEG: Field Emission Gun
DTA: Differential Thermal Analysis
TGA: Thermogravimetric Analysis
PL: Photoluminescence
PLE: Photoluminescence Excitation
EPR: Electron Paramagnetic Spectroscopy
ESR: Electron Spin Resonance
PDF: Portable Document Format
UV: Ultraviolet
CV: Cyclic Voltammetry
PEIS: Potentiostatic Electrochemical Impedance Spectroscopy
EIS: Electrochemical Impedance Spectroscopy
GCPL: Galvanostatic Cycling With Potential Limitation

GCD: Galvanostatic Charge/Discharge
EC/DEC: Ethylene Carbonate/Diethyl Carbonate
SC: Supercapacitor
ASC: Asymmetric supercapacitor
CPE: Constant Phase Element

# CHAPTER 1. GENERAL INTRODUCTION

Increase in population hence the consumption of energy by human activities resulting in rising demand for energy in all industrial sectors as well as in all aspects of everyday life. In addition to the rapid population growth and its economic consequences, increased rate of industrialization, the global climate change and the severe damage of air pollutants both on environment and public health caused by the combustion of fossil fuels brought an immediate need for the development of efficient renewable and sustainable energy sources and storage systems [1-5] .

Supercapacitors (SCs) and batteries have attracted great interest in recent decades as promising solutions for the energy storage problem [6-8]. SCs differ from batteries in terms of their charge storage mechanism. This difference arises from the electrochemical processes involved in the charge storage. In electric double layer capacitors (EDLCs), the electrostatic charge storage occurs at the surface of the electrodes by adsorption of the electrolyte ions, and no diffusion-controlled process is involved. In batteries, the process is based on the diffusion of $Li^+$ in the bulk electrode material which takes longer time for the process to occur, thus causes slower response times. Consequently, SCs exhibit much higher power density, longer cycle life and considerably faster response times when compared to batteries [9-12]. These properties are particularly crucial in applications where rapid power delivery and recharging are of primary importance, such as in portable electronic devices, electrical vehicles, space shuttles, and solar cells. [13, 14]. The utmost importance of providing the required amount of energy instantly at low-cost without the need of any additional conversion step has triggered an enormous number of research activities toward SCs. However, SCs, especially EDLC, have lower energy density when compared to batteries because the charge storage is limited to the electrode surface.

Development of high-performance materials with improved capacitive behavior for SC applications are of great interest. In present, there are more than 300,000 publications on Google Scholar for the keyword of “supercapacitors”, and the number reaches almost 3.5 million for the keyword of “capacitor”. Although the energy density of SCs is higher than the conventional capacitors, it is considerably poor compared to most rechargeable batteries, which makes it the main drawback of SC devices. The development of new device configurations with novel nanostructured electrode materials and employment of various operation parameters play a critical role to increase the overall performance of the SCs including the energy density, specific capacity, capacitance retention and coulombic efficiency [15-17].

Carbon materials are most widely used electrode materials for SCs due to their high porosity, (especially open pores), high surface area, high electronic conductivity, high capacitance, low cost and availability in different forms such as composites, foams, powders, fibers, aerogels, nanotubes, foils etc. [18]. Most of the carbon materials contain open pores in their structure that are accessible to the electrolyte ions. The significantly high specific surface area of highly porous carbon electrodes make them capable of holding increased number of charges at the electrode-electrolyte interface by forming an electrochemical double layer, leading to an increased energy storage performance. This non-Faradaic charge storage mechanism, also known as EDLC, is characteristic of carbon electrodes. Most widely used carbon-based electrodes are made of active carbon, graphene, graphite, carbon dots and carbon nanotubes (CNTs) [19-24].

Metal oxides and carbides are well-known pseudocapacitors with Faradaic charge storage mechanism in which rapid near-surface or surface reversible redox reactions lead to an increase in the charge storage. Even though they have some drawbacks like poor conductivity, uncontrollable ion diffusion and volume expansion in the bulk phase, they deliver considerably fast charge-discharge responses, high capacitance with high energy at a low current density without sacrificing power density when electro-active sites or defects are introduced into the structure [25]. Among metal oxides, ZnO, which is an n-type wide-bandgap (~3.2-3.3 eV) semiconductor with wurtzite crystal structure, has regained increased attention and recognized as a promising material for its use in electronics and energy storage applications due to its unique and multifunctional properties in nanoscale, including its pseudocapacitive behavior with sufficient theoretical capacity, defective structure, high chemical and thermal stability, n-type semiconductivity, tunable morphology, abundance, and high Li ion diffusion coefficient [26-47]. Conceivably, there are five types of point defects that occur in ZnO: 1) zinc vacancies ($V_{Zn}$), 2) zinc interstitials ($Zn_i$), 3) oxygen vacancies ($V_O$), 4) oxygen interstitials ($O_i$), and 5) hydrogen shallow donors ($H_O$). All these defects contribute to the properties of ZnO by modifying the electronic and crystal structure and play a vital role on its electronic, electrical and optical properties [48, 49]. Therefore, being able to introduce defects in ZnO structure at nanoscale and understanding the defect formation mechanism as well as the kind of defect centers are very critical and challenging in the development of efficient energy storage systems [50, 51]. Illustrations of possible defects in ZnO are presented in Fig. 1 and Fig. 2 [26].

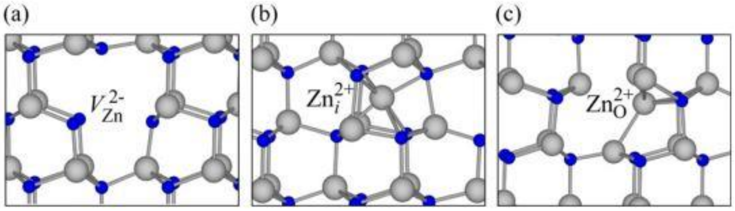

Figure 1. Calculated local atomic geometry for (a) the Zn vacancy in the −2 charge state ($V_{Zn}^{2-}$; (b) the zinc interstitial in the +2 charge state ($Zn_i^{2+}$). (c) Calculated local atomic geometry of the zinc antisite in the +2 charge state ($Zn_O^{2+}$). (Reprinted from [26] with permission of the IOP Publishing.)

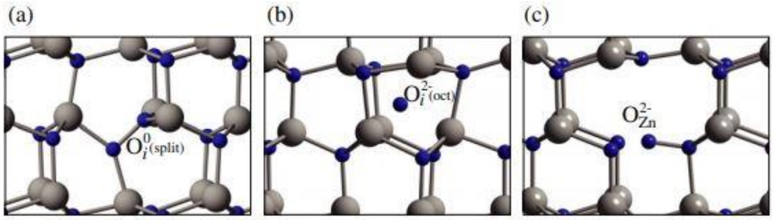

Figure 2. Local atomic geometries for (a) oxygen interstitial in the split-interstitial configuration $O_i^0$ (split); (b) oxygen interstitial in the octahedral configuration $O_i^{2-}$ (oct); (c) oxygen antisite $O_{Zn}^{2-}$, showing a large displacement off the substitutional site. (Reprinted from [26] with permission of the IOP Publishing.)

The crystal structure of $B_4C$ is still one of the most debated issues in terms of exact site occupancies by boron (B) and carbon (C) atoms. It has a rhombohedral structure consists of 15 atoms per elementary cell consisting of a linear chain of three atoms (or atoms and vacancies) at the center (C-C-C, C-B-C or C-B-B) that links a slightly distorted 12-atom icosahedra of $B_{12}$, $B_{11}C$ or $B_{10}C_2$ located at the corners of the structure as suggested by the available experimental and computational data (Fig. 3) [52-55].

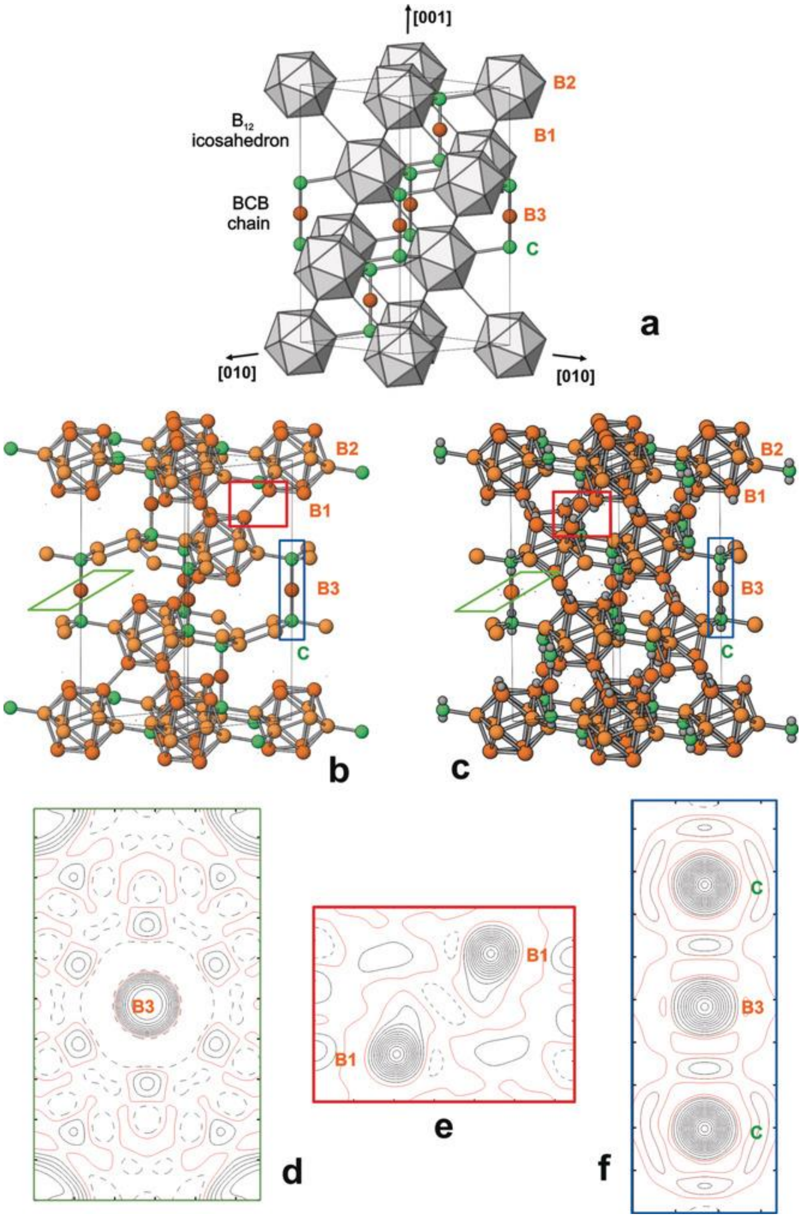

Figure 3. Crystal structure of boron carbide: a) general arrangement of the icosahedrons ($B_{12}$) and interconnecting chains (CBC) in the structure. b) Atomic arrangement in the ideal structural motif $B_{13}C_2$. c) Positions of the maxima of the difference ED after refinement of the ideal model (gray spheres). d)–f) Difference ED in the selected regions of the crystal structure revealing local deviations from the ideal model: d) in the (002) plane (z=0.5) crossing the B3 atom, revealing the positions of boron in bent CBC chains or in rhombic CB2C; e) in vicinity of the B1 atoms, visualizing the boron-by-carbon substitution in the $B_{12}$ icosahedron; f) in the CBC chain. The shortest B−B and B−C distances are shown with gray lines (a–c); the scale step is 0.5 Å, blue isolines reveal the positive values, the red line shows the zero value (d–f). (Reprinted from [53] with permission of the John Wiley and Sons.)

The primary aim of this dissertation is to develop novel symmetric and/or asymmetric all-in-one supercapacitor devices comprising boron carbide ($B_4C$) and zinc oxide (ZnO) based electrode materials to reveal their synergistic effects on the SC performance. Basically, there are three main types of SCs namely pseudocapacitors, battery-like (or hybrid), and electric double layer capacitors (EDLC) [11, 17, 56]. The working mechanism of SCs is highly dependent on the device design, the type of electrode materials (dielectrics (i.e., ceramics), polymeric materials, metal-ion doped materials, semiconductors etc.), morphology, crystal size and defect structures [57]. In this dissertation, $B_4C$ and ZnO have been selected due to their interesting defective and capacitive properties [28, 58-60]. Point defects in $B_4C$ are among the most debated issues so far, as it is the case for ZnO [61-71]. Recent studies showed that semiconductor ZnO nanocrystals exhibit hybrid SC mechanism due to their intrinsic defects [32]. On the other hand, $B_4C$ is recognized as the third hardest material known to date after diamond and cubic boron nitride, in fact, it is the hardest material produced in tonnage quantities for commercial applications [52, 72]. Its use is generally in the form of sintered bulk compacts or composite plates in nuclear, ballistic, abrasives, nozzles and refractory applications due to its excellent thermal, mechanical, chemical and thermoelectric properties, as well as high neutron absorption cross-section [73-75]. The use of $B_4C$ as an energy storage material is not common. In fact, most of the studies investigating its defective structure are based on modelling or ab initio calculations [76, 77]. Even though there are a few studies in literature on its use in electronics and energy applications, there is very limited information regarding its use as an electrode material for SCs [60, 78]. In the light of these facts, defect structure investigation and smart way of SC design with $B_4C$ and ZnO materials should be thoroughly investigated which are the main motivations of this thesis. The goal is to obtain durable and thermally stable high performance SC devices by knowing the electronic and optical properties of its constituent electrodes. Such goal can only be reached by the advanced characterization as well as facile and green synthesis techniques and modelling of materials characteristics. A correlation of defect structures with the electrochemical performance is beneficial for not only for the energy storage industry, but also necessary for the research on the development of advanced materials for similar applications. Finally, it is worth to mention that very little is known on the semiconductor properties of $B_4C$, especially from the point of view of empirical research, whereas semiconductor properties of ZnO are quite well known.

To the best of our knowledge, these two opposite types (p- and n-type for $B_4C$ and ZnO, respectively) semiconductor materials have not yet been used together and reported as electrode materials in a SC device so far. Therefore, the results of this study are expected to significantly contribute to the literature in the development of semiconductor model of $B_4C$, as well as to design novel combinations of electrode materials containing $B_4C$ and ZnO nanomaterials.

# CHAPTER 2. BORON CARBIDE AND ZINC OXIDE NANOMATERIALS AS ELECTRODES FOR SUPERCAPACITORS

## 2.1. Synthesis of Boron Carbide as an Electrode Material for Supercapacitors

### 2.1.1. Materials

Boric acid ($H_3BO_3$) and D(-)mannitol ($C_6H_{14}O_6$) were chosen as boron and carbon sources, respectively. Both chemicals were purchased from Merck and used as received. Deionized (DI) water was used as a solvent to prepare precursor solutions.

### 2.1.2. Sol-gel derived synthesis of boron carbide precursors

Boron carbide ($B_4C$) powder was synthesized from a precursor solution containing aqueous solutions of boric acid ($H_3BO_3$, denoted as BA) and D(-)mannitol ($C_6H_{14}O_6$, denoted as M) at different molar ratios given in Table 1. The precursor solution was prepared via a modified sol-gel process through the dehydration and condensation reactions of $H_3BO_3$ and $C_6H_{14}O_6$ by modifying a previously reported synthesis route by Kakiage et al [79]. A schematic of the process is given in Fig. 4. In a typical synthesis procedure, separate aqueous solutions of $H_3BO_3$ and $C_6H_{14}O_6$ were prepared by dissolving the required amounts of starting materials (see Table 1) in DI water and maintaining the solution temperature at 80 ℃ under continuous stirring at 320 rpm for 30 min. When the solutions become clear without any suspended or precipitated particles, the $C_6H_{14}O_6$ solution was slowly mixed with the $H_3BO_3$ solution with constant stirring at controlled temperature (Fig. 5(a)). Then, the excess water was evaporated by maintaining the temperature at 110-120 ℃ at the same stirring rate (Fig. 5(b)). Finally, an opaque gel-like condensed matter is obtained, collected in a watch glass, and dried in a vacuum oven (max. pressure: $2.5 \times 10^{-5}$ bar) at 110 ℃ for 3-4 hours (Fig. 6(a)). The dried condensed product were carefully crushed by a hammer, and then ground in an agate mortar to separate agglomerated particles, as well as to obtain homogeneously distributed powders before heat treatment (Fig. 6(b)).

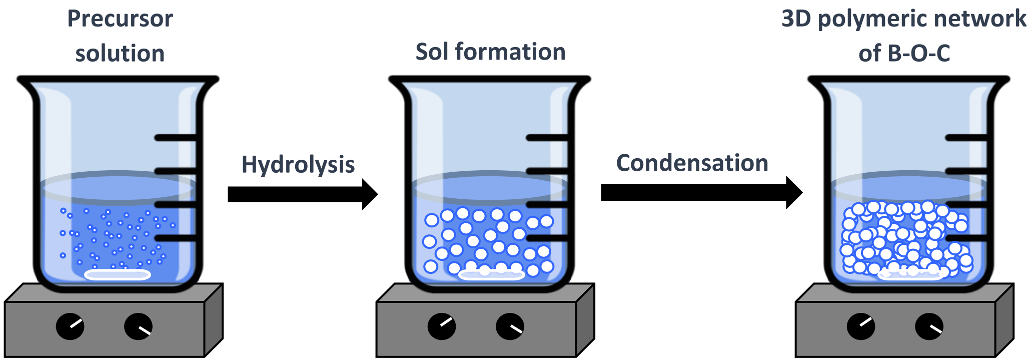

Figure 4. Schematic illustration of the synthesis procedure of $B_4C$ precursors (B-O-C networks).

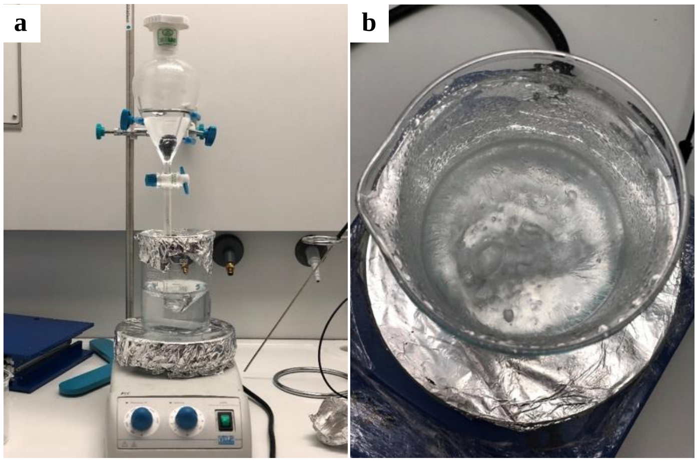

Figure 5. (a) Experimental setup of modified sol-gel synthesis of $B_4C$ precursor, and (b) solution at the beginning of the condensation step.

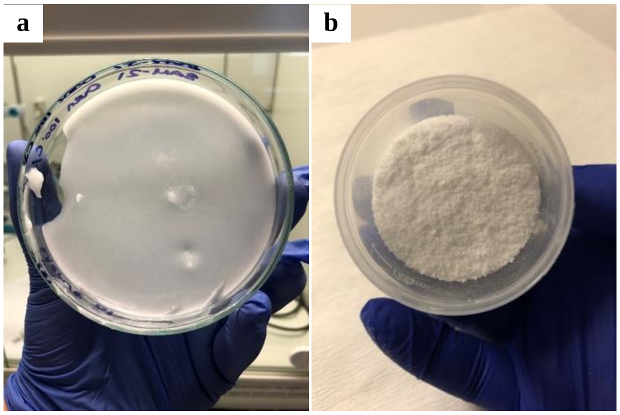

Figure 6. Condensed MBA14 precursor: (a) wet (before drying), (b) dried and ground.

Table 1. Synthesis conditions and composition design parameters to produce $B_4C$ powders from mannitol and boric acid.

| **Composition Code** | | **Starting Materials** | | **Compositions** | | | **Calcination Conditions**[#] | | | **Heat Treatment (Sintering) Conditions** | | | |
|---|---|---|---|---|---|---|---|---|---|---|---|---|---|
| | | **Carbon Source** | **Boron Source** | **Molar Ratio** | | **$C/B_2O_3$** | **T1 (°C)** | **Time (h)** | **Heating rate (°C/min)** | **T2 (°C)** | **Time (h)** | **Heating rate (°C/min)** | **Atmosphere** |
| | | | | **C source** | **B source** | | | | | | | | |
| **MBA** | **MBA14** | D(-)-Mannitol (M) ($C_6H_{14}O_6$) | Boric Acid (BA) ($H_3BO_3$) | 1 | 4 | 3 | 400-500 | 2 | 5 | 1400-1500 | 5 | 10 | Ar |
| | **MBA13.5** | | | 1 | 3.44 | 3.5* | 400-500 | 2 | 5 | 1400-1500 | 5 | 10 | Ar |
| | **MBA12** | | | 1 | 2 | 6 | 400-500 | 2 | 5 | 1400-1500 | 5 | 10 | Ar |

[#] All calcination studies were conducted in air atmosphere.
*Stoichiometric ratio.

### 2.1.3. Heat treatment of boron carbide

The dried and ground powder precursors were placed in alumina crucibles and calcined at 500 °C for 2 h at a heating rate of 5 °C/min in air to remove water and the excess carbon contents. Then, each calcined black sample was ground in an agate mortar for 10 minutes before subsequent thermal treatment. The ground black powder was then placed in a graphite crucible with dimensions 100x40x20 mm and subjected to a heat treatment at 1400 and 1500 °C with a dwell time of 5 h and a heating rate of 10 °C/min in flowing Ar atmosphere (200 ml/min) to produce crystalline $B_4C$ as a final product. The inner surface of the graphite crucible was covered with a graphite foil of 0.5 mm thickness to avoid contact between sample and the crucible and to ease the removal of sintered product from the crucible. The images of the samples before and after heat treatment are shown in Fig. 7. A tubular horizontal furnace (Protherm PTF 16/75/450) equipped with SiC heating elements was used with a ceramic working tube made of high-purity alumina (Alsint, 99.7 % $Al_2O_3$) with an inner diameter of 75 mm and length of 1000 mm for the thermal treatment of the calcined $B_4C$ precursors. For the sample codes listed in Table 1, the letters M and BA refer to the starting materials mannitol and boric acid, respectively, and the numbers correspond to the molar ratio of mannitol-to-boric acid except for MBA13.5 where 1:3.5 corresponds to the stoichiometric ratio of $C/B_2O_3$.

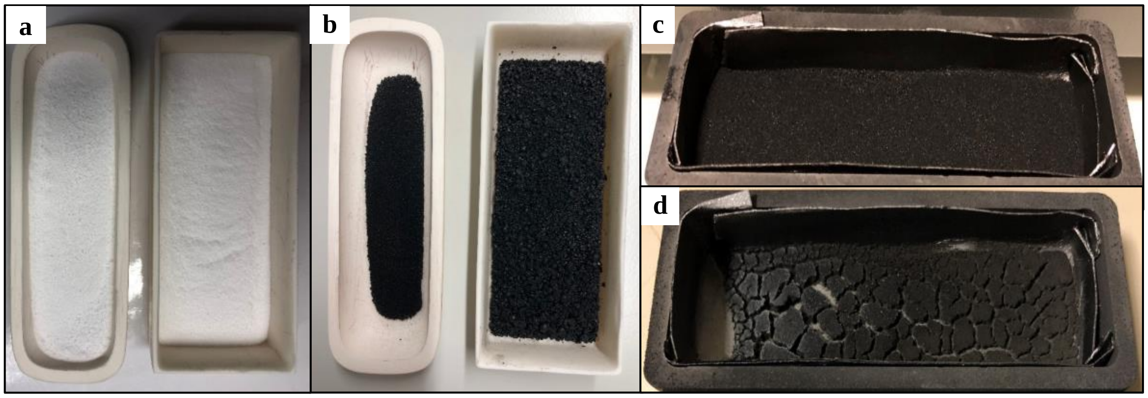

Figure 7. Synthesized MBA14 precursors (a) before and (b) after calcination at 500°C in alumina crucibles, (c) before and (d) after heat treatment at 1500°C in graphite crucibles with graphite foils.

### 2.1.4. High-energy ball milling of boron carbide

Crystalline powders of synthesized boron carbide were mechanically milled to investigate the effects of milling on the paramagnetic properties of boron carbide by introducing surface defects by the mechanical strain produced through high energy ball milling process. A high-energy planetary ball milling (HEBM) equipment (Fritsch, Pulverisette 7 Premium Line Planetary Micro Mill) was employed at room temperature with zirconia vial and balls at following conditions: milling times of 20 and 30 min, rotation speed of 500 rpm, Ø 2 mm zirconia balls, 45 ml zirconia vial, ball-to-powder weight ratio (BPR) of 13:1.

## 2.2. Zinc Oxide (ZnO) Nanocrystals as Electrode Materials for Supercapacitors

ZnO nanocrystals were obtained from high-purity commercial ZnO powder (bulk) (purity: 99.9 %, Sigma-Aldrich) with an average particle size of 100 μm by dry milling via the HEBM at room temperature without using any additives or any liquid milling medium. The starting powders were milled for 30 min at 500 rpm for 4 cycles for the sample ZnO-2h, and for 8 cycles for the sample ZnO-4h, respectively, with 3 min of rest between each cycle. A 45 ml zirconia vial was used with 5 zirconia balls (Ø=10 mm) with a BPR of 15.

# CHAPTER 3. CHARACTERIZATION METHODS

## 3.1. Microstructural Characterization Methods

### 3.1.1. X-ray diffraction (XRD)

X-ray diffraction is a non-destructive method for structural characterization of various types of crystalline solid materials including metals, ceramics, and polymers using constructive interference described by Bragg's law [80]. It is used both for the qualitative analysis, that is, to identify the phases and the lattice parameters of the crystalline material where the exact composition is not known, and for the quantitative analysis which enables us to calculate the percentage of crystallinity, the strain and the relative proportion of the phases in the subjected material.

In this dissertation, the XRD measurements were performed to identify the phases present in each sample, to determine the corresponding lattice parameters, and to calculate the percentage crystallinity of the subjected material. The XRD patterns of the synthesized powders were obtained at ambient conditions using a Bruker D2 Phaser X-ray diffractometer over a $2\theta$ range of 5-90$^{o}$ at a step size of 0.02 $s^{-1}$ with Cu-K$\alpha$ radiation ($\lambda$ = 1.540 Å) at 30 kV and 10 mA. The identification of the crystalline phases was carried out using the DIFFRAC.EVA software V4.2 (Bruker) and matched with the Inorganic Crystal Structure Database (ICSD, FIZ Karlsruhe 2019, version 4.2.0). Rietveld refinements on the powder X-ray diffraction (XRD) data were performed using jEdit (ver. 4.3.1) and TOPAS-Academic V5 software packages from Bruker. Crystallographic information file (CIF) of the identified phase was obtained from Crystallography Open Database (COD).

### 3.1.2. Raman Spectroscopy

Raman spectroscopy is a vibrational spectroscopic technique based on the light-matter interaction and the change in polarizability of a molecule during its vibrational motion. In this technique, a target molecule is excited by focusing a high-intensity laser beam on it, and induced dipole moments are created due to the interaction of the incident light with the vibration modes of the target molecule. This results in inelastic scattering of light from the molecule, known as Raman scattering, provides a unique chemical and structural information about the target molecule that is characteristic for each molecular system, therefore represents a fingerprint of the molecule. Raman spectroscopy is applied for the quantitative and qualitative analyses of various types of organic, inorganic, and biological molecules.

In this dissertation, Raman spectroscopy was used to investigate the effects of different mannitol to boric acid molar ratios and different heat treatment temperatures on material's defect structure, especially in terms of the presence of D- and G-bands. Raman spectroscopy measurements were carried out using a Renishaw inVia Raman spectrometer with a 532 nm green laser excitation. The analyses were performed at ambient conditions.

### 3.1.3. Fourier Transform Infrared Spectroscopy (FTIR)

Fourier transform infrared spectroscopy (FTIR) is very similar to Raman spectroscopy, but it utilizes the absorption of light by the target molecules at frequencies that match the vibrational frequencies of their chemical bonds. These frequencies are characteristic for every molecule, that is, each molecular bond vibrates at certain frequencies, and is called IR-active if a change occurs in its dipole moment upon absorption of the incident light. FTIR enables us to track the changes in the molecular structure, i.e., formation or elimination of a particular functional group, throughout the synthesis of materials.

In this work, a Thermo Scientific Nicolet iS10 FTIR spectrometer with ATR (Attenuated Total Reflectance) is used to track the formation of the dichelate complexes, i.e., B-O-C bonds arising from complexation reaction between mannitol and boric acid.

### 3.1.4. Scanning Electron Microscopy (SEM) and Energy-Dispersive X-ray Spectroscopy (EDX)

Scanning electron microscopy (SEM) and Energy-Dispersive X-ray Spectroscopy (EDX) are two most widely used techniques to investigate the morphological and the microstructural properties, as well as the elemental composition of the subjected area of the samples. There are different types of electrons emitted from the sample upon its interaction with the electron beam, namely secondary electrons (SEs) and backscattered electrons (BSEs), which occur due to the inelastic and elastic interactions, respectively. Topological images of the subjected area are generated by detection of the emitted SEs as they originate from the near-surface region of the sample and enables us to observe the surface features and morphological properties. EDX, on the other hand, equipped with SEM, collects the emitted characteristic X-rays, and provides both qualitative and quantitative information about the elemental composition of the sample.

In this work, the size, the microstructural properties including elemental compositions, and the morphologies of the synthesized particles were investigated by a field emission scanning electron microscope (FE-SEM, Zeiss Leo Supra 35 VP) using a field emission gun (FEG) as the electron source at 3-15 kV operating voltage to record high-resolution images. A sputter coater (Cressington 108) was used for coating the samples with Au-Pd at 40 mA for 120 s prior to analysis. EDX elemental maps were acquired by a Bruker EDX-Xflash detector attached to a Zeiss Leo Supra 35 VP. The acquisition of EDX elemental maps were performed at 15 kV operating voltage using the Bruker Esprit software.

### 3.1.5. Differential thermal analysis (DTA) and thermogravimetric analysis (TGA)

Thermal analysis is a crucial characterization tool, especially in solid-state physics and chemistry, to observe the thermal stability of a material, the phase transitions during heat treatment, and changes in its weight as the temperature changes.

In this work, differential thermal analysis (DTA) was used to investigate the thermal profile of the precursors, especially the release of organic species and the phase transitions as a function of temperature, to be able to determine the required temperature for calcination and heat treatment of the synthesized particles, whereas the changes in weight of the particles were monitored simultaneously with thermogravimetric analysis (TG) using a Shimadzu DTG-60H TG/DTA simultaneous measuring instrument.

## 3.2. Optical and Electronic Characterization Methods

### 3.2.1. Photoluminescence Spectroscopy (PL)

Photoluminescence spectroscopy (PL) is a useful tool to determine the energy levels in various kinds of materials, in particular semiconductors. In a typical PL-excitation (PLE) measurement, first, a laser beam with a fixed wavelength is used to irradiate the electrons in the sample to excite them from the ground state to the excited state. Then, during the relaxation of the excited electrons to the ground state, the excess energy is emitted as light (or photon), recorded by the detector and converted to an electrical signal to plot the variation of the PL intensity as a function of the excitation wavelength. The output of this measurement carries important information on both intrinsic and the extrinsic transitions. The latter is closely related to the defect states, i.e., trap states, since near-band gap transitions have relatively weak energies than that of the ones in volume, thereby appear at higher wavelengths.

In this work, an FS5 Edinburgh Instrument PL spectrometer equipped with a light source of 150 W CW Ozone-free Xenon arc lamp, a Czerny-Turner monochromator with plane gratings, and a special sample holder for direct measurement of solid samples was used to probe the optoelectronic properties of the point defects in the synthesized particles.

### 3.2.2. Electron Paramagnetic Resonance Spectroscopy (EPR, or ESR)

Electron Paramagnetic Spectroscopy (EPR), also called ESR, is a nondestructive analytical technique based on the absorption of electromagnetic radiation in microwave frequency by a paramagnetic substance. It can be used for many different applications in physics, medicine, chemistry, and biology to examine various species, such as free radicals, reaction kinetics, oxidation reduction processes, conducting electrons and, here in particular, point defects. Atoms, ions or molecules having an unpaired electron in their outermost shells exhibit characteristic electronic properties. EPR takes advantage from the spin magnetic moments arise from the electrons. For an unpaired electron, the spin energy levels are degenerate, that is, electrons spin randomly, without an applied magnetic field. When an external magnetic field is applied, the spin energy levels split and the spin of the unpaired electron can align with and opposite to the magnetic field, creating two spin states $M_S = \pm \frac{1}{2}$. These two spin states have an energy difference between them since they have different energies. This phenomenon is called the Zeeman splitting (or Zeeman effect). Absorption occurs when the energy difference between two states is equal to the incident photon energy. The resonance condition can be described as in Eq. (1):

$$\Delta E = h.\nu = g.\beta.B_0.M_S \tag{1}$$

where h is the Planck's constant ($6.626 \times 10^{-34}$ J.s$^{-1}$), ν is the frequency of radiation (s$^{-1}$), g is the *g*-factor (spectroscopic splitting factor, unitless), β is the Bohr magneton ($9.274 \times 10^{-24}$, J.T$^{-1}$), $B_0$ is the magnetic field (in T), and $M_S$ is the electron spin quantum number.

In this thesis, the paramagnetic point defect centers were investigated using X-band (9.64 GHz) and Q-band (33.98 GHz) EPR spectroscopy. For the X-band measurements, the sample of interest was placed inside a spin-free 25 cm long quartz tube (Qsil®, Germany) and its X-band EPR spectrum was collected at room temperature with 2G modulation amplitude and 1.585 mW microwave power using a Bruker EMX Nano spectrometer. For Q-band measurements, an Elexys 500 Bruker spectrometer equipped with an ER 5106 QT, a standard Bruker Q-Band probe for CW-EPR, was used. The Q-band, UV-light and temperature dependency measurements were conducted by Dr. Arpad Mihai Rostas. The room temperature X-band measurements and the interpretation of all the data presented in this thesis were performed by the author.

# CHAPTER 4. RESULTS AND DISCUSSION

The sample codes given in Table 2 will be used hereafter to refer to the synthesized $B_4C$ powders.

Table 2. Sample codes and corresponding processing parameters used in this dissertation to refer to the $B_4C$ powders synthesized with different processing parameters.

| Sample code | Mannitol-to-boric acid molar ratio | Calcination temperature (℃) | Heat treatment temperature (℃) | Ball-milling time (min) |
|---|---|---|---|---|
| MBA14-414 | 1:4 | 400 | 1400 | - |
| MBA14-415 | 1:4 | 400 | 1500 | - |
| MBA14-515 | 1:4 | 500 | 1500 | - |
| MBA13.5-515 | 1:3.44 | 500 | 1500 | - |
| MBA14-515-BM20 | 1:4 | 500 | 1500 | 20 |
| MBA14-515-BM30 | 1:4 | 500 | 1500 | 30 |

## 4.1. Microstructural Investigations

### 4.1.1. Microstructural analysis of boron carbide

FTIR measurements were carried out to investigate the structural evolution of the precursors before calcination, especially to monitor the formation of B-O-C bonds that occur through the dehydration (Eqs. (2-4)) and condensation reactions (Eq. (5) and Fig. 8) [81, 82].

$$6H_3BO_3 \rightarrow_{(80\text{-}130℃)} 2(BOH)_3O_3 + 6H_2O \rightarrow_{(>130℃)} 3B_2O_3 + 9H_2O \quad (2)$$

$$2\ H_3BO_3 \rightarrow 2HBO_2 + 2H_2O \quad (3)$$

$$2HBO \rightarrow B_2O_3 + H_2O \quad (4)$$

$$H_3BO_3 + 3\ C_xH_yO_zOH \rightleftharpoons C_{3x\text{-}3}H_{3y}O_{3z}B(OC)_3 + 3\ H_2O \quad (5)$$

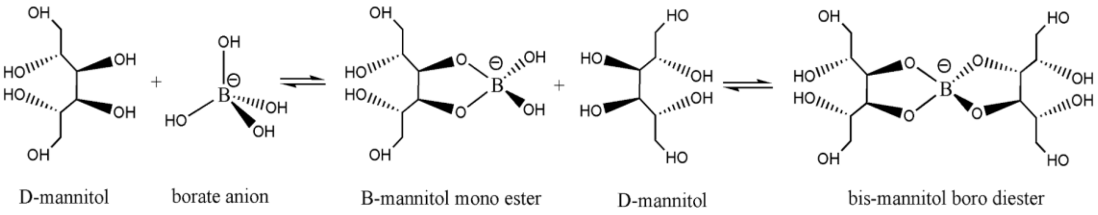

Figure 8. Reaction between boric acid and mannitol to form a dichelate complex.

Fig. 9 shows the FTIR spectra of the two precursors and the starting materials. For mannitol, the broad band at 3500-3200 $cm^{-1}$ was assigned to the characteristic broad band of O-H stretching, and the peaks at 3000-2886 $cm^{-1}$ and 1076-1017 $cm^{-1}$ were assigned to the C-H and C-O stretching vibrations, respectively. For boric acid, the characteristic stretching vibrations of O-H and B-O were observed at 3300-3100 $cm^{-1}$ and 1600-1300 $cm^{-1}$, respectively, whereas the peaks at around 1190, 700, 630 and 544 $cm^{-1}$ were assigned to the bending vibrations of B-OH, B-O-O, $BO_3$ and O-B-O, respectively [79, 83-86]. In the FTIR spectrum of the dried precursor prepared with excess amount of boric acid (M:BA molar ratio of 1:5, denoted as MBA15), the appearance of the stretching vibrations of carbon O-H, C-H and C-O for mannitol is dominant, indicating that the excess mannitol remained in the solution without forming borate complexes. On the other hands, for the condensed precursor synthesized from the M:BA molar ratio of 1:4 (MBA14), the characteristic stretching vibrations of mannitol were not observed while the stretching vibrations of O-H and B-O, and the bending vibrations of B-O-H become weaker than those of the boric acid, indicating that the B-O-C bonds were formed by the dehydration condensation reaction of mannitol and boric acid through the modified sol-gel process, as appeared in the FTIR spectrum of MBA14 at around 1035 $cm^{-1}$. It should be noted that the formation of B-O-C bonds through the dehydration condensation reactions prior to the heat treatment steps are crucial to synthesize boron carbide at temperatures lower than the conventional high-temperature (>2100 ℃) processes.

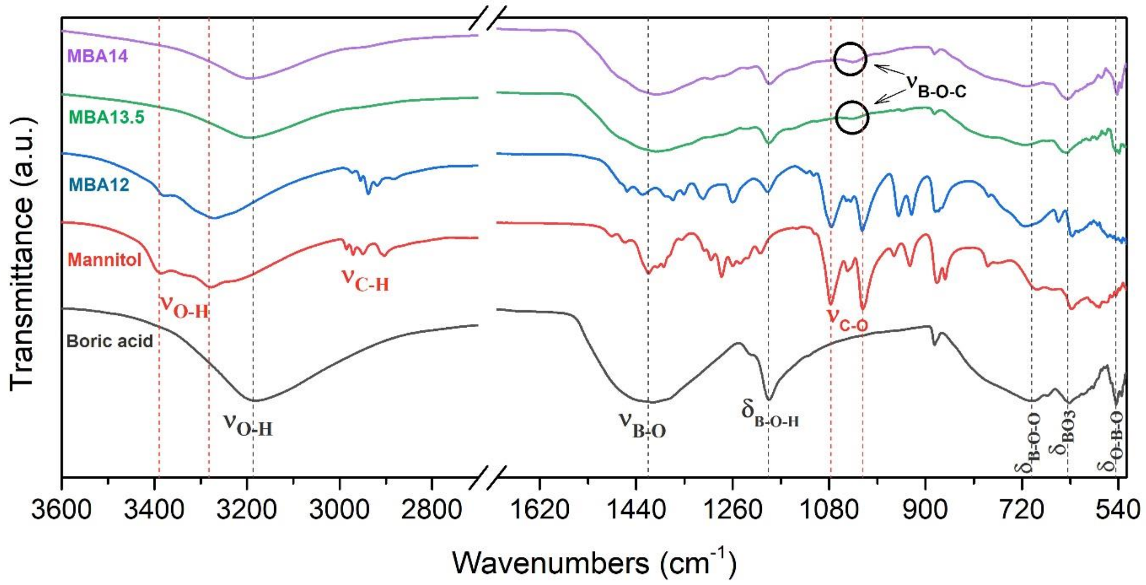

Figure 9. FTIR spectra of the starting materials and the condensed precursors dried at 110 °C in vacuum.

Fig. 10 represents the DTA/TGA profile of the dried gel precursor MBA14 recorded in argon atmosphere to monitor the material’s thermal stability and to determine the decomposition temperatures and corresponded weight losses through observation of the endothermic and exothermic events upon heating. TGA profile reveals two significant weight losses between 90-450 °C accompanied with endothermic and exothermic peaks at around 90-210 °C and 320-450 °C corresponded to the removal of physisorbed and chemically bonded water molecules (endothermic) and the decomposition of organic contents (exothermic), respectively. The vaporization equilibria of boron oxide phases given in Fig. 11 show that, below 1500 °C, the partial pressure of $B_2O_3$ is the highest among other boron oxide phases, and slightly lower than the partial pressure of $B_2O_2$ at 1500 °C (see the dashed red line) [87]. Accordingly, the significant broad endothermic peak observed until around 1460 °C is ascribed to the competitive generation and consumption of $B_2O_{2(g)}$ due to the carbothermic reduction of boron oxides with carbon on fluid/solid and gas/solid interfaces (Eqs. (6) and (7)), hence the nucleation and growth of boron carbide [88].

$$B_2O_{3(l)} + C_{(s)} \rightarrow B_2O_{2(g)} + CO_{(g)} \quad (6)$$

$$2B_2O_{2(g)} + 5C_{(s)} \rightarrow B_4C_{(s)} + 4CO_{(g)} \quad (7)$$

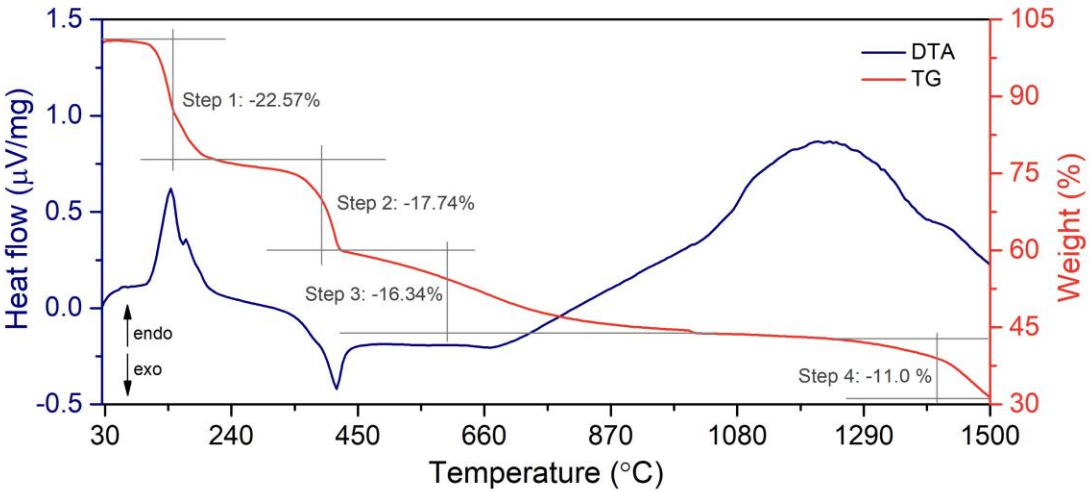

Figure 10. DTA-TGA profile of the MBA14 precursor synthesized from the M:BA molar ratio of 1:4.

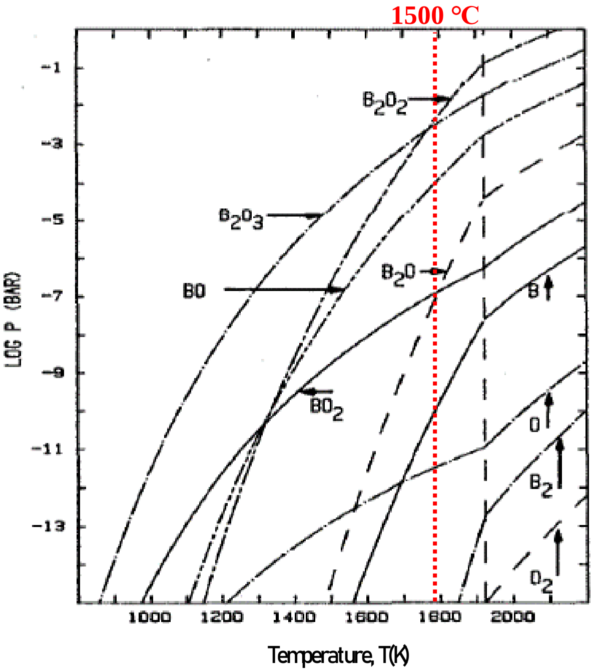

Figure 11. $B_2O_3$ vaporization in $10^{-15}$ bar ($10^{-10}$ Pa) $O_2$ below 1650 °C (1923 K) and vaporization of B-$B_2O_3$ mixture above 1650 °C (1923 K) (Reprinted from [87] with permission of the American Institute of Physics.)

In Fig. 12(a), the compared XRD spectra of the boron carbide crystals synthesized with different M:BA ratios and at different temperatures show that intensities of $B_2O_3$ (PDF #13-0570) and free C (PDF #01-0640) increased as the calcination and heat treatment temperatures decreased from 500 to 400°C, and 1500 to 1400°C, respectively. All samples exhibited the diffraction peaks corresponded to $B_4C$ (PDF #35-0798) at almost the same positions. The highest intensities of the $B_4C$ peaks was observed for MBA14-515 which was the only sample that contain neither $B_2O_3$ nor C phase. These results show that, for MBA14-515, no unreacted boron oxide remained in the structure after the synthesis of $B_4C$ at 500 and 1500 °C, respectively. By using excess boron source, the loss of boron species (oxides/suboxides) was compensated, and the required amount of boron was provided to form $B_4C$ through the reactions given in Eqs. (6) and (7) without excess carbon content. To confirm the crystal structure of MBA14-515 and to calculate the precise lattice parameters, the Rietveld refinement in Fig. 12(b) was performed for the XRD data of MBA14-515. The initial and refined lattice parameters, the space group and atomic positions are given in Table 3. The $B_4C$ phase was confirmed by comparison of the XRD data with the crystallographic information file (CIF) of the $B_4C$ phase obtained from Crystallography Open Database (COD) [89]. The measured and calculated patterns, their difference, the Bragg positions and the reliability factors (R factors) are included in the Fig. 12(b). The R factors and goodness of fit (GOF) were $R_{wp}$=9.29 %, $R_p$=6.96 %, $R_{exp}$=1.95 %, and $\chi^2$=4.76, indicating a good fit of the observed and the calculated patterns as evidenced in the graphical fit in Fig. 12(b).

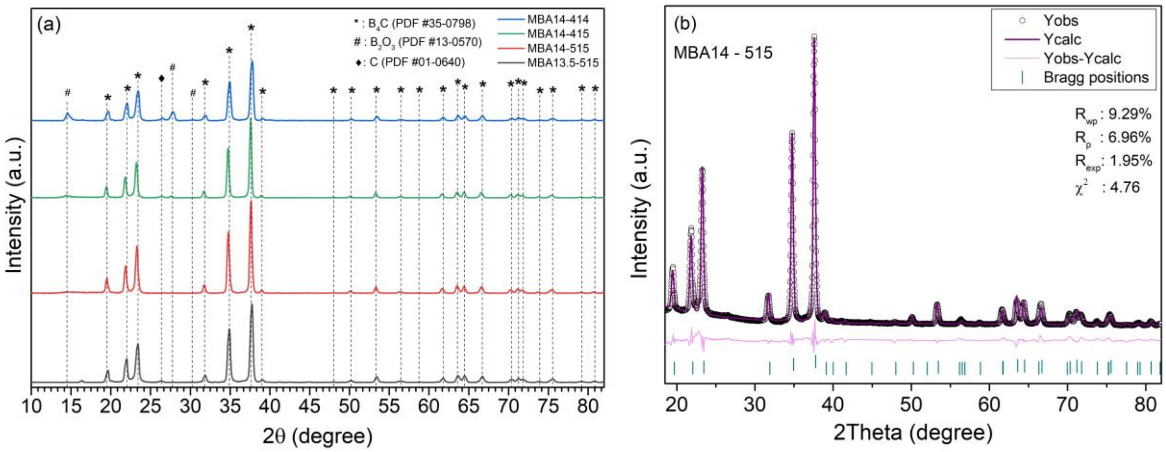

Figure 12. (a) XRD spectra of the boron carbide crystals synthesized with different M:BA ratios, calcined at 400-500 °C and heat treated at 1400-1500°C, and (b) Rietveld refined XRD pattern of the selected boron carbide sample (MBA14-515) (COD code: 4124697).

Table 3. Refinement parameters of the $B_4C$ powder referred as MBA14-515.

| Phase | Space group | Refined lattice parameters | Initial lattice parameters | Atoms | Atomic positions |
|---|---|---|---|---|---|
| **$B_4C$** | R-3m:H | a = 5.608891 Å<br>b = 5.608397 Å<br>c = 12.09053 Å<br>V = 329.140 $Å^3$<br>α = 89.90153°<br>β = 90.06901°<br>γ = 120.0708° | a = b = 5.6 Å<br>c = 12.12 Å<br>V = 329.162 $Å^3$<br>α = β = 90°<br>γ = 120° | B1 | x = 0.15400<br>y = -0.06894<br>z = 0.37973 |
| | | | | C1 | x = 0.17635<br>y = 0.31747<br>z = 0.13349 |
| | | | | B2 | x = 0.02288<br>y = 0.01152<br>z = 0.12060 |
| | | | | C2 | x = y = z = 0 |

The FE-SEM images of the MBA14 precursor and the synthesized $B_4C$ powders were presented in Fig. (13)-(17). The microstructure of the condensed gel precursor exhibits an epitaxial growth as shown in Fig. 13(a) and 13(b) at different magnifications. A previously reported model suggests that the nucleation of a crystalline $B_4C$ particle initiates from the outer portion of the precursor and propagates inward as the temperature increases [90]. In addition to that model, we report that, once a $B_4C$ nucleates, new nucleus tends to grow on top of existing nuclei where C exists in solid form and reacts with the boron suboxide gases, and the process continues by maintaining the equiaxed morphology until the reactants (i.e., boron oxide/suboxide and carbon) are fully consumed at the active nucleation site. The proposed mechanism is supported by the FE-SEM micrograph given in Fig. 14(c) and its zoom in view in Fig. 14(d), which clearly shows its fused layered inner structure. From the FE-SEM investigations, the particle size of the $B_4C$ was determined within the range of 10 μm-100 nm. EDX results in Fig. 15 demonstrate the elemental mapping of B and C in $B_4C$ to maintain the 4:1 stoichiometry of B:C, which confirms the XRD results in Fig. 12 on the absence of $B_2O_3$ in MBA14-515. For the comparison, the FE-SEM images of MBA14-414 and MBA13.5-515 were shown in Fig.16 and Fig. 17, respectively. Fig. 16 confirms the presence of unreacted $B_2O_3$ phases both coated on the surface of and around the $B_4C$

particles, and Fig. 17 shows that the structure contains residual carbon and unreacted $B_2O_3$ phase within the structure.

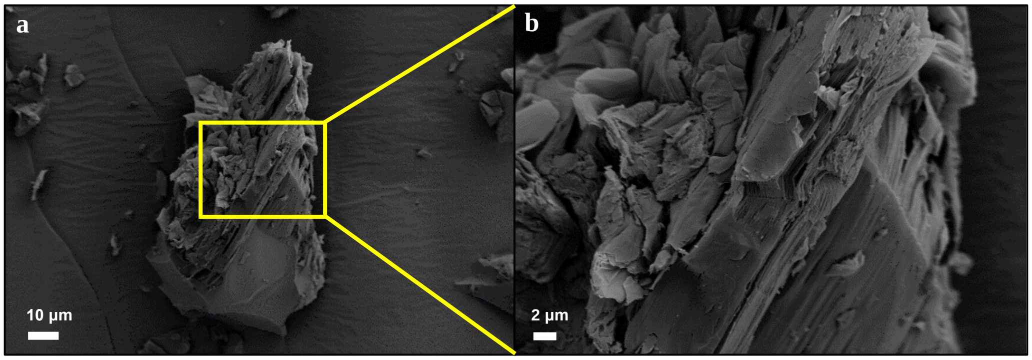

Figure 13. FE-SEM images of MBA14 condensed gel precursor at (a) 2kX and (b) 7.5kX magnifications.

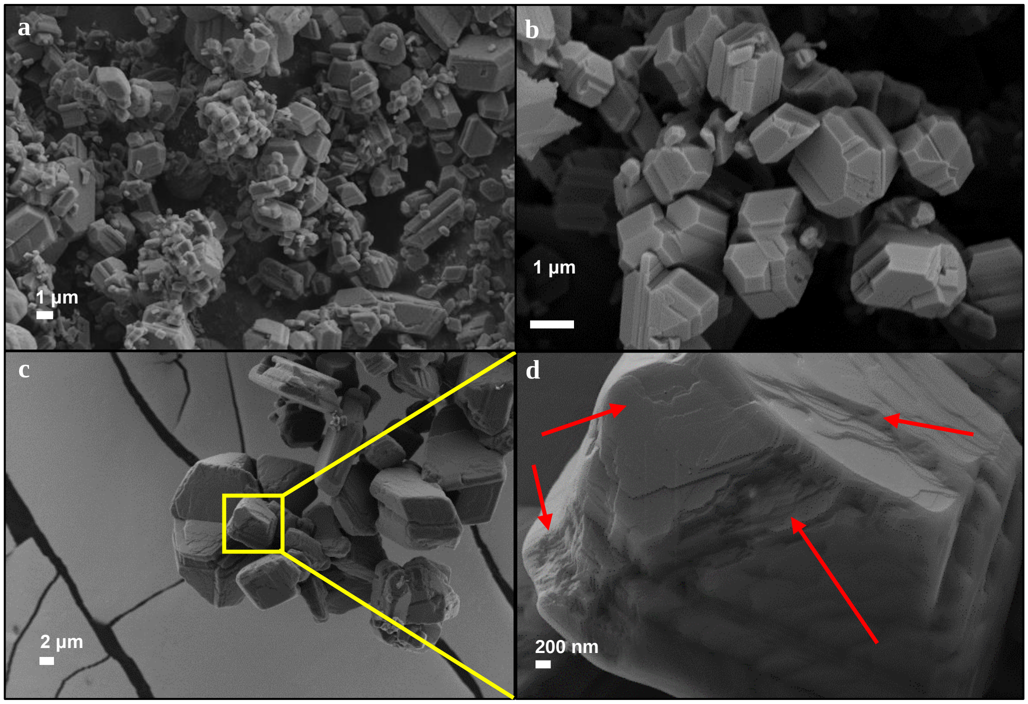

Figure 14. FE-SEM micrographs of the boron carbide (MBA14-515) calcined at 500℃ and heat treated at 1500℃: (a-b) taken from different regions of the sample at 10kX and 25kX magnifications; micrographs of the same region (c) at 5kX and its zoom in image (d) at 50kX magnifications, respectively. The red arrows indicate some of the many regions where the fused layered inner structure of the $B_4C$ is visible (50kX magnification).

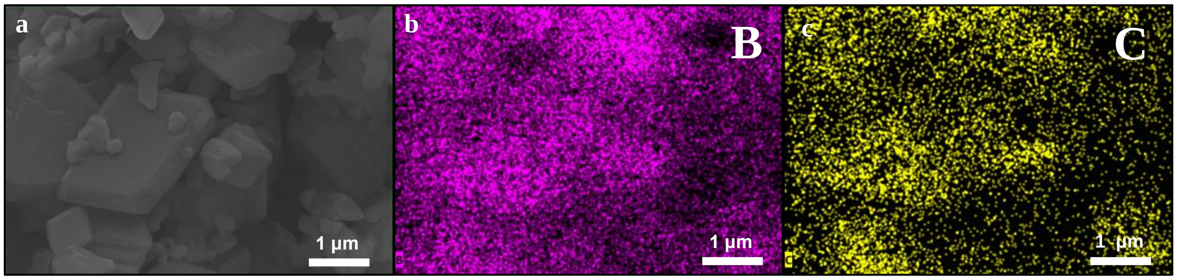

Figure 15. FE-SEM-EDX elemental maps of the boron carbide (MBA14-515) sample calcined at 500℃ and heat treated at 1500℃; (a) FE-SEM image, (b) B map, and (c) C map at 50 kX magnification.

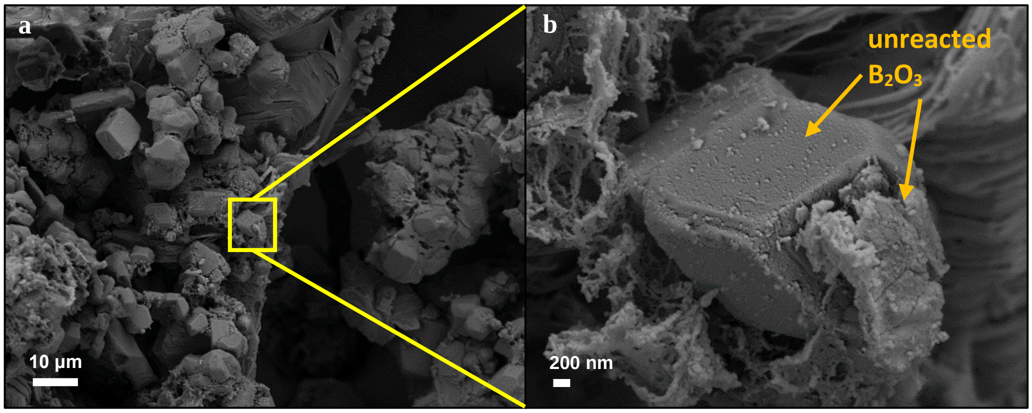

Figure 16. FE-SEM images of the boron carbide (MBA14-414) calcined at 400 ℃ and heat treated at 1400 ℃ at (a) 5kX and (b) 50kX magnifications. Orange arrows show the unreacted $B_2O_3$ phases.

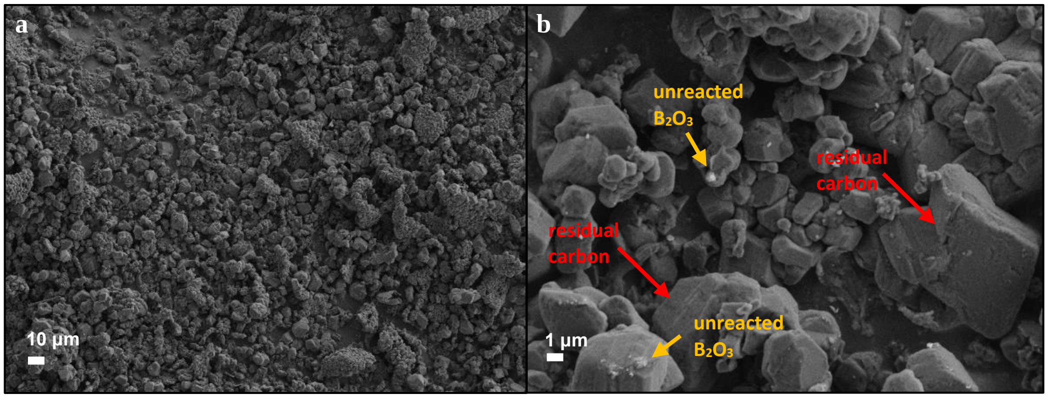

Figure 17. FE-SEM images of the boron carbide (MBA13.5-515) calcined at 500 ℃ and heat treated at 1500 ℃ at (a) 1kX and (b) 10kX magnifications. Red arrows show the residual carbon content, and the orange arrows show the unreacted $B_2O_3$ phases.

The Raman spectra of the boron carbide samples were recorded to investigate the effects of both the mannitol to boric acid molar ratio, hence the carbon content, and the calcination temperature on the defective properties of the crystals. The presence of a D-band and a G-band in a Raman spectrum is ascribed to the defect-induced in-plane vibrations of $sp^2$ carbon and in-plane vibrations of $sp^2$ crystalline carbon (high degree of order), respectively [91]. As it is shown in the comparative spectra in Fig. 18, the intensities of both D- and G-bands are decreasing in the order of MBA14-415 > MBA14-515 > MBA13.5-515, as expected. At calcination temperatures lower than 500 °C, the degradation and removal of carbonaceous species were not completed as it was depicted in Fig. 10, thereby the highest Raman intensities for both D- and G-bands were observed for the boron carbide calcined at 400°C (MBA14-415). On the other hand, the MBA13.5 composition with less boric acid (i.e., stoichiometric ratio) exhibited almost no defect-induced D-band, and the G-band has much smaller intensity compared to the MBA14-415 and MBA14-515. The intensity of the defect-induced peaks of MBA14-515 with excess boric acid (1:4) decreased as the calcination temperature increases from 400 to 500°C. The low frequency region below 600 $cm^{-1}$ is assigned to the characteristic Raman modes of the $B_{11}C$ icosahedron. Two characteristic broad bands at between 262-271 $cm^{-1}$ were due to the rotation of the icosahedron, and at around ~319 $cm^{-1}$ due to the wagging and chain rotation of the icosahedron. The sharp peaks at around ~472 and ~525 $cm^{-1}$ were assigned to the rotation of CBC chains perpendicular to the [111] direction and the libration of the icosahedra, respectively [92, 93]. The significant increase in intensities of the Raman modes both at high frequency (above 600 $cm^{-1}$) and the low frequency (below 600 $cm^{-1}$) regions for MBA14-515 indicate better nucleation and growth of boron carbide with well-ordered chains [94]. In addition, the intensity of G-band for $sp^2$ crystalline carbon significantly decreased for MBA14-515 when compared to the MBA14-415 due to the removal of excess carbon during calcination at 500 °C. However, the G-peak intensity was higher than that of MBA13.5-515 because excess boric acid compensated the loss of boron during the heat treatment above 1000°C and induced the formation of boron carbide, hence the crystalline carbon content. The final heat treatment temperature was 1500°C for all samples.

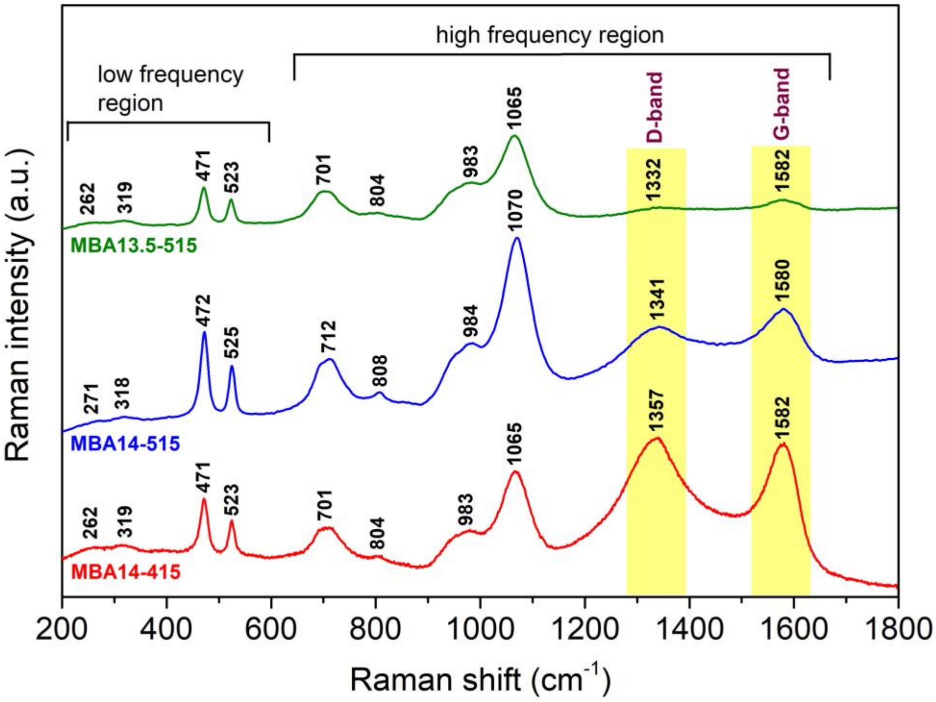

Figure 18. Comparison of the Raman spectra of the boron carbide crystals synthesized from precursors with different M:BA molar ratios (red and blue: 1:4, green: 1:3.44), calcined at 400-500 ℃, and heat treated at 1500 ℃.

## 4.2. Optical and electronic investigations in boron carbide via photoluminescence spectroscopy

Fig. 19 presents the photoluminescence (PL) spectra of $B_4C$ powder (MBA14-515) under 525 nm laser excitation at room temperature. Two sharp PL bands were appeared in the spectrum in Fig. 19(a) at 510 and 544 nm which correspond to 2.28 and 2.43 eV in Fig. 19(b), accompanied with a shoulder peak at around 1.92 eV. It should be noted that boron carbide can be found in different forms such as bulk pressed monoliths or fine powders, as well as in different structure formulas due to the variable stoichiometry of B and C. The variations in the B:C molar ratio and the presence of interstitial or substitutional defects can cause considerable deviations from the lattice parameters of rhombohedral structured boron carbide, i.e., expansion/contraction in the lattice volume, or increase/decrease in the c/a ratio. Additionally, it was reported that different trapping levels can occur in boron carbide due to the electron-phonon interactions [95]. These trapping levels may affect the luminescence characteristics hence the electronic band gap value of the subjected boron carbide. Therefore, the structure formula ($B_xC_{1-x}$), the doping level and the form of boron carbide should be indicated when considering the electronic band gap of the material. Werheit et *al.* reported an electronic band gap energy of 2.09 eV for the hot pressed carbon-rich boron carbides with structure formula of $B_{4.3}C$, attributed to the indirect allowed interband transitions which shown in Fig. 20 [55, 95]. The optical band gap values of 2.28 and 2.43 eV at 540 and 510 nm, respectively, were attributed to the $sp^2$-bonded C species, whereas the band gap of 1.92 eV that appeared as the shoulder band at 645 nm was attributed to the $B_4C$. The band gap of 2.09 eV is close to our findings with a small deviation (~1.92 eV), which is most probably due to the small difference in B:C stoichiometry, as well as the presence of interstitial defects. These findings are in good agreement with the available literature and with the Raman results discussed in this chapter [55, 96].

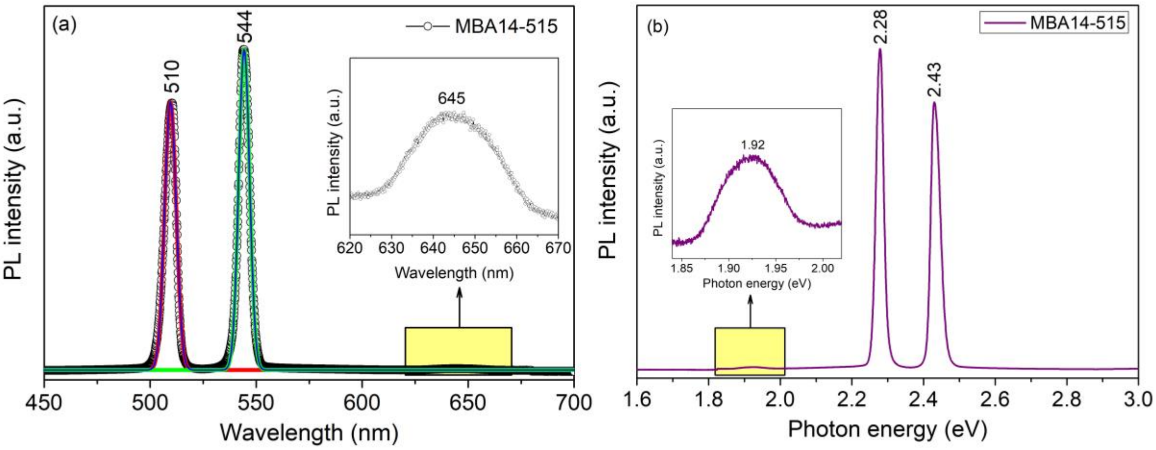

Figure 19. PL spectra of the $B_4C$ powder (MBA14-515) calcined at 500 ℃ and heat treated at 1500 ℃. Insets in (a) and (b) show the zoomed-in view within the range 620-670 nm and the corresponded optical band gap, respectively.

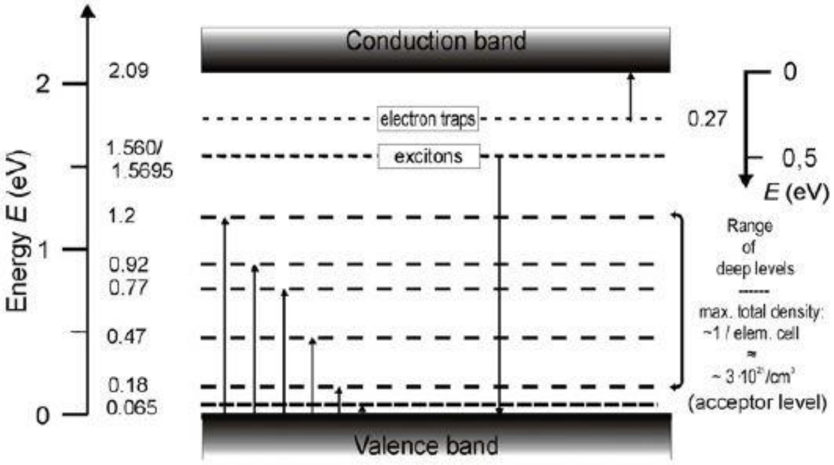

Figure 20. Energy band scheme of boron carbide based on optical absorption, luminescence, XRS, and transport properties. Left ordinate, energies related to the valence band edge; right ordinate, energies relative to the conduction band edge. Arrows indicate the direction of the measured optical transition. (Reprinted from [55] with permission of the Institute of Physics Publishing.)

Overall, the presented results for MBA14-515 are consistent and prove that the boron carbide with $B_4C$ stoichiometry was formed. However, the presence of D- and G-bands in its Raman spectrum and the PL peaks corresponded to the sp$^2$-bonded C species need to be further investigated in terms of the existence and nature of the defects. Since XRD is not sensitive enough to detect very low elemental/phase concentrations or to probe the lattice deficiencies such as point defects, it should be complemented with electronic characterization by using electron paramagnetic resonance (EPR) spectroscopy, as discussed in Chapter 5.

# CHAPTER 5. PROBING OF INTRINSIC POINT DEFECTS VIA ELECTRON PARAMAGNETIC RESONANCE (EPR)

Electron paramagnetic resonance (EPR) spectroscopy is a state-of-the-art technology for the analysis of electronic structure of the materials, in particular point defects and impurities, by detecting the paramagnetic centers within the crystal. As is evident from the description of the method, the defect properties of a material can only be investigated via EPR if the material of interest have unpaired electrons in its outer shell. Both defective boron carbide with $B_4C$ stoichiometry and ZnO should have unique EPR signals arising from the point defects (i.e., vacancies or interstitial atoms) within the lattice. The defect properties of unmilled, 2 h milled, and 4 h milled ZnO, as well as the synthesized $B_4C$ powders were characterized by X-band (9.64 GHz) and Q-band (33.96 GHz) EPR spectroscopy, and the results were presented in this chapter.

## 5.1. Probing of Electronic Properties of $B_4C$ via X-band EPR Spectroscopy

Boron carbide ($B_xC_{1-x}$) has a rhombohedral structure composed of mainly $B_{12}$ or $B_{11}C$, or less likely $B_{10}C_2$ icosahedra at the corners that linked together by the strong covalent inter-icosahedral three-atom chains located along the main diagonal of the rhombohedral axis. The possible configurations of these linear three-atom chains are C-C-C, C-B-C or C-B-B depending on the carbon concentration and the level of incorporation of carbon into the boron carbide structure rather than formation of a secondary graphite phase [54]. For boron carbide with $B_4C$ formula, it was shown that the structure is preferably formed by $B_{11}C$ icosahedra connected with C-B-C intericosahedral chains. The substitution of the carbon atoms in the icosahedra causes a disorder in the structure which is the origin of the p-type semiconducting character of $B_4C$, and significantly affects the electronic properties in terms of self-trapping and hence formation of the point defects [54, 92].

The point defect properties of the synthesized boron carbide powders were first investigated by analyzing the paramagnetic centers via X-band EPR spectroscopy (9.64 GHz) at room temperature. The EPR spectra of the synthesized $B_4C$ powders and the raw materials were recorded using a Bruker Xenon Nano software and presented in Fig. 21. As expected, both boric acid and mannitol are EPR-silent with a typical diamagnetic behavior due to the lack of unpaired electrons in their outer shells, whereas a strong signal was detected for all the synthesized $B_4C$ powders, confirms the presence the paramagnetic defective centers.

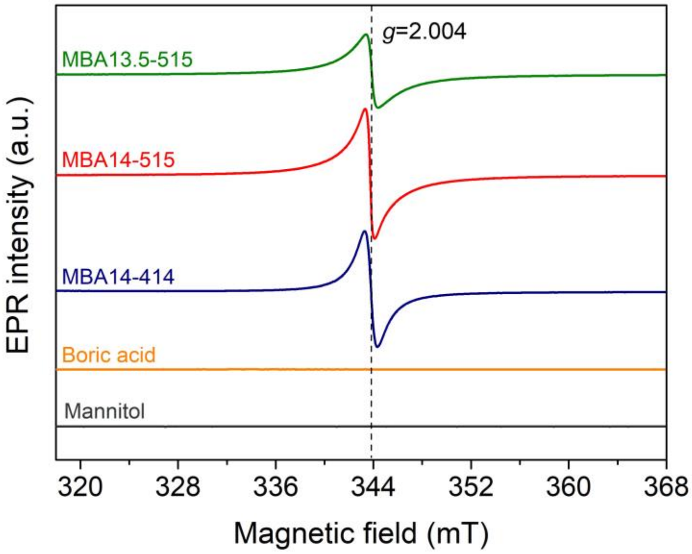

Figure 21. X-band EPR spectra of raw materials and synthesized $B_4C$ powders recorded at room temperature. The EPR intensities were normalized according to the mass of each sample.

The intensity of the EPR signal does not only depend on the concentration, but also strongly related to the microwave power. In ideal conditions, the EPR intensity increases linearly with the square root of the microwave power. However, when the magnitude of applied microwave power exceeds the relaxation rates (that is, how fast spins turn back to the z axis, or return to equilibrium), the signal starts to broaden, then deviates from the linearity and diminishes with increasing power, which is called power saturation effect. Since both spin-lattice ($T_1$) and spin-spin ($T_2$) relaxations contribute to the EPR signal, the saturation threshold should be determined to be able to make a comparison between the EPR spectra of the synthesized $B_4C$ samples. The saturation behavior of the synthesized $B_4C$ powders were presented in Fig. 22. The power dependent measurements were conducted at room temperature from 3.162x10$^{-4}$ mW to 79.43 mW under air atmosphere. The saturation effects were observed for MBA14-414 and MBA13.5-515 at 39.81 mW and 25.12 mW in Figs. 22(a) and 22(b), respectively, whereas the strongest deviation from the linear trend was observed for MBA14-515 at 25.12 mW (Fig. 22(c)).

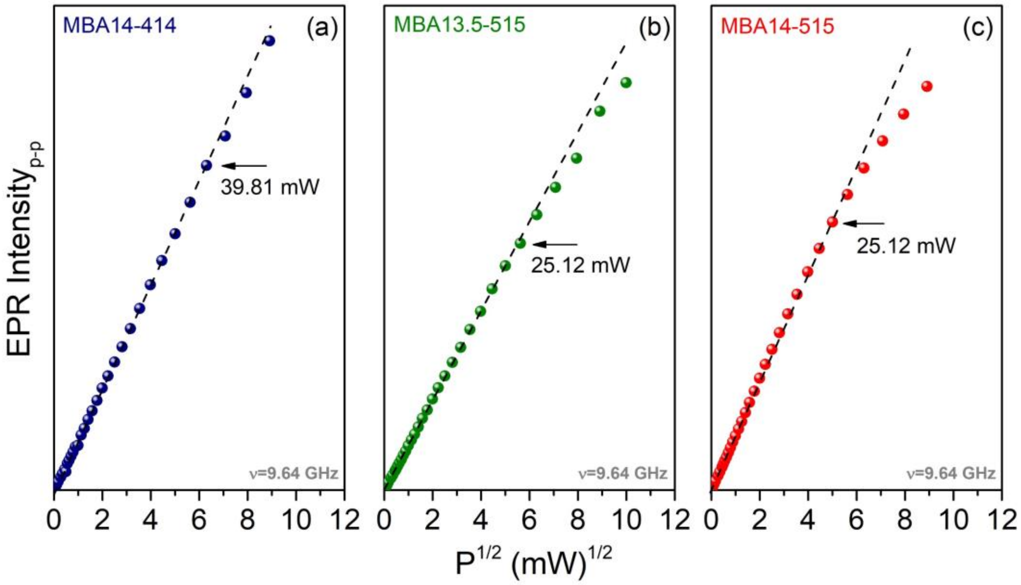

Figure 22. Peak-to-peak EPR intensity of the synthesized $B_4C$ powders with respect to $P^{1/2}$: (a) MBA14-414, (b) MBA13.5-515, and (c) MBA14-515. The EPR intensities were normalized according to the mass of each sample.

To ease the comparison of the signal intensities and the magnetic field positions, and to calculate the accurate *g*-factor of the synthesized $B_4C$ powders, the first integral of each signal (i.e., the absorption spectrum) was plotted with respect to the EPR intensity. The absorption spectra and the g-factor values of all the samples were shown in Fig. 23 (a-d). The *g*-value of 2.004 was calculated for all the samples. The $B_4C$ powder referred as MBA14-515 exhibited the highest EPR intensity, indicating the highest number of point defects compared to the other samples. The increase in the defect centers in MBA14-515 can be attributed to the following factors: (i) maintained molar ratio of mannitol-to-boric acid at 1:4 to introduce the required amount of boron and carbon to satisfy the stoichiometry of the reactions to form $B_4C$, (ii) the optimum pyrolysis temperature of 500 °C which induced the removal of the excess organic content and provided the formation of $B_4C$ at 1500 °C without any secondary or amorphous phases, and (iii) formation of C-B-C chains as paramagnetic centers in between the $B_{11}C$ icosahedra. These findings are in accordance with the XRD, Raman and PL results discussed in Chapter 3.

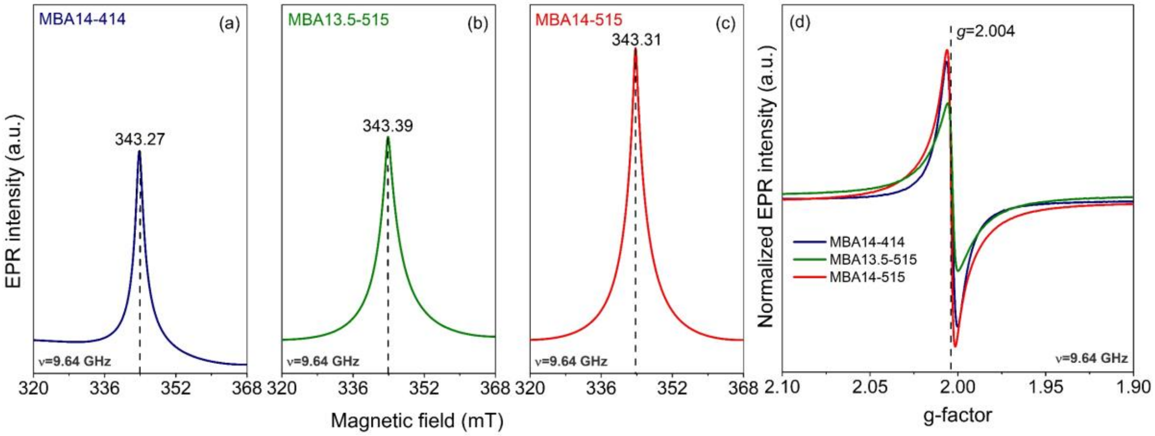

Figure 23. (a-c) X-band EPR absorption spectra of the synthesized $B_4C$ powders recorded at room temperature, and (d) g-values measured at room temperature at 1.585 mW. The EPR intensities were normalized according to the mass of each sample.

To investigate the effect of ball milling on the evolution of the defects, the synthesized $B_4C$ powder having no amorphous or free carbon content (MBA14-515) was placed in a 45 ml zirconia vial using Ø 2 mm zirconia balls with BPR of 13:1, milled at 500 rpm for 20 and 30 min, and the ball milled samples were referred as MBA14-515-BM20 and MBA14-515-BM30, respectively. The X-band EPR signal intensity was significantly increased after ball milling the $B_4C$ powder for 20 min, but then decreased as the ball milling time is increased from 20 to 30 min (Fig. 24). The significant increase in the signal intensity with the ball milling for 20 min is mainly due to the surface defects introduced into the $B_4C$ crystals during the milling process. As the particle size decreased from micron to nano region, the surface area increased and led to an increase in the EPR signal of the surface carbons. However, the increased strain with the increased milling time of 30 min most likely induces the loss of long range order and subsequently the formation of the amorphous phase, therefore the EPR signal intensity decreases for MBA14-515-BM30.

Peak-to-peak linewidths ($\Delta B_{p-p}$) were calculated from the difference of the magnetic field positions corresponding to the extreme points of the EPR spectra in Fig. 24(a). The $\Delta B_{p-p}$ of 1.4209, 0.8406 and 0.8806 for MBA14-515, MBA14-515-BM20 and MBA14-515-BM30, respectively, showed consistently similar order as in the EPR intensities, but the *g*-factor was found to be 2.004 and did not vary with milling, as depicted in Fig. 24(b).

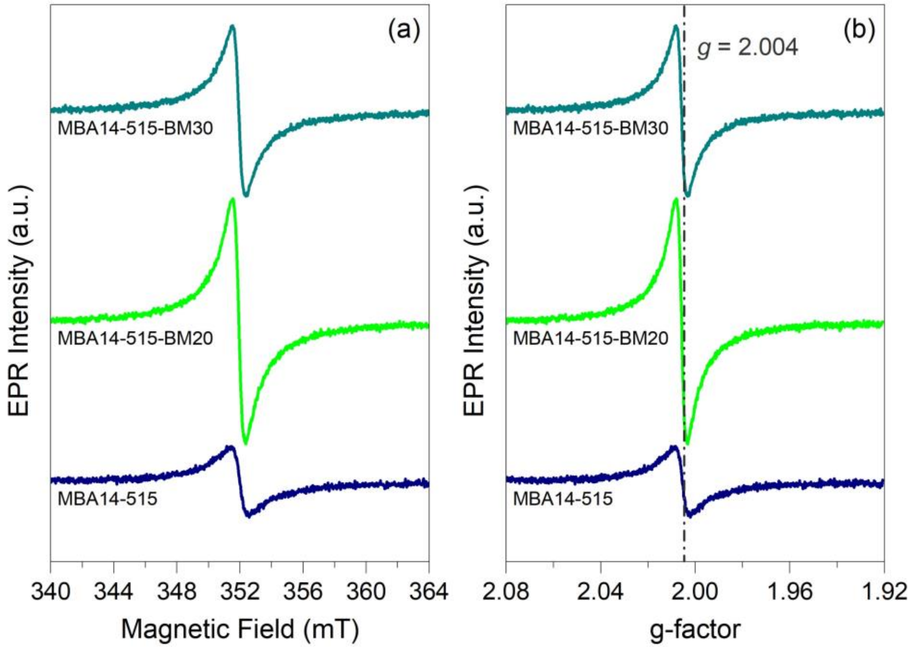

Figure 24. Comparisons of (a) X-band EPR spectra and (b) g-factors of the as-synthesized and ball-milled $B_4C$ powders, where MBA14-515-BM20 and MBA14-515-BM30 refer to the $B_4C$ ball milled for 20 and 30 min, respectively.

The influence of UV-light on the formation of new defect centers and on the X-band EPR signal intensities were studied through in-situ UV-irradiation experiments at room temperature. The measurements were conducted first in the dark, then under the irradiation with UV-light for different durations, and finally in the dark again. The EPR spectra of $B_4C$ powders before and after the UV-irradiation were shown in Fig. 25. Insets in Fig. 25(a-e) show that all the $B_4C$ samples exhibited the same *g*-factor of 2.004, however, the amplitudes of the EPR signals varied depending on the synthesis and the heat treatment temperature of the samples as it was discussed previously.

The temperature-dependent properties of the defect centers in the synthesized $B_4C$ powders were studied between 120-300 K in X-band at a frequency of 9.88 GHz, and the comparative results were presented in Fig. 26. As it is observed from the spectra in Fig. 26(a-c), the peak intensities increase as the temperature is decreased from 300 K to 120 K. All the EPR intensities of the synthesized $B_4C$ powders exhibited a significantly similar increase with a decrease in temperature, especially below 150 K. On the other hand, the signal intensities of the ball milled $B_4C$ powders in Fig. 26(d) and (e) were increased compared to that of the unmilled sample in Fig. 26(c) which were ascribed to the increased shell defects due to the increase of the surface area by ball milling.

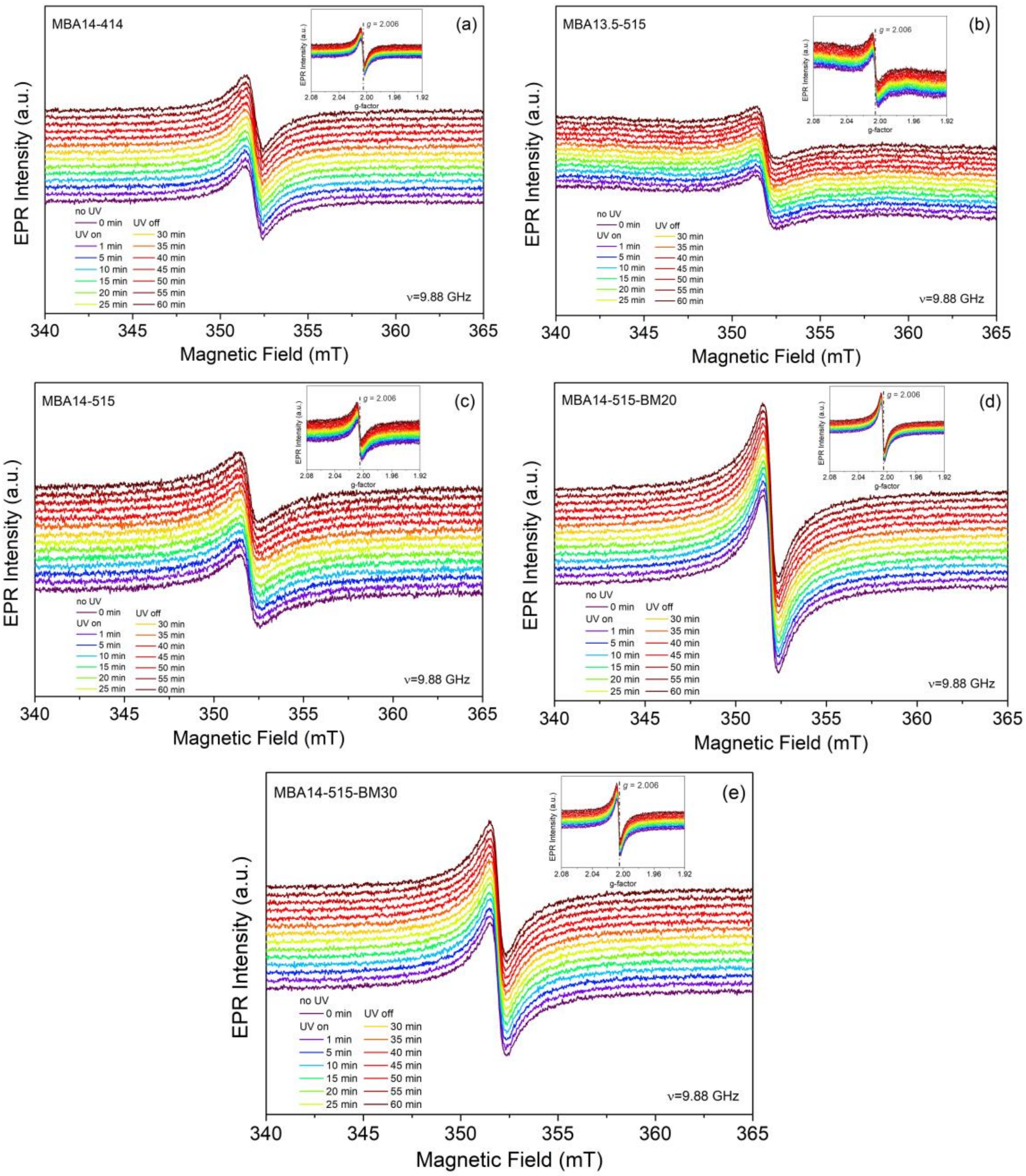

Figure 25. X-band EPR spectra of $B_4C$ powders before and after UV-light irradiation recorded at a frequency of 9.88 GHz: (a) MBA14-414, (b) MBA13.5-515, (c) MBA14-515, (d) MBA14-515-BM20, and (e) MBA14-515-BM30. The insets show the *g*-factors of the measured samples.

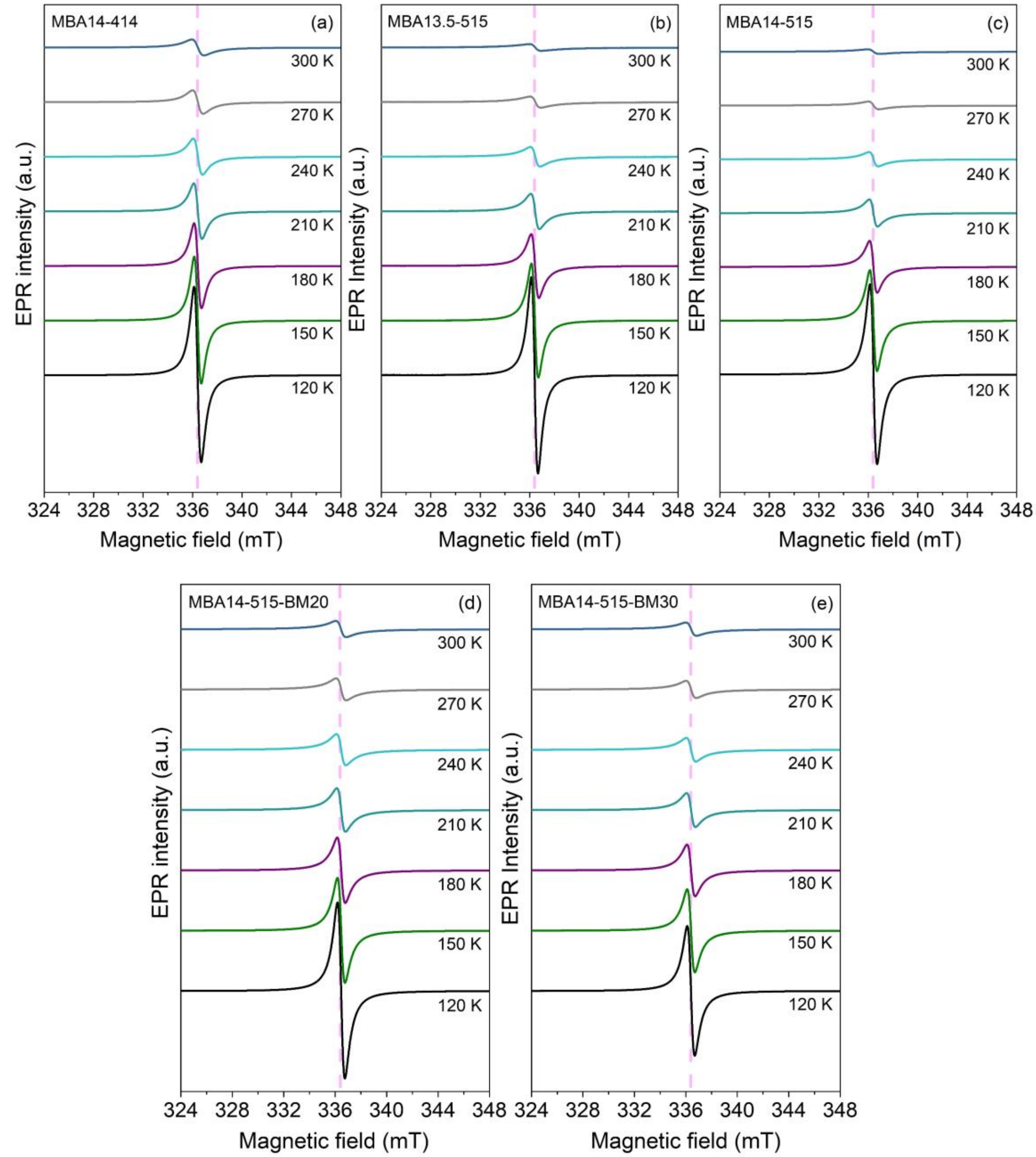

Figure 26. X-band EPR spectra of the $B_4C$ powders measured at temperatures from 300 K to 120 K at a frequency of 9.88 GHz: (a) MBA14-414, (b) MBA13.5-515, (c) MBA14-515, (d) MBA14-515-BM20, and (e) MBA14-515-BM30.

$\Delta B_{p\text{-}p}$ were found to vary from 0.54 to 0.58 mT at 120 K and 0.88 to 0.98 mT at 300 K, in accordance with the previous studies [97]. A negligible shift in the magnetic field positions were observed, and the peak-to-peak linewidths were increased similarly with temperature, indicating a common defect in all three samples, as shown in Table 4 and Fig. 27. The broadest EPR lines were appeared at 300 K, and they became narrower and sharper with decreasing temperature. In addition, the amplitudes and the linewidths of the EPR signals of the synthesized $B_4C$ powders depend on the synthesis conditions and the heat treatment processes. The free carbon content of the as-synthesized $B_4C$ samples is decreasing in the order of MBA14-414 > MBA13.5-515 > MBA14-515. Nevertheless, there is no direct relation between the free carbon content and the $\Delta B_{p\text{-}p}$, indicating that increased paramagnetic behavior at 120 K does not depend on the free carbon content but attributed to the localized spins of defects which arise from the replacement of some of the boron atoms with carbon atoms within the three-atom chains. The origin of the localized spins is ascribed to the extra electron introduced into the system by that carbon atom (CBC→CCC or CBB→CCB) upon replacing the boron atom [97, 98].

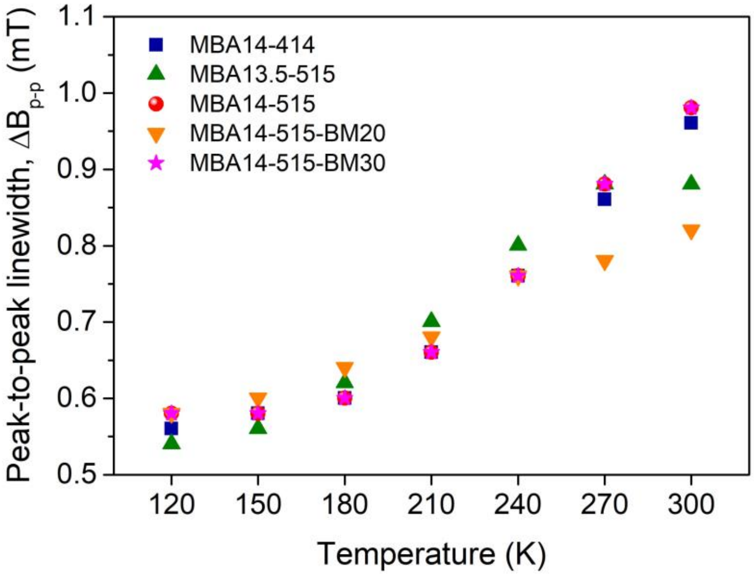

Figure 27. The peak-to-peak linewidths ($\Delta B_{p\text{-}p}$) of the EPR spectra plotted against temperature in Fig. 26.

Table 4. The tabulated values of the $\Delta B_{p\text{-}p}$ of the EPR spectra plotted against temperature in Figs. 26 and 27.

| **Sample code** | **$\Delta B_{p\text{-}p}$ (mT)** | | | | | | |
|---|---|---|---|---|---|---|---|
| | **120 K** | **150 K** | **180 K** | **210 K** | **240 K** | **270 K** | **300 K** |
| **MBA14-414** | 0.5604 | 0.5804 | 0.6004 | 0.6604 | 0.7605 | 0.8606 | 0.9606 |
| **MBA13.5-515** | 0.5404 | 0.5604 | 0.6204 | 0.7005 | 0.8005 | 0.8806 | 0.8806 |
| **MBA14-515** | 0.5804 | 0.5804 | 0.6004 | 0.6604 | 0.7605 | 0.8806 | 0.9806 |
| **MBA14-515-BM20** | 0.5804 | 0.6004 | 0.6204 | 0.6805 | 0.7405 | 0.7805 | 0.8206 |
| **MBA14-515-BM30** | 0.5804 | 0.6004 | 0.6404 | 0.6805 | 0.7605 | 0.7805 | 0.8206 |

## 5.2. Probing of Intrinsic Defect Centers in ZnO via X-band EPR Spectroscopy

ZnO has interesting structural properties including native point defects such as oxygen vacancies (in three charge states: neutral ($V_O^0$), +1 ($V_O^+$), and +2 ($V_O^{2+}$)), oxygen interstitials (in three charge states: neutral ($O_i^0$), -1 ($O_i^-$), and -2 ($O_i^{2-}$)), oxygen antisites ($O_{Zn}$ in the -2 charge state $O_{Zn}^{2-}$), zinc vacancies (in three charge states: neutral ($V_{Zn}^0$), -1 ($V_{Zn}^-$), and -2 ($V_{Zn}^{2-}$)), zinc interstitials ($Zn_i$; $Zn_i^+$(upon excitation) and $Zn_i^{2+}$(stable)), and zinc antisites ($Zn_O$; in the +2 charge state $Zn_O^{2+}$), among which $V_O$, $Zn_i$ and $Zn_O$ act as donors and $V_{Zn}$, $O_i$ and $O_{Zn}$ act as acceptors, as shown in Fig. 1 and Fig. 2, [26, 50, 99]. Probing of these native defects via EPR spectroscopy is possible only if the defects have unpaired electrons, in other words, paramagnetic spin states, which are $O_i^-$, $Zn_i^+$, $V_O^+$, $V_{Zn}^-$ (paramagnetic) and $V_O^0$, $V_{Zn}^0$, $O_i$ (if they exist in the triplet state, S=1) [47, 100].

The intrinsic point defects in the unmilled and the HEBM ZnO powders, which were used as electrodes in asymmetric SC devices in this dissertation, were analyzed using X-band EPR spectroscopy (9.64 GHz) at room temperature. The EPR spectra of the 0 (unmilled), 2, and 4 h milled ZnO powders were recorded using a Bruker Xenon Nano software, and the comparative results were presented in Fig. 28. The EPR spectrum of unmilled ZnO shows only one signal at g~1.96. The significant deviation of the g-factor of these defect centers from the g factor of free electron ($g_{\text{free electron}}$=2.0023) is because these are the defects under the spin-orbit coupling effect and they are tightly bound to the core, therefore do not act as free electrons. After ball-milling for 2 hours, two distinct EPR signal appeared at around g=1.96 and g=2.00. Interestingly, the intensity of the signals due to the core defects significantly increased as the milling time increased from 2 h to 4 h while that of the newly appeared defects slightly decreased. Due to the close similarity of g-factor of the latter signals to the $g_{\text{free electron}}$, these EPR signals were attributed to the delocalized surface (shell) defects. The origins of both core (g~1.96) and shell (g~2.00) defects have been extensively discussed in the literature. Although there are many controversial reports about the origin of the g-factor of 1.96, they can be divided into two main categories: one set of reports associates g~1.96 with the singly ionized oxygen vacancies, and the others with singly ionized zinc vacancies [101-106]. The similar debate is also raised for the association of g~2.00 with defect centers: it has been assigned to the several defects including (ionized) zinc and oxygen vacancies, or to an $F^+$ center which corresponds to an unpaired electron that is trapped at an oxygen-ion vacancy [47, 107-109].

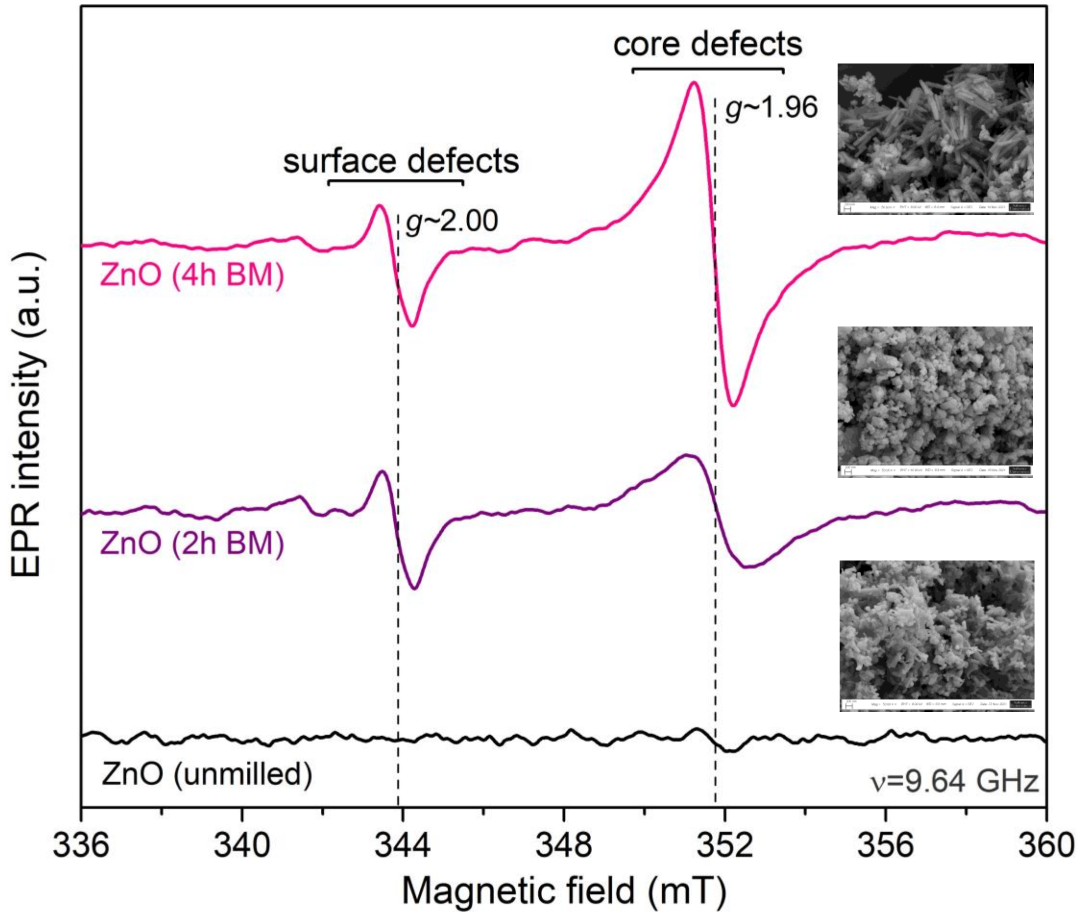

Figure 28. Comparative room temperature EPR spectra of 0, 2 and 4 h ball milled ZnO. The bottom, middle and top insets show the SEM images of unmilled, 2 h and 4 h ball milled ZnO nanocrystals, respectively. (Scale: 200 nm.)

## 5.3. Q-band EPR Spectroscopy of $B_4C$

Further analyses of paramagnetic defect centers in $B_4C$ have been conducted at higher frequency in Q-band EPR (33.98 GHz) to resolve the signals recorded in X-band thus to understand if there are other defects whose paramagnetic response is hindered by the surroundings, in particular core defects, that could not be revealed at X-band frequencies. The Q-band spectra of $B_4C$ synthesized via different synthesis procedures (see Chapter 2) were recorded at room temperature at microwave attenuations of 20 and 40 dB with microwave power of 0.014 mW. A comparative X- and Q-band spectra of the $B_4C$ powders is presented in Fig. 29. Insets in Fig. 29(a-d) show the additional signals that could not be monitored in X-band but resolved in Q-band. At 20 dB, both X- and Q-band spectra of all the samples in Fig. 29(a) and (b) exhibited a single strong signal, indicating that neither the EPR microwave frequency nor the attenuation are sufficient to resolve any peaks arising from the defects residing at the deeper level (i.e., core) of the crystals. As the microwave attenuation is increased from 20 to 40 dB, additional peaks started to appear, but still not well resolved at X-band frequency (Fig. 29(c)), therefore measurements at higher microwave frequencies are necessary. Indeed, the increased Q-band microwave frequency of ~34 GHz and microwave attenuation of 40 dB enabled these additional signals to be resolved at *g*-factors of 2.0003, 2.0003 and 2.0007 for the boron carbide samples MBA13.5-515, MBA14-414 and MBA14-515, respectively. Although there are numerous computational studies as well as some reports coupled with experiments reported in the literature on the determination of the precise crystal structure of boron carbide, the debate is still open because of the complicated crystal structure and lattice parameters of the boron carbide. In the case of boron carbide, to represent the whole structure, one deals with isomorphous elementary cells that composed differently instead of a unit cell, therefore there are numerous possibilities of forming crystal structures composed of different types of icosahedra ($B_{12}$ or $B_{11}C$) or intra/intericosahedral chains (C-B-C, C-B-B, B□B, □:vacancy) distributed over the structure with different homogeneities [110]. In accordance with the present literature on the electronic properties of the boron carbide, the major EPR signals in Fig. 29 with *g*-factors of ~2.004 were attributed to the carbon atoms localized near the surface, whereas the additional signals that appeared in Q-band frequencies at 40 dB at *g*-factors between 2.0003-2.0007 (which differ significantly from the $g_{free}$=2.0023) were ascribed to the core defects either due to the vacancies in the intericosahedral chains, or the carbon atoms substituting for boron in C-B-C chains that localized near the core [110, 111].

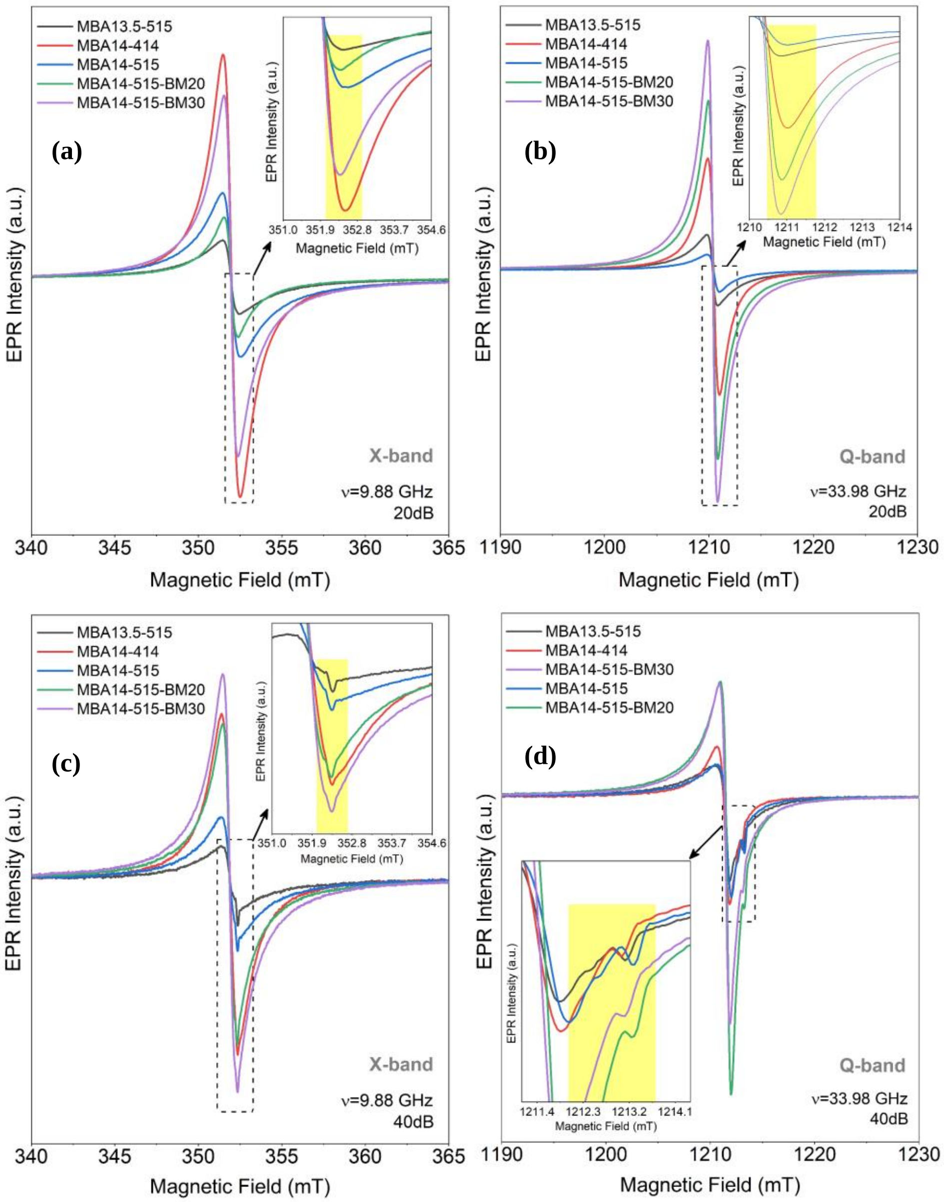

Figure 29. Room temperature X- and Q-band EPR spectra of the synthesized $B_4C$ powders measured at power attenuations of (a-b) 20 dB and (c-d) 40 dB. Signals from core defects are highlighted with yellow and shown in insets.

# CHAPTER 6. BORON CARBIDE AND ZINC OXIDE BASED ALL-IN-ONE SUPERCAPACITOR DEVICES

## 6.1. Electrochemical Characterization and Device Assembly

The fundamental processes involved in the electrochemical energy storage can take place at the (sub)surface of the electrodes or at the electrode/electrolyte interface. EIS is an important tool to analyze a circuit's ability to resist the electrical current flow, that is, resistance and impedance. Analyzing the current response in high and low frequencies is useful to differentiate the ionic and electronic processes. CV, on the other hand, provides basic information about the voltage window of the fabricated devices, oxidation and reduction potentials of the electrodes, and the type of energy storage mechanisms from the shape of the CV curve [112]. The gravimetric specific capacitance ($C_s$, F.g$^{-1}$) can be calculated from CV using Eq. 8 [113]:

$$C_s = \frac{A}{\Delta V \times v \times m} \tag{8}$$

where $A$ is the integrated area of the CV curve (A.V), $\Delta V$ is the potential window (V), $v$ is the scan rate (V.s$^{-1}$) and $m$ is the mass of the active electrode materials (g). Another way of calculation of the gravimetric specific capacitance is from the galvanostatic charge-discharge (GCD) curves using Eq. 9 or 10 [114, 115]:

$$C_s = \frac{I \times \Delta t}{\Delta V \times m} \tag{9}$$

or

$$C_s = \frac{Q_{ch/disch}}{\Delta V \times m} \tag{10}$$

where $I/m$ is the current density (A.g$^{-1}$, $I$: the charge/discharge current, $m$: mass of the active electrode material), $\Delta t$ is the full discharge time (s$^{-1}$), $\Delta V$ is the change in voltage between the initial and final potential either on charging or discharging process (V), and $Q_{ch/disch}$ is the total charge stored or released by the SC. In this dissertation, the specific capacitances and gravimetric energy and power densities of the assembled SC devices were obtained from the GCD curves.

Electrochemical performance of the $B_4C$ and ZnO based electrode materials and the fabricated symmetric and asymmetric SC devices were characterized by using a multichannel BioLogic VMP 300 potentiostat in a two-electrode configuration with a custom-made SC device designed by our research group as shown in Fig. 30. An aqueous solution of 6 M KOH and a non-aqueous (organic) 1.0 M $LiPF_6$ in EC/DEC=50/50 (v/v) (i.e., a lithium salt dissolved in an organic solvent mixture) were chosen as the electrolytes to the effect of different types of electrolytes on the charge storage behavior of the electrodes and to observe the synergistic effects of $B_4C$ and ZnO in different electrolytes. In a typical SC device, stainless steel screws were used as the current collectors on both sides, and a porous glass fiber paper (Whatman, grade GF/F) was used as a separator after wetting it with the selected electrolyte. The synthesized $B_4C$ and ZnO powders were directly used as electrodes for all-in-one symmetric and asymmetric SC devices without any further treatment. No binders or additives were used in preparation of the electrodes.

All the tests was performed at room temperature using cyclic voltammetry (CV), potentiostatic electrochemical impedance spectroscopy (PEIS, or EIS), and galvanostatic cycling with potential limitation (GCPL) techniques. CV profiles were recorded for 100 cycles at various scan rates from 10 to 200 $mV.s^{-1}$ over the voltage range of 0 to +1 V and 0 to +3 V for the devices assembled in the aqueous and organic electrolytes, respectively. The EIS measurements were carried out at open circuit voltage by applying a sinusoidal signal of 10 mV in the frequency range from 10 mHz to 1 MHz. GCPL was performed at a scan rate of 100 mV/s at various specific currents of 0.1 A/g, 0.2 A/g, 0.3 A/g, 0.5 A/g and 2.5 A/g for 100 cycles.

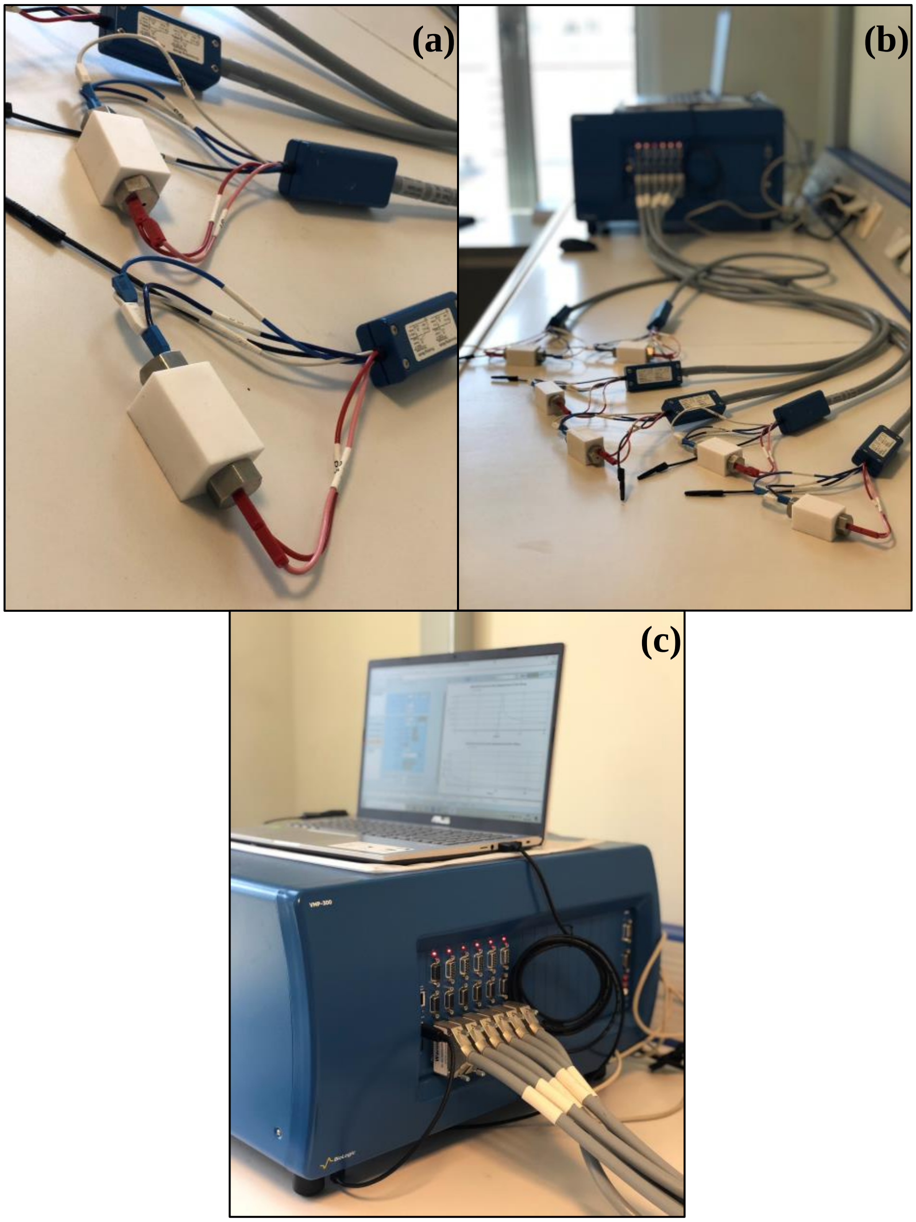

Figure 30. Supercapacitor devices and the testing equipment used for the electrochemical analysis of supercapacitors: (a) custom-made SC device in a two-electrode configuration, (b) simultaneous testing of SCs, and (c) BioLogic VMP 300 potentiostat with six-channels.

### 6.2. Symmetric Supercapacitors

A simple device architecture was designed and used for the assembly of all-in-one SCs. In a symmetric two-electrode cell configuration, $B_4C$ powders were directly used as electrodes on each side in contact with the stainless steel current collectors and the glass fiber separator wetted with an electrolyte, as illustrated in Fig. 31. The fabricated symmetric SC devices consist of $B_4C$ electrodes synthesized with different mannitol-to-boric acid molar ratios and at different temperatures (see Table 2 for the synthesis conditions). The cell components are listed in Table 5. The devices were tested both in the aqueous (6 M KOH) and the organic (1 M $LiPF_6$ in EC/DEC=50/50 (v/v)) electrolytes, and the results were compared.

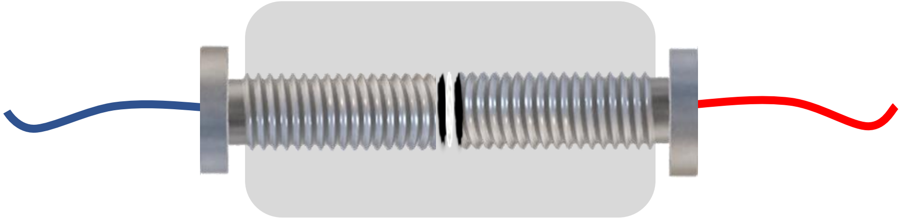

Figure 31. Illustration of a symmetric cell assembly. (Black: $B_4C$ electrode, white: glass fiber separator.)

Table 5. Cell components of all-in-one symmetric ($B_4C$/$B_4C$) supercapacitors.

| Device number | Electrode material 1 (E1) | Electrode material 2 (E2) | Electrolyte (EL) | Separator (S) | SC Type |
|---|---|---|---|---|---|
| **SC1** | $B_4C$ (MBA14-414) | $B_4C$ (MBA14-414) | 6 M KOH | Glass fiber | Symmetric |
| **SC2** | $B_4C$ (MBA14-414) | $B_4C$ (MBA14-414) | 1 M $LiPF_6$ | Glass fiber | Symmetric |
| **SC3** | $B_4C$ (MBA13.5-515) | $B_4C$ (MBA13.5-515) | 6 M KOH | Glass fiber | Symmetric |
| **SC4** | $B_4C$ (MBA13.5-515) | $B_4C$ (MBA13.5-515) | 1 M $LiPF_6$ | Glass fiber | Symmetric |
| **SC5** | $B_4C$ (MBA14-515) | $B_4C$ (MBA14-515) | 6 M KOH | Glass fiber | Symmetric |
| **SC6** | $B_4C$ (MBA14-515) | $B_4C$ (MBA14-515) | 1 M $LiPF_6$ | Glass fiber | Symmetric |

### 6.3. Asymmetric Supercapacitors

The asymmetric SCs were assembled in the same way as the symmetric ones, except that this time the selected electrodes were used at the opposite sides of the SC device. The synthesized $B_4C$ powder (MBA14-515) and ZnO powders (unmilled and ball milled) were directly used as electrodes without mixing with any conductive additives and/or binders. In addition to the unmilled (bulk) ZnO, 2 hours and 4 hours ball milled ZnO powders were prepared as described in Chapter 2 and assembled into an asymmetric device. A comparison was made for each test between the devices assembled in the aqueous (6 M KOH) and the organic (1 M $LiPF_6$ in EC/DEC=50/50 (v/v)) electrolytes to evaluate the synergistic effects of the electrodes, the effects of the intrinsic point defects created by the high energy ball milling process as well as the effects of particle size and active surface area on the energy storage performance of the devices. The schematic illustration of an asymmetric SC device assembly is shown in Fig. 32, and the cell components are listed in Table 6.

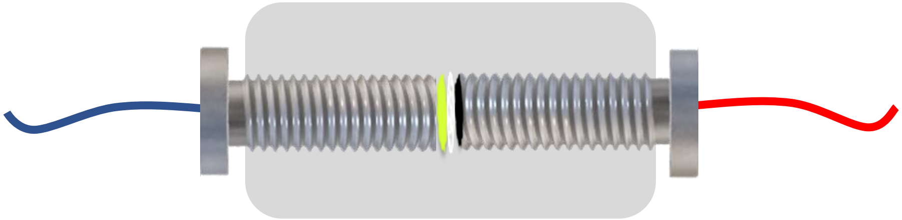

Figure 32. Illustration of an asymmetric cell assembly. (Green: ZnO electrode, black: $B_4C$ electrode, white: glass fiber separator.)

Table 6. Cell components of all-in-one asymmetric ($B_4C$/ZnO) supercapacitors.

| **Device number** | **Electrode material 1 (E1)** | **Electrode material 2 (E2)** | **Electrolyte (EL)** | **Separator (S)** | **SC Type** |
|---|---|---|---|---|---|
| **ASC1** | ZnO (bulk) | $B_4C$ (MBA14-515) | 6 M KOH | Glass fiber | Asymmetric |
| **ASC2** | ZnO (bulk) | $B_4C$ (MBA14-515) | 1 M $LiPF_6$ | Glass fiber | Asymmetric |
| **ASC3** | ZnO-2h | $B_4C$ (MBA14-515) | 6 M KOH | Glass fiber | Asymmetric |
| **ASC4** | ZnO-2h | $B_4C$ (MBA14-515) | 1 M $LiPF_6$ | Glass fiber | Asymmetric |
| **ASC5** | ZnO-4h | $B_4C$ (MBA14-515) | 6 M KOH | Glass fiber | Asymmetric |
| **ASC6** | ZnO-4h | $B_4C$ (MBA14-515) | 1 M $LiPF_6$ | Glass fiber | Asymmetric |

## 6.4. Results and Discussions

### 6.4.1. Investigation of electrochemical performance of the fabricated supercapacitor devices

#### 6.4.1.1. Electrochemical performance of symmetric SCs

$B_4C$, being a p-type semiconductor and an ultralight material with high chemical and thermal stability, has a promising potential as an electrode for electrochemical energy storage devices, especially SCs. It has an interesting crystal structure that can accommodate point defects (interstitials/vacancies) which significantly improves the electrochemical performance of the $B_4C$ electrodes, as previously discussed [60].

We firstly compared the electrochemical behavior of symmetric devices made of $B_4C$ powders synthesized with different processing parameters (see Table 5 for the device components). Then, we selected the most suited $B_4C$ sample as an electrode material for the preparation of asymmetric SC devices.

Fig. 33-35 shows the comparative pre- and post-CV Nyquist plots and corresponding fits for symmetric SCs. The fitting parameters are given in Appendix 1. As shown in Fig. 33(a) and 33(c), at high frequencies, pre-CV EIS profile of SC1 and SC2 exhibited ohmic (or series) resistances ($R_s$) of 0.58 and 10.85 Ω, respectively, which mostly due to the solution resistance (electrolyte) but also includes the intrinsic resistance of the electrode material, and the contact resistance between the electrode-current collector and the separator-electrode [116]. The lower $R_s$ of SC1 in an aqueous electrolyte (6 M KOH) than that of SC2 in an organic electrolyte (1 M $LiPF_6$) is expected due to the higher conductivity of the aqueous electrolytes [117]. Both equivalent circuits are combination of parallel RC in series, that is, a typical Randles circuit, and contain constant phase elements (CPE, Q) reflecting the non-ideal capacitor behavior which is common for EDLCs. No semicircle was observed, neither in high-frequency nor in mid-frequency domains in Fig. 33 (b) and 33 (d), again suggesting a double-layer capacitance instead of a Faradaic charge transfer, which is confirmed by the CV curves recorded at 10, 20, 50, 100 and 200 $mV.s^{-1}$ and presented in Fig. 33 (e) and (f). The quasi-rectangular shape of the CV curves with no visible redox peaks were maintained at each cycle (even at 200 mV.s$^{-1}$), indicating that the nature of the charge storage mechanism is dominated by the fast non-Faradaic processes [112].

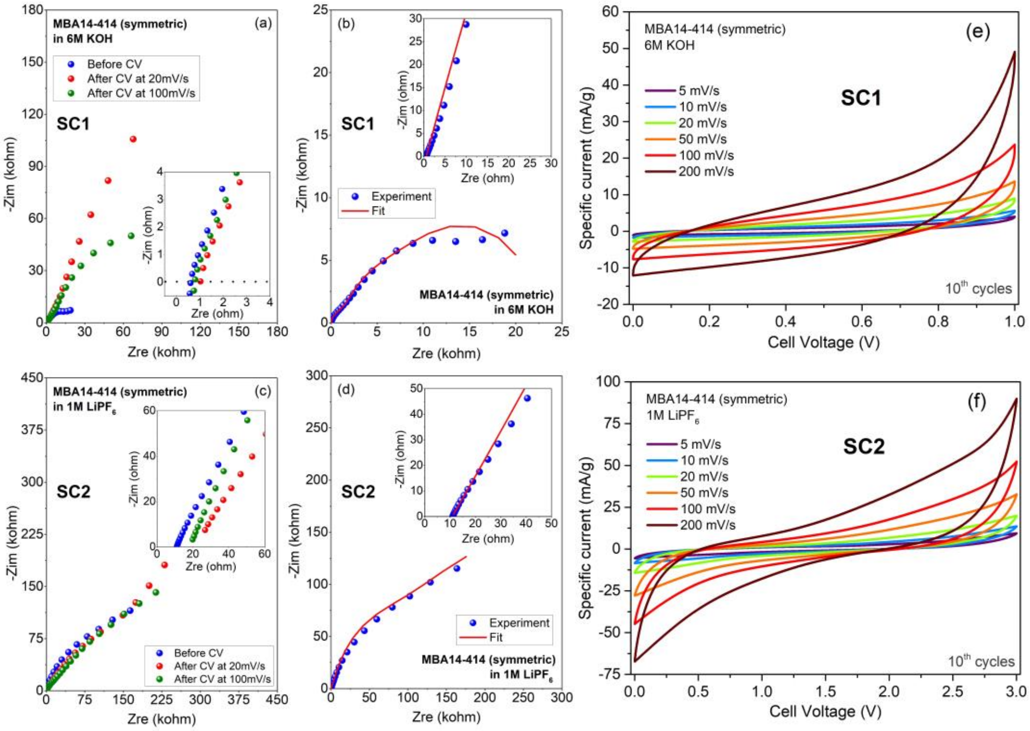

Figure 33. Comparison of the room temperature Nyquist plots and CV profiles of the symmetric SCs (SC1 and SC2) composed of $B_4C$ (MBA14-414) in different electrolytes: (a), (c) pre- and post-CV Nyquist plots, (b), (d) experimental and fitted Nyquist profiles; 10th CV cycles for SC1 and SC2 at scan rates between 10-200 mV.s$^{-1}$. The insets in (a-d) show the high frequency regions. The tests were carried out with (a), (b), (e) 6 M KOH and (c), (d), (f) 1 M $LiPF_6$ in EC/DEC=50/50 (v/v), respectively.

In Fig. 34 (a-b) and Fig. 35 (a-b), similar $R_s$ values of 0.60 Ω for SC3 and 0.55 Ω for SC5 were calculated to that of SC1 (0.58 Ω) in the aqueous electrolyte. For devices tested in the organic electrolyte, the $R_s$ was 18.47 Ω for SC4 and 19.96 Ω for SC6 (Fig. 34 (c-d) and Fig. 35 (c-d)). It should be noted that all the $R_s$ obtained for the symmetric SC devices (SC1 to SC6) made of bare $B_4C$ electrodes were significantly lower than that of the reported $R_s$ values for similar systems in literature [60, 78]. The rest of the fitting parameters were listed in Appendix 2 for SC3 and SC4, and in Appendix 3 for SC5 and SC6.

Unlike SC1, SC3 and SC5 provide small redox peaks in the aqueous 6 M KOH electrolyte, especially below 200 mV.s$^{-1}$, by preserving the quasi-rectangular shape of the CV curves at all scan rates, indicating a combination of EDLC and pseudocapacitance. These small redox peaks were ascribed to the central C atom with unpaired electrons in the three-atom chains in $B_4C$, which acts as an active site for the redox reactions. On the other hand, the pseudocapacitive contribution increases in SC6 with visible redox peaks in the pseudocapacitive CV curves, which is mainly attributed to the following reasons: i) presence of pure phase of $B_4C$ electrode without any impurities like amorphous/free C or $B_2O_3$, ii) decreased particle size, iii) increased active surface area, and iv) point defects (interstitials or vacancies in $B_4C$) which discussed in Chapter 5. Since the electrodes used in SC1 and SC2 were containing varying amounts of such impurities and less $B_4C$ phase, the pseudocapacitive character of the electrodes might be hindered by those impurities by blocking the access of ions to the redox active sites.

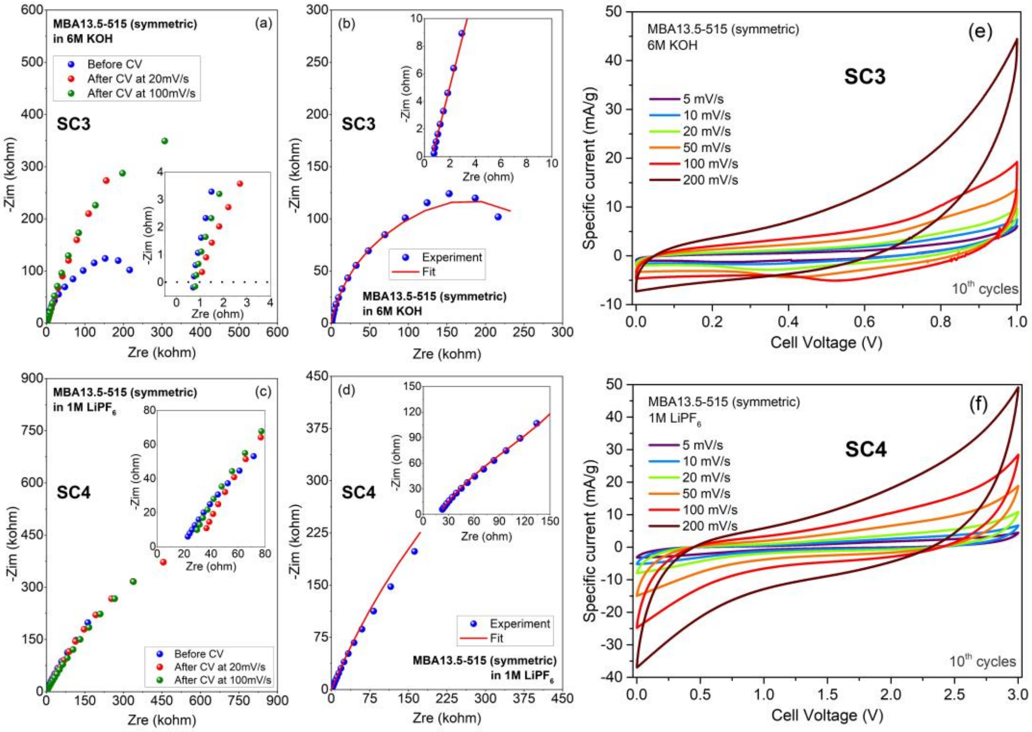

Figure 34. Comparison of the room temperature Nyquist plots and CV profiles of the symmetric SCs (SC3 and SC4) composed of $B_4C$ (MBA13.5-515) in different electrolytes: (a), (c) pre- and post-CV Nyquist plots, (b), (d) experimental and fitted Nyquist profiles; 10th CV cycles for SC3 and SC4 at scan rates between 10-200 mV.s$^{-1}$. The insets in (a-d) show the high frequency regions. The tests were carried out with (a), (b), (e) 6 M KOH and (c), (d), (f) 1 M $LiPF_6$ in EC/DEC=50/50 (v/v), respectively.

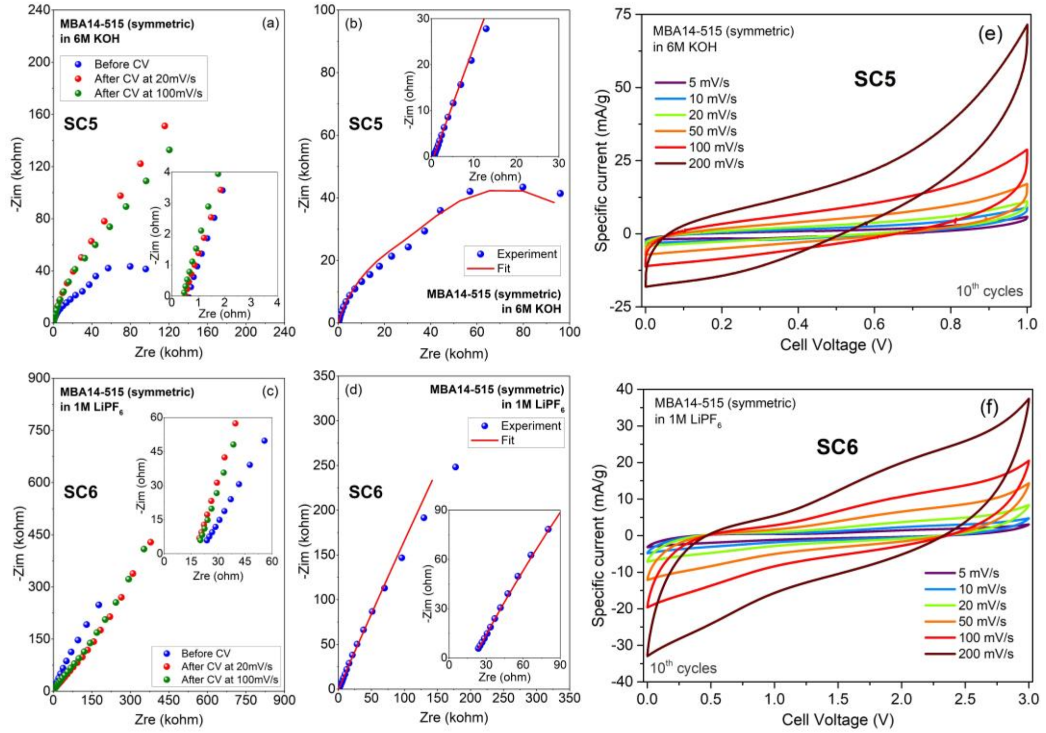

Figure 35. Comparison of the room temperature Nyquist plots and CV profiles of the symmetric SCs (SC5 and SC6) composed of $B_4C$ (MBA14-515) in different electrolytes: (a), (c) pre- and post-CV Nyquist plots, (b), (d) experimental and fitted Nyquist profiles; 10th CV cycles for SC5 and SC6 at scan rates between 10-200 $mV.s^{-1}$. The insets in (a-d) show the high frequency regions. The tests were carried out with (a), (b), (e) 6 M KOH and (c), (d), (f) 1 M $LiPF_6$ in EC/DEC=50/50 (v/v), respectively.

The charge-discharge performance of the $B_4C$ in aqueous and organic electrolytes were compared for devices SC5 and SC6 in Fig. 36 (a-d). The specific discharge capacity of the electrodes were more than doubled in the organic electrolyte (135.2 $\mu Ah.g^{-1}$) compared to that of in the aqueous one (67.2 $\mu Ah.g^{-1}$) at a current density of 0.1 $A.g^{-1}$, as shown in Fig. 36 (a-b). Fig. 36 (c) shows the last 10 cycles out of 100 galvanostatic charge-discharge cycles at current densities of 0.10, 0.15, 0.20, 0.50 and 2.40 $A.g^{-1}$ for SC5 and SC6. Both devices experienced a reduction in the specific discharge capacitance as the charge-discharge rate is increased from 0.1 to 2.4 $A.g^{-1}$ which ascribed to the increase in the internal resistance that slows down the charge transport. The highest specific discharge capacitances were found to be 114.1 $mF.g^{-1}$ and 81.7 $mF.g^{-1}$ for SC5 in the aqueous electrolyte and for SC6 in the organic electrolyte, respectively. The long term cycling performance of the SC5 and SC6 was tested in both electrolytes for 100 cycles at a current density of 0.10 A.g$^{-1}$. After 100 cycles, both SC5 and SC6 displayed excellent cycling stability with 97.5% and 98.3% retention of their initial capacities, respectively.

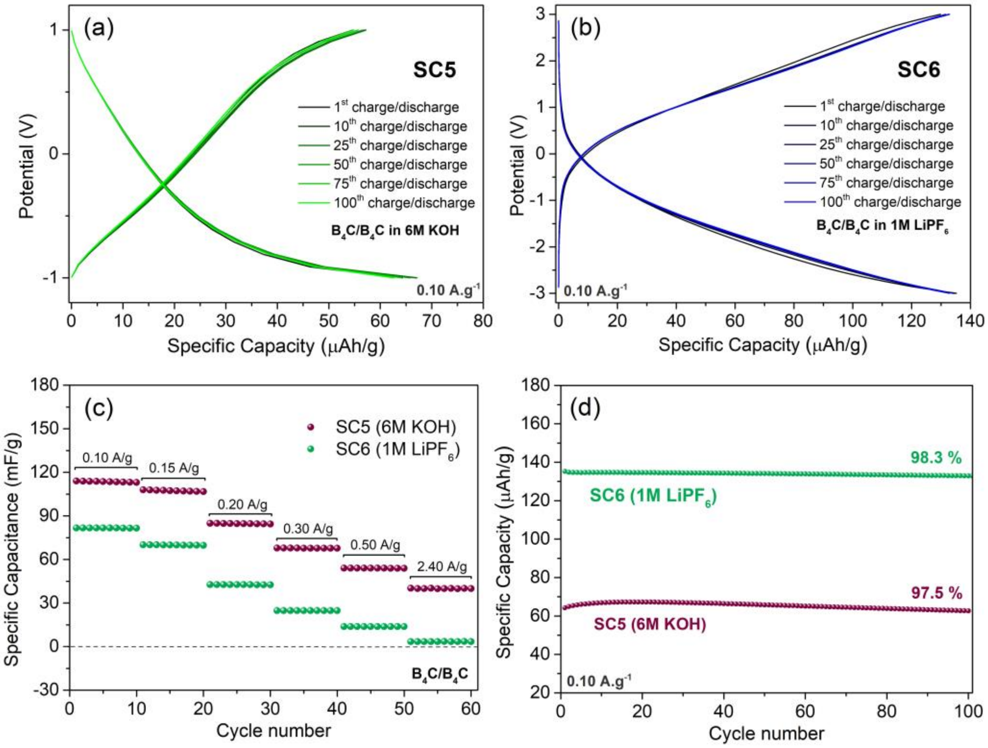

Figure 36. Electrochemical performance of the selected symmetric ($B_4C/B_4C$) SCs. Room temperature charge-discharge profiles of 1st, 10th, 25th, 50th, 75th, and 100th cycles at a current density of 0.10 A.g$^{-1}$ in (a) 6 M KOH (SC5) and (b) 1 M $LiPF_6$ in EC/DEC=50/50 (v/v) (SC6) electrolytes, respectively; (c) cycling stability of the last 10 cycles out of 100 cycles at current densities of 0.10, 0.15, 0.20, 0.30, 0.50 and 2.40 A.g$^{-1}$ for SC5 and SC6, and (d) long-term cycling performance for SC5 and SC6 at a current density of 0.10 A.g$^{-1}$ for 100 cycles.

In the light of above results and discussions, the sample referred as MBA14-515 with pure $B_4C$ phase was selected as the most suitable electrode for the fabrication of asymmetric SCs with ZnO.

#### 6.4.1.2. Electrochemical performance of asymmetric supercapacitors: Synergistic effects of $B_4C$ and ZnO

Electrochemical performance tests of the asymmetric SC devices made of $B_4C$ and unmilled (bulk), 2h and 4h ball milled ZnO electrodes were evaluated by CV, EIS and GCPL using a two-electrode electrochemical cell under the same test conditions with the symmetric ones, and the results were presented in Fig. 37-44. At first sight the Nyquist profiles of the asymmetric SCs seem to be similar with the symmetric SCs (SC5 and SC6), however, when measured in the organic electrolyte, ASC2, ASC4, and ASC6 delivered significantly improved capacitive properties than SC6. The $R_s$ of asymmetric SCs measured in the organic electrolyte were considerably decreased to 12, 10.12, and 10.62 Ω for ASC2 , ASC4, and ASC6 as shown in Fig. 37 (c-d), Fig. 38 (c-d), and Fig. 39 (c-d), respectively. The decrease in $R_s$ around 50% in comparison to that of SC6 (19.96 Ω) reflects the good synergistic effects of $B_4C$ and ZnO, and much better access of electrolyte ions to the electroactive surface through the conducting pathways provided by the intrinsic point defects both in $B_4C$ and ZnO. In addition, low series resistances were obtained for ASC1 (Fig. 37 (a-b)), ASC3 (Fig. 38 (a-b)), and ASC5 (Fig. 39 (a-b)) in the aqueous electrolyte with $R_s$ values of 0.86, 1.08, and 0.91 Ω, respectively. None of the asymmetric devices displayed a semicircle at high frequencies which confirms the low electron-transfer resistance and fast charge transfer at the electrodes. It should be noted that, fitting the experimental EIS data to an equivalent circuit model is not an easy process, and in some cases finding a perfect fit both at high and low frequency regions is not possible due to the unique electrochemical behavior of the real device. Although the closest possible matches were used, some of the fit curves presented in this dissertation did not perfectly fit at low frequencies but fitted perfectly at high frequency regions, therefore, the capacitance and the charge-transfer (or polarization) resistance calculated from the fits might be different to some degree than that of the real values. In this study, all the specific capacitance values were obtained from the charge-discharge tests.

The effect of electrolyte on the electrochemical behavior of the asymmetric SCs was depicted in CV curves presented in Fig. 37 (e) and (f) for ASC1 and ASC2, respectively. It is evident from the shape of the curves that ASC1 exhibits EDLC-dominant characteristics with very small pseudocapacitive contribution that resulted in the quasi-rectangular CV curves, whereas the CV curves for ASC2 were typical for pseudocapacitive charge storage process with noticeable redox peaks, especially at scan rates below 200 $mV.s^{-1}$. These results suggest that the surface redox reactions and the diffusion of $Li^+$ in ZnO were facilitated at lower scan rates which led to increased pseudocapacitive contribution, and the double-layer contribution was increased as the scan rate increased from 10 to 200 $mV.s^{-1}$.

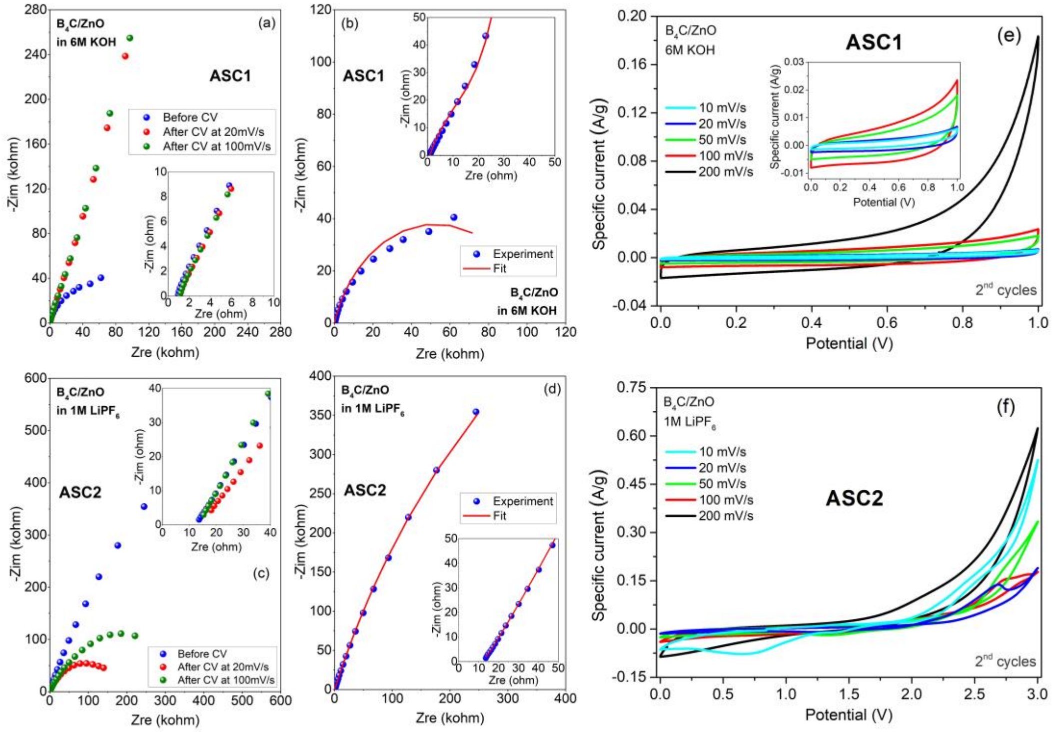

Figure 37. Comparison of the room temperature Nyquist plots and CV profiles of the asymmetric SCs (ASC1 and ASC2) based on B$_4$C and ZnO (bulk) in different electrolytes: (a), (c) pre- and post-CV Nyquist plots, (b), (d) experimental and fitted Nyquist profiles; 2$^{nd}$ CV cycles for ASC1 and ASC2 at scan rates between 10-200 mV.s$^{-1}$. The insets in (a-d) show the high frequency regions. The tests were carried out with (a), (b), (e) 6 M KOH and (c), (d), (f) 1 M LiPF$_6$ in EC/DEC=50/50 (v/v), respectively.

Similarly, ASC4 and ASC6 exhibited significantly better electrochemical performance in the organic electrolyte than that of the ASC3 and ASC5 in the aqueous electrolyte with remarkably increased peak currents compared to that of in 6 M KOH due to the wider potential window and increased pseudocapacitive contributions by the (sub)surface redox reactions accompanied with the capacitive double-layer characteristics, as shown in Fig. 38 (e)-(f) and Fig. 39 (e)-(f). An additional redox peak appeared between 2.65-2.80 V, indicating that fresh charge transfer pathways were provided for the electrolyte ions by the increased number of surface and core defects introduced in ZnO by the high strain during the high-energy ball-milling process [118]. These results are in good agreement with the EPR results that presented in Chapter 5, and strongly reflects the importance of the defects on the electrochemical performance of SC devices.

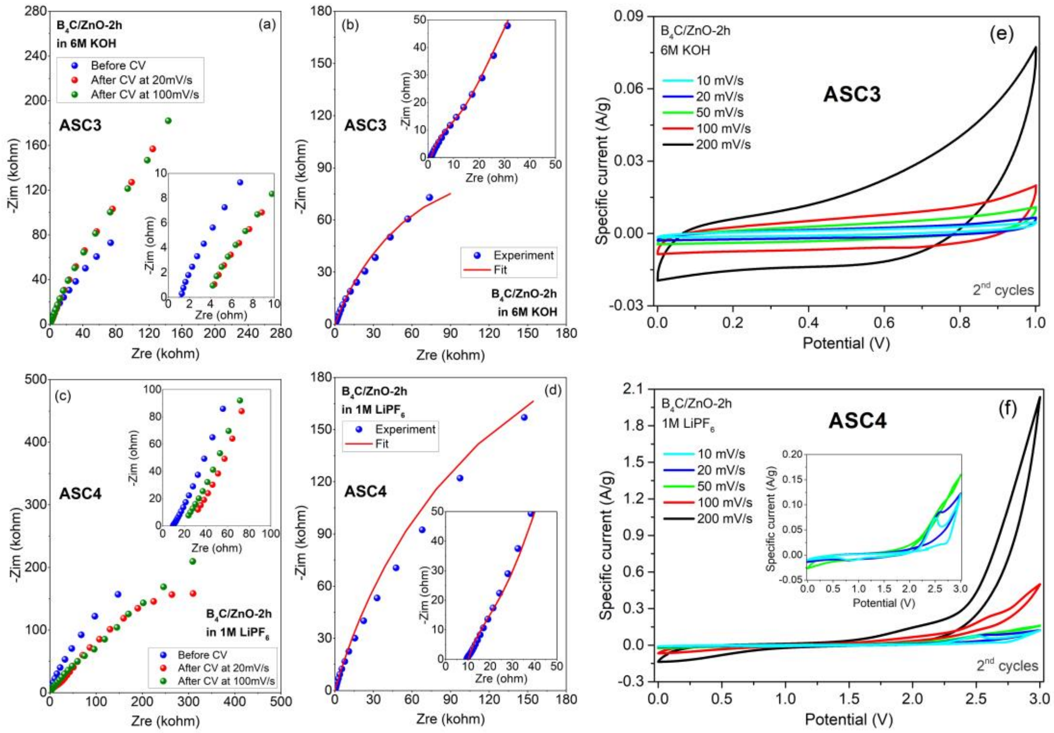

Figure 38. Comparison of the room temperature Nyquist plots and CV profiles of the asymmetric SCs (ASC3 and ASC4) based on $B_4C$ (MBA14-515) and 2 h ball milled ZnO (ZnO-2h) electrodes in different electrolytes: (a), (c) pre- and post-CV Nyquist plots, (b), (d) experimental and fitted Nyquist profiles; 2nd CV cycles for ASC3 and ASC4 at scan rates between 10-200 $mV.s^{-1}$. The insets in (a-d) show the high frequency regions. The tests were carried out with (a), (b), (e) 6 M KOH and (c), (d), (f) 1 M $LiPF_6$ in EC/DEC=50/50 (v/v), respectively.

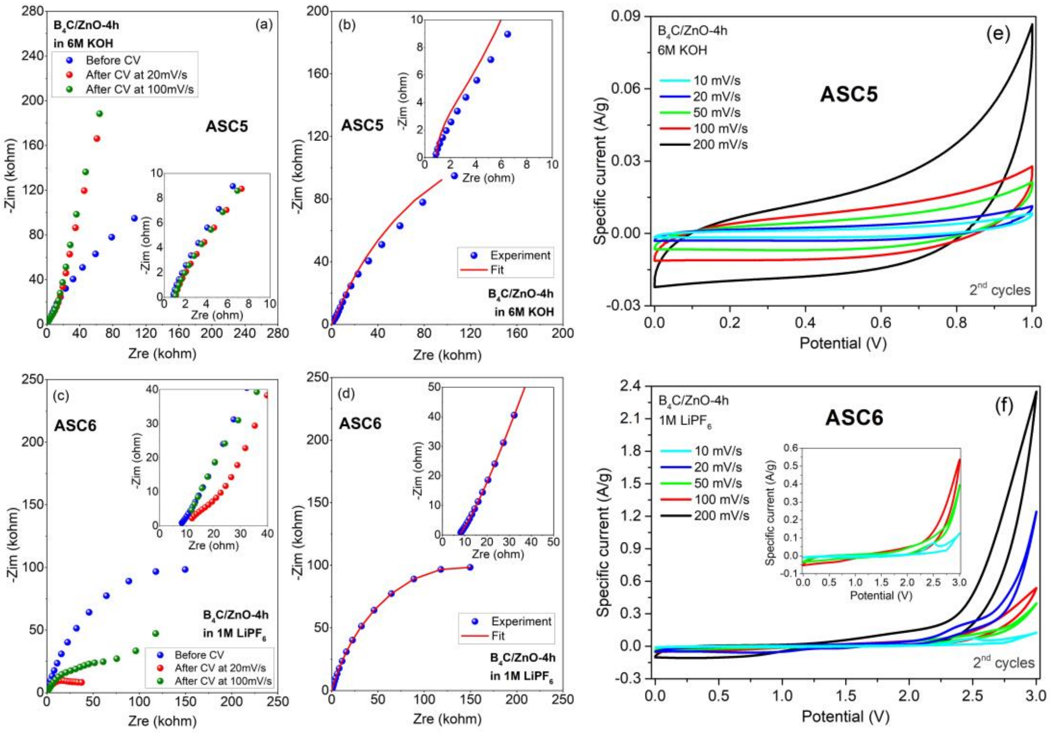

Figure 39. Comparison of the room temperature Nyquist plots and CV profiles of the asymmetric SCs (ASC5 and ASC6) based on $B_4C$ (MBA14-515) and 4 h ball milled ZnO (ZnO-4h) electrodes in different electrolytes: (a), (c) pre- and post-CV Nyquist plots, (b), (d) experimental and fitted Nyquist profiles; 2nd CV cycles for ASC5 and ASC6 at scan rates between 10-200 $mV.s^{-1}$. The insets in (a-d) show the high frequency regions. The tests were carried out with (a), (b), (e) 6 M KOH and (c), (d), (f) 1 M $LiPF_6$ in EC/DEC=50/50 (v/v), respectively.

Further investigation on the electrochemical energy storage performance of the asymmetric SC devices were conducted by galvanostatic charge/discharge analysis at various current densities from 0.10 $A.g^{-1}$ to 2.40 $A.g^{-1}$, and the results were presented in Fig. 40 and Fig 41. It is evident from the results displayed in Fig. 40 that there is a significant increase in the electrochemical performance for all the asymmetric devices measured in the 1 M $LiPF_6$ electrolyte compared to that of in 6 M KOH as expected from the previous results. The charge/discharge profiles for selected cycles were shown in Fig. 40 (a-b) for ASC1 and ASC2, in Fig. 40 (d-e) for ASC3 and ASC4, and in Fig. 40 (g-h) for ASC5 and ASC6 at 0.10 $A.g^{-1}$. The asymmetric devices prepared with 6 M KOH, namely ASC1, ASC3, and ASC5, kept great stability in charge/discharge cycles with a typical EDLC behavior, but the specific charge/discharge capacities were drastically lower than those in 1 M $LiPF_6$ which delivered initial specific charge/discharge capacities of 193.1/184.4, 270/233.5, and 307.2/295.1 μAh.g$^{-1}$ for ASC2, ASC4, and ASC6, respectively. After the 1st charge/discharge cycle, first increasing and subsequently decreasing charge/discharge trend was notable for ASC2. Furthermore, as shown in Fig. 40 (c), (f), and (i), the maximum $C_s$ values of 261.4, 142.1, and 298.6 mF.g$^{-1}$ were obtained for ASC2, ASC4, and ASC6, respectively, for the last 10 cycles (out of 100 cycles) at a current density of 0.15 A.g$^{-1}$, however with low stability. ASC2 exhibited the largest variation of $C_s$ at 0.15 A.g$^{-1}$ (Fig. 40(c)). Nevertheless, all the devices showed excellent long term cycling stability at 0.10 A.g$^{-1}$. The long term capacity retention was found to be 101.3, 99.9, and 100.3 % for ASC1, ASC3, and ASC5 in 6 M KOH, and 96.4, 87.2, and 93.8 % for ASC2, ASC4, and ASC6 in 1 M $LiPF_6$, respectively, after 100 cycles. The above mentioned fluctuations in specific capacity at 0.15 A.g$^{-1}$ were ascribed to the non-uniform particle distribution and agglomerate formation in the unmilled ZnO electrode (see Fig. 28, bottom inset) which may cause or facilitate instability at the electrode-electrolyte interphase hence the unstable charge/discharge behavior. It was noticed that the instabilities could still be observed but significantly reduced after 2 h and 4 h milling of ZnO due to the more homogeneous particle shape and size distributions as well as higher surface area obtained by the high-energy ball-milling process. Another important fact that needs to be pointed out is the intrinsic defect property of the unmilled and milled ZnO electrodes which plays a key role in enhancing the electrochemical performance of the electrodes, as discussed in our previous publications [30, 60, 119]. With increased milling time, the concentration of the ball milling induced intrinsic point defects (i.e., oxygen and zinc vacancies) in ZnO was increased, which promotes the electrolyte ion transport into the electrode by shortening the ion transport paths and/or by providing extra pathways for the ion transport. The comparative spectra of the 2nd charge/discharge cycles of the fabricated SC devices at 0.10 A.g$^{-1}$ clearly showed that, in 6 M KOH (Fig. 40(k)), both symmetric and asymmetric devices delivered EDLC-dominant characteristics of $B_4C$ with small pseudocapacitive contributions, whereas in 1 M $LiPF_6$ (Fig. 40(l)), the energy storage mechanism is based on mixed Faradaic and non-Faradaic contributions from ZnO and $B_4C$, respectively. After 100 cycles, the maximum $C_s$ retention of 101.4 % was obtained for ASC1, followed by 100.3, 99.9, 98.3, 97.5, 96.5, 93.8, and 87.2 % for ASC3, ASC5, SC6, SC5, ASC2, ASC6, and ASC4, respectively (Fig. 41(a)). Coulombic efficiencies were found to be

114.1 % for SC5, 101.5 % for ASC1, 101.0 % for SC6 and ASC4, 100.8 % for ASC5, 98.7 % for ASC2, 98.1 % for ASC4 and 96.0 % for ASC6. Both $C_s$ retention and coulombic efficiency were obtained after 100 cycles at a current density of 0.10 $A.g^{-1}$.

Energy density (ED) and the power density (PD) are the two of the most important properties of SCs that measures the overall performance of the SC devices. In the simplest term, ED indicates the total energy/charges that can be stored per unit volume/mass of a SC, whereas PD represents how fast the stored energy can be delivered. The volumetric ED is expressed in watt-hours per liter ($W.h.L^{-1}$) whereas the gravimetric ED (i.e., specific energy) is expressed as watt-hours per kilogram ($W.h.kg^{-1}$). For the PD, watt per liter ($W.L^{-1}$) represents the volumetric PD whereas watt per kilogram ($W.kg^{-1}$) is used for the gravimetric PD. In Fig. 41(c), a Ragone plot was constructed to evaluate the performance and the practical applicability of our all-in-one SC devices by calculating their gravimetric ED and PD from the galvanostatic charge/discharge curves at a current density of 0.1 $A.g^{-1}$. The grey color area in Fig. 41(c) shows the energy and power density ranges of previously reported SC systems [9]. Our symmetric devices SC5 and SC6 delivered PD of 142.7 and 298.3 $W.kg^{-1}$, and ED of 0.036 and 0.261 $W.h.kg^{-1}$, respectively. The asymmetric SCs in 6 M KOH exhibited worse performance than that of the SC5 with ED of 0.014, 0.006, and 0.010 $W.h.kg^{-1}$, and PD of 99.8, 100.0, and 99.7 $W.kg^{-1}$ for ASC1, ASC3, and ASC5, respectively. The maximum ED and PD were delivered by the asymmetric devices prepared with 1 M $LiPF_6$, which is expected in accordance with the previous results, with maximum ED of 0.39, 0.56, and 0.52 $W.h.kg^{-1}$, and PD of 299.7, 299.9 and 299.8 $W.kg^{-1}$ for ASC2, ASC4, and ASC6, respectively. It should be noted that no carbonaceous active materials or additives were incorporated into electrodes to boost the supercapacitor performances. These ED and PD values may seem low, especially if compared with the carbon-based systems, but taking into consideration the very low amounts used in the assembly of the SCs (~1 mg) without any binders or additives, they are quite good for such SC devices assembled only with as-synthesized boron carbide and metal oxide based ceramic electrodes. Here, we designed the supercapacitors only from the synthesized $B_4C$ and ZnO (0, 2, 4 h milled) nanomaterials without any carbon booster to investigate their naked capacitor behavior as well as the synergistic effects. Most conventional capacitors contain carbon materials as electrodes to increase the conductivity as well as the number of charges at the electrode-electrolyte interface due to their porous structure and high surface area. Our aim here is to open a door for future studies for the development of long-life, durable, chemically and thermally stable type electrode materials for supercapacitors by improving the material properties according to the area of interest.

These results clearly reflect i) the improved synergistic effects of the $B_4C$ and ZnO electrode materials in 1 M $LiPF_6$, ii) the importance of electrolyte selection to reveal the capacitive performance and the charge storage mechanism of the electrode materials, iii) the increased charge/discharge performance of the electrode materials with higher defect concentrations, and iv) the synergistic effects of non-Faradaic (i.e., EDLC) from $B_4C$ and Faradaic (pseudocapacitance) contributions from ZnO.

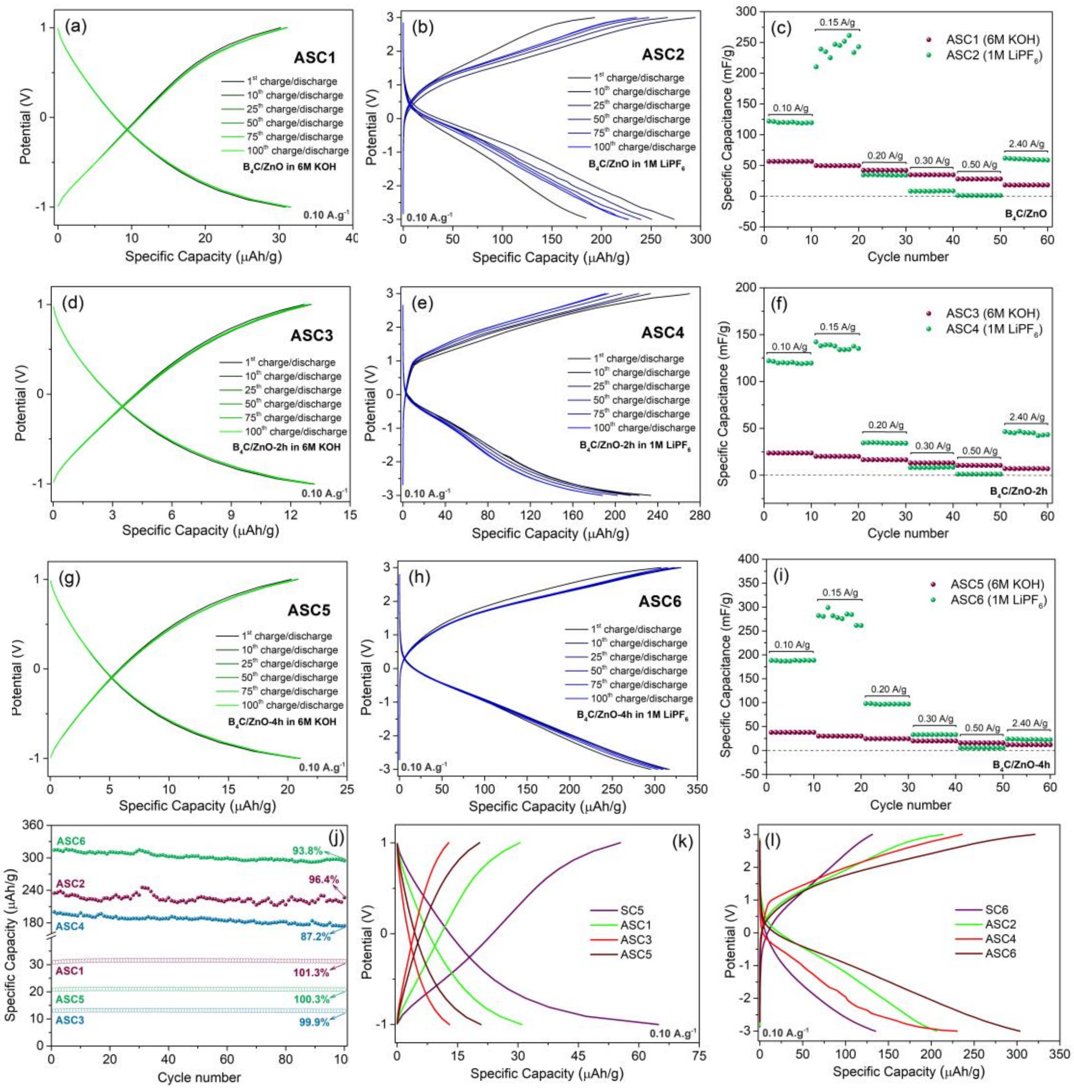

Figure 40. Charge/discharge curves of the last 10 cycles out of 100 cycles for (a) ASC1 ($B_4C$/unmilled ZnO in 6 M KOH), (b) ASC2 ($B_4C$/unmilled ZnO in 1 M $LiPF_6$ in EC/DEC=50/50 (v/v)), (d) ASC3 ($B_4C$/2 h HEBM ZnO in 6 M KOH), (e) ASC4 ($B_4C$/2 h HEBM ZnO in 1 M $LiPF_6$ in EC/DEC=50/50 (v/v)), (g) ASC5 ($B_4C$/4 h HEBM ZnO in 6 M KOH), (h) ASC6 ($B_4C$/4 h HEBM ZnO in 1 M $LiPF_6$ in EC/DEC=50/50 (v/v)) at a current density of 0.10 $A.g^{-1}$; specific discharge capacitances for (c) ASC1 and ASC2, (f) ASC3 and ASC4, (i) ASC5 and ASC6 at current densities of 0.10, 0.15, 0.20, 0.30, 0.50, and 2.40 $A.g^{-1}$; (j) long-term cycling stability of ASC1, ASC2, ASC3, ASC4, ASC5, and ASC6 at a current density of 0.10 $A.g^{-1}$ for 100 cycles; comparison of the 2nd charge/discharge curves of the fabricated symmetric and asymmetric devices in the (k) 6 M KOH (SC5, ASC1, ASC3, and ASC5), and (l) 1 M $LiPF_6$ in EC/DEC=50/50 (v/v) (SC6, ASC2, ASC4, and ASC6) at a current density of 0.1 $A.g^{-1}$.

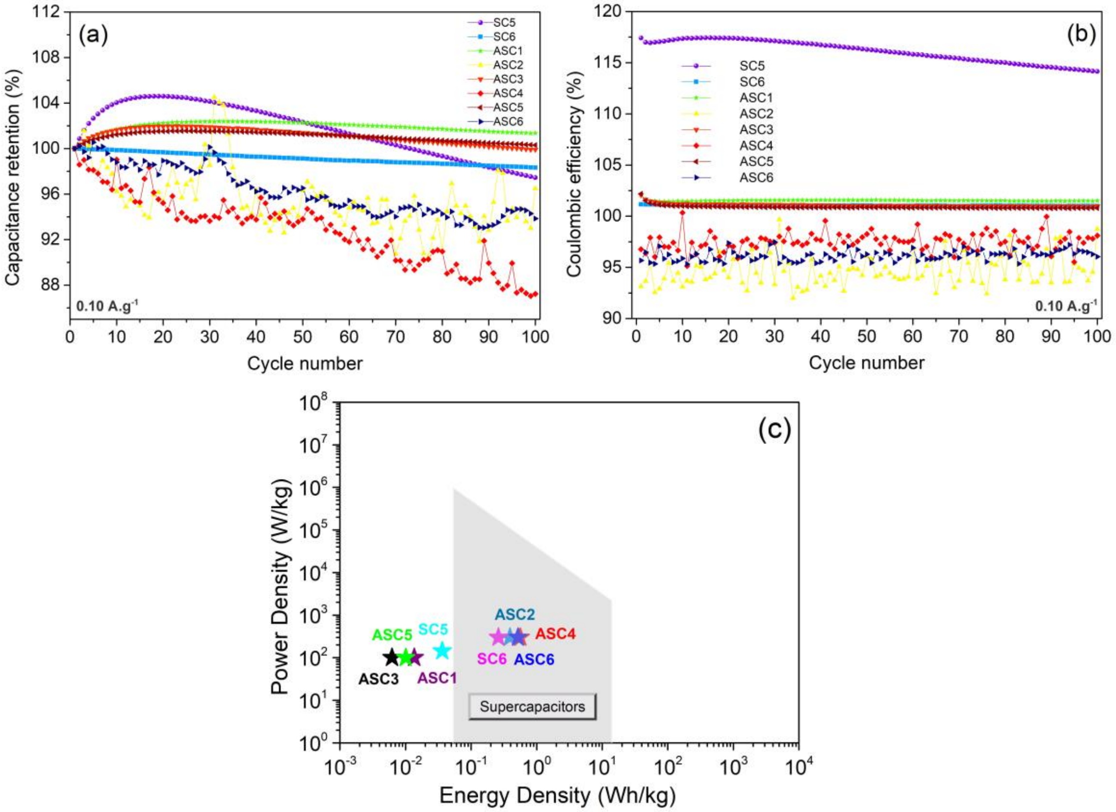

Figure 41. Comparison of the (a) capacitance retentions and (b) coulombic efficiencies of the selected symmetric (SC5 and SC6) and asymmetric (ASC1, ASC2, ASC3, ASC4, ASC5, ASC6) SC devices under repeated cycling at a current density of 0.10 A.g$^{-1}$ for 100 cycles; (c) Ragone plot of the fabricated symmetric and asymmetric devices for the comparison of the values with the energy and power density range of the supercapacitors .

# CHAPTER 7. CONCLUSIONS AND FUTURE WORK

$B_4C$, or boron carbides ($B_xC_{1-x}$) in general, has been subjected to the intensive studies for almost 90 years, however, the debate on its atomic structure, electronic properties and electrochemical behavior is still open. Its main use is generally as a bulk sintered material in military, space, nuclear, and industrial wear applications due to its superior properties including very high hardness, stability in harsh chemical environments and at extremely high temperatures, and high cross-section that provides the ability of capturing thermal neutrons. While the difficulties of obtaining $B_4C$ stoichiometry, the complex atomic structure and the need of high sintering temperatures (>2000 ℃) to produce bulk materials from its elements with conventional methods have been obstacles to its widespread use, its p-type semiconducting character, defect-induced atomic structure, long term stability in both acidic and basic environments, good thermoelectric properties and the abundance of its constituent elements make it to be a promising electrode material for SCs.

The everyday increasing energy demands can only be satisfied and sustained for the long run by the development of electrodes from sustainable materials for high-performance energy storage devices. Therefore, in Chapter 3, we focused on proposing a facile technique for the synthesis of $B_4C$, which is one of the most strategically important materials both in Turkey and in the world, and extending its application to the various energy storage systems, especially as an electrode material for SCs. A modified sol-gel technique was employed both to decrease the production temperature and to synthesize a highly crystalline powder with $B_4C$ stoichiometry by adjusting the molar ratio of boron and carbon sources. Heat treatment temperatures were kept between 400 and 500 ℃ for calcination, and 1400-1500 ℃ to produce the final $B_4C$ powder. In the Chapter 4, extensive characterization were carried out to monitor the thermal behavior and the structural evolutions of the precursors upon heating, and the $B_4C$ phase and the lattice parameters including atomic positions of the synthesized $B_4C$ crystals were identified. Furthermore, the defective properties of $B_4C$ were revealed, and the results were compared with the literature. In the Chapter 5, the electronic properties and the origin of the point defects were analyzed using advanced characterization techniques by taking advantage of the spin magnetic moments arising from the unpaired electrons within the crystal structure. Finally, in Chapter 6, an application of as-synthesized $B_4C$ and ZnO powders as electrodes in symmetric and asymmetric SCs was presented. All-in-one SC devices were prepared in a two-electrode configuration either in 6 M KOH or 1 M $LiPF_6$ electrolytes to investigate the effects of the electrolytes on the electrochemical performance. The synergistic effects between $B_4C$ and ZnO and the effects of point defects on the electrochemical performance of SCs were discussed. The symmetric SC based on $B_4C$ electrodes (SC5 and SC6) exhibited specific capacities of 65 and 135 $\mu Ah.g^{-1}$ in 6 M KOH and 1 M $LiPF_6$ electrolytes, respectively. The specific capacity of asymmetric SCs composed of $B_4C$ and 0, 2 and 4h ball-milled ZnO electrodes were calculated as 32, 13.2, and 21 $\mu Ah.g^{-1}$ for ASC1 ($B_4C$/ZnO), ASC3 ($B_4C$/ZnO-2h) and ASC5 ($B_4C$/ZnO-4h) in 6 M KOH, and as 273, 233 and 317 $\mu Ah.g^{-1}$ for ASC2 ($B_4C$/ZnO), ASC4 ($B_4C$/ZnO-2h) and ASC6 ($B_4C$/ZnO-4h) in 1 M $LiPF_6$, respectively. These values indicate that the specific capacities were increased by almost 202 %, 173 % and 235 %, in ASC2, ASC4 and ASC6 compared to SC6. The electrochemical data also shown that the specific discharge capacitances of the asymmetric SCs composed of $B_4C$ and 0, 2 and 4h ball-milled ZnO electrodes were improved by 149, 149, and 231 % at 0.1 $A.g^{-1}$, and 318, 173, and 365 % at 0.15 $A.g^{-1}$ for ASC2, ASC4 and ASC6, respectively, compared to the symmetric device composed of $B_4C$ electrodes at both sides (SC6), indicating the excellent synergistic effects of $B_4C$ and ZnO electrodes. Furthermore, as the defect concentration of ZnO is increased, a remarkable increase in the electrochemical performance of the ASCs is observed, proving the significant effects of defects on the energy storage performance thereby on the electrochemical behavior of the electrodes.

Overall, the SCs are one of the most important technologies that will play a key role for both today’s and the future’s energy systems due to their very high specific capacities, long life cycles and outstanding power densities. Only drawback is their insufficient energy densities which needs to be further improved by developing novel electrode materials. Development of the electrodes from abundant elements such as boron is of crucial importance for the sustainability of the produced energy storage systems. In this dissertation, the aim was to investigate the capacitive properties of the pure defect-induced $B_4C$, to understand the synergistic effects between $B_4C$ and ZnO nanoparticles, and to reveal the role of defects on the electrochemical properties, therefore no binders or additives for boosting the SCs' performance (such as carbonaceous species) were used in the preparation of the cells. By changing the synthesis route, doping with metal or rare-earth ion, or producing $B_4C$ based composites could be future approaches to improve the electrochemical performance of $B_4C$. This study opens a door for future studies on the use of boron-based materials, especially $B_4C$, in energy storage applications and proves the importance of defects on the SCs' electrochemical performances.

# REFERENCES

1. Dresselhaus, M.S. and I.L. Thomas, *Alternative energy technologies.* Nature, 2001. 414(6861): p. 332-337.
2. Hadjipaschalis, I., A. Poullikkas, and V. Efthimiou, *Overview of current and future energy storage technologies for electric power applications.* Renewable & Sustainable Energy Reviews, 2009. 13(6-7): p. 1513-1522.
3. Drury, E., P. Denholm, and R. Sioshansi, *The value of compressed air energy storage in energy and reserve markets.* Energy, 2011. 36(8): p. 4959-4973.
4. Abas, N., A. Kalair, and N. Khan, *Review of fossil fuels and future energy technologies.* Futures, 2015. 69: p. 31-49.
5. European, C., et al., *Study on energy storage : contribution to the security of the electricity supply in Europe*. Publications Office, 2020.
6. Goodenough, J.B., *Energy storage materials: A perspective.* Energy Storage Materials, 2015. 1: p. 158-161.
7. Chu, S., Y. Cui, and N. Liu, *The path towards sustainable energy.* Nature Materials, 2017. 16(1): p. 16-22.
8. Raza, W., et al., *Recent advancements in supercapacitor technology.* Nano Energy, 2018. 52: p. 441-473.
9. Winter, M. and R.J. Brodd, *What are batteries, fuel cells, and supercapacitors?* Chemical Reviews, 2004. 104(10): p. 4245-4269.
10. Xie, J., et al., *Puzzles and confusions in supercapacitor and battery: Theory and solutions.* Journal of Power Sources, 2018. 401: p. 213-223.
11. Simon, P., Y. Gogotsi, and B. Dunn, *Where Do Batteries End and Supercapacitors Begin?* Science, 2014. 343(6176): p. 1210-1211.
12. Hatzell, K.B., et al., *Flowable Conducting Particle Networks in Redox-Active Electrolytes for Grid Energy Storage.* Journal of the Electrochemical Society, 2015. 162(5): p. A5007-A5012.
13. Nomoto, S., et al., *Advanced capacitors and their application.* Journal of Power Sources, 2001. 97-8: p. 807-811.

14. Jung, D.Y., et al., *Development of ultracapacitor modules for 42-V automotive electrical systems.* Journal of Power Sources, 2003. 114(2): p. 366-373.

15. Simon, P. and Y. Gogotsi, *Materials for electrochemical capacitors.* Nature Materials, 2008. 7(11): p. 845-854.

16. Wu, Y. and C.B. Cao, *The way to improve the energy density of supercapacitors: Progress and perspective.* Science China-Materials, 2018. 61(12): p. 1517-1526.

17. Najib, S. and E. Erdem, *Current progress achieved in novel materials for supercapacitor electrodes: mini review.* Nanoscale Advances, 2019. 1(8): p. 2817-2827.

18. Pandolfo, A.G. and A.F. Hollenkamp, *Carbon properties and their role in supercapacitors.* Journal of Power Sources, 2006. 157(1): p. 11-27.

19. Taberna, P.L., C. Portet, and P. Simon, *Electrode surface treatment and electrochemical impedance spectroscopy study on carbon/carbon supercapacitors.* Applied Physics a-Materials Science & Processing, 2006. 82(4): p. 639-646.

20. Frackowiak, E., *Carbon materials for supercapacitor application.* Physical Chemistry Chemical Physics, 2007. 9(15): p. 1774-1785.

21. Zhou, Y.S., et al., *High-performance symmetric supercapacitors based on carbon nanotube/graphite nanofiber nanocomposites.* Scientific Reports, 2018. 8.

22. Portet, C., et al., *High power density electrodes for carbon supercapacitor applications.* Electrochimica Acta, 2005. 50(20): p. 4174-4181.

23. Balducci, A., et al., *High temperature carbon-carbon supercapacitor using ionic liquid as electrolyte.* Journal of Power Sources, 2007. 165(2): p. 922-927.

24. Dericiler, K., et al., *Upcycling process of transforming waste coffee into spherical graphene by flash pyrolysis for sustainable supercapacitor manufacturing with virgin graphene electrodes and its comparative life cycle assessment.* Biomass Conversion and Biorefinery, 2022.

25. Shaikh, N.S., et al., *Novel electrodes for supercapacitor: Conducting polymers, metal oxides, chalcogenides, carbides, nitrides, MXenes, and their composites with graphene.* Journal of Alloys and Compounds, 2022. 893.

26. Janotti, A. and C.G. Van de Walle, *Fundamentals of zinc oxide as a semiconductor.* Reports on Progress in Physics, 2009. 72(12).

27. Theerthagiri, J., et al., *A review on ZnO nanostructured materials: energy, environmental and biological applications.* Nanotechnology, 2019. 30(39).

28. Erdem, E., *Microwave power, temperature, atmospheric and light dependence of intrinsic defects in ZnO nanoparticles: A study of electron paramagnetic resonance (EPR) spectroscopy.* Journal of Alloys and Compounds, 2014. 605: p. 34-44.

29. Ammar, A.U., et al., *ZnO and MXenes as electrode materials for supercapacitor devices.* Beilstein Journal of Nanotechnology, 2021. 12: p. 49-57.

30. Buldu-Akturk, M., et al., *ZnO and reduced graphene oxide electrodes for all-in-one supercapacitor devices.* Nanoscale, 2022. 14(8): p. 3269-3278.

31. Subramani, K. and M. Sathish, *Facile synthesis of ZnO nanoflowers/reduced graphene oxide nanocomposite using zinc hexacyanoferrate for supercapacitor applications.* Materials Letters, 2019. 236: p. 424-427.

32. Kasap, S., et al., *Superbat: battery-like supercapacitor utilized by graphene foam and zinc oxide (ZnO) electrodes induced by structural defects.* Nanoscale Advances, 2019. 1(7): p. 2586-2597.

33. Lee, K.S., C.W. Park, and J.D. Kim, *Synthesis of ZnO/activated carbon with high surface area for supercapacitor electrodes.* Colloids and Surfaces a-Physicochemical and Engineering Aspects, 2018. 555: p. 482-490.

34. Wei, J.S., et al., *Self-assembled ZnO-carbon dots anode materials for high performance nickel-zinc alkaline batteries.* Chemical Engineering Journal, 2021. 425.

35. Fahimi, Z. and O. Moradlou, *Fabrication of ZnO@C foam: A flexible free-standing electrode for energy storage devices.* Materials & Design, 2020. 189.

36. Ranjithkumar, R., et al., *Enhanced electrochemical studies of ZnO/CNT nanocomposite for supercapacitor devices.* Physica B-Condensed Matter, 2019. 568: p.51-59.

37. Kalpana, D., et al., *A novel high power symmetric ZnO/carbon aerogel composite electrode for electrochemical supercapacitor.* Electrochimica Acta, 2006. 52(3): p. 1309-1315.

38. Deka, B.K., et al., *Multifunctional enhancement of woven carbon fiber/ZnO nanotube-based structural supercapacitor and polyester resin-domain solid-polymer electrolytes.* Chemical Engineering Journal, 2017. 325: p. 672-680.

39. Luo, Q., et al., *Synthesis of ZnO tetrapods for high-performance supercapacitor applications.* Materials Letters, 2017. 198: p. 192-195.

40. Altaf, C.T., et al., *Photo-supercapacitors based on nanoscaled ZnO.* Scientific Reports, 2022. 12(1).

41. Pallavolu, M.R., et al., *Self-assembled and highly faceted growth of Mo and V doped ZnO nanoflowers for high-performance supercapacitors.* Journal of Alloys and Compounds, 2021. 886.

42. Ge, X.L., et al., *Metal-Organic Frameworks Derived Porous Core/Shell Structured* $ZnO/ZnCo_2O_4/C$ *Hybrids as Anodes for High-Performance Lithium-Ion Battery.* Acs Applied Materials & Interfaces, 2015. 7(48): p. 26633-26642.

43. Zhang, H., et al., *MOF-Derived ZnO Nanoparticles Covered by N-Doped Carbon Layers and Hybridized on Carbon Nanotubes for Lithium-Ion Battery Anodes.* Acs Applied Materials & Interfaces, 2017. 9(43): p. 37813-37822.

44. Zhang, Y.D., et al., *All-solid-state asymmetric supercapacitors based on ZnO quantum dots/carbon/CNT and porous N-doped carbon/CNT electrodes derived from a single ZIF-8/CNT template.* Journal of Materials Chemistry A, 2016. 4(26): p. 10282-10293.

45. Lee, G., Y.D. Seo, and J. Jang, *ZnO quantum dot-decorated carbon nanofibers derived from electrospun ZIF-8/PVA nanofibers for high-performance energy storage electrodes.* Chemical Communications, 2017. 53(83): p. 11441-11444.

46. Samuel, E., et al., $ZnO/MnO_x$ *Nanoflowers for High-Performance Supercapacitor Electrodes.* Acs Sustainable Chemistry & Engineering, 2020. 8(9): p. 3697-3708.

47. Kaftelen, H., et al., *EPR and photoluminescence spectroscopy studies on the defect structure of ZnO nanocrystals.* Physical Review B, 2012. 86(1).

48. Wang, J., et al., *Synthesis, properties and applications of ZnO nanomaterials with oxygen vacancies: A review.* Ceramics International, 2018. 44(7): p. 7357-7377.

49. Gurylev, V. and T.P. Perng, *Defect engineering of ZnO: Review on oxygen and zinc vacancies.* Journal of the European Ceramic Society, 2021. 41(10): p. 4977-4996.

50. Nadupalli, S., et al., *About defect phenomena in ZnO nanocrystals.* Nanoscale, 2021. 13(20): p. 9160-9171.

51. Han, N.S., et al., *Defect states of ZnO nanoparticles: Discrimination by time-resolved photoluminescence spectroscopy.* Journal of Applied Physics, 2010. 107(8).

52. Suri, A.K., et al., *Synthesis and consolidation of boron carbide: a review.* International Materials Reviews, 2010. 55(1): p. 4-40.

53. Rasim, K., et al., *Local Atomic Arrangements and Band Structure of Boron Carbide.* Angewandte Chemie-International Edition, 2018. 57(21): p. 6130-6135.

54. Emin, D., *Electronic transport in boron carbides.* AIP Conference Proceedings, 1986. 140(1): p. 189-205.

55. Werheit, H., *On excitons and other gap states in boron carbide.* Journal of Physics-Condensed Matter, 2006. 18(47): p. 10655-10662.

56. Libich, J., et al., *Supercapacitors: Properties and applications.* Journal of Energy Storage, 2018. 17: p. 224-227.

57. Balducci, A., et al., *A Guideline for Reporting Performance Metrics with Electrochemical Capacitors: From Electrode Materials to Full Devices.* Journal of the Electrochemical Society, 2017. 164(7): p. A1487-A1488.

58. Schneider, J.J., et al., *Synthesis, Characterization, Defect Chemistry, and FET Properties of Microwave-Derived Nanoscaled Zinc Oxide.* Chemistry of Materials, 2010. 22(7): p. 2203-2212.

59. Ruf, T., et al., *Competing effects between intrinsic and extrinsic defects in pure and Mn-doped ZnO nanocrystals.* Journal of Nanoparticle Research, 2016. 18(5).

60. Balci, O., et al., *Defect-induced* $B_4C$ *electrodes for high energy density supercapacitor devices.* Scientific Reports, 2021. 11(1).

61. Heian, E.M., et al., *Synthesis of dense, high-defect-concentration* $B_4C$ *through mechanical activation and field-assisted combustion.* Journal of the American Ceramic Society, 2004. 87(5): p. 779-783.

62. Betranhandy, E., N. Vast, and J. Sjakste, *Ab initio study of defective chains in icosahedral boron carbide* $B_4C$. Solid State Sciences, 2012. 14(11-12): p. 1683-1687.

63. Reddy, K.M., et al., *Atomic structure of amorphous shear bands in boron carbide.* Nature Communications, 2013. 4.

64. Mondal, S., et al., *Disorder and defects are not intrinsic to boron carbide.* Scientific Reports, 2016. 6.

65. Awasthi, A. and G. Subhash, *Deformation behavior and amorphization in icosahedral boron-rich ceramics.* Progress in Materials Science, 2020. 112.

66. Look, D.C., et al., *Electrical and optical properties of defects and impurities in ZnO.* Physica B-Condensed Matter, 2003. 340: p. 32-38.

67. Sokol, A.A., et al., *Point defects in ZnO.* Faraday Discussions, 2007. 134: p. 267-282.

68. Erhart, P., K. Albe, and A. Klein, *First-principles study of intrinsic point defects in ZnO: Role of band structure, volume relaxation, and finite-size effects.* Physical Review B, 2006. 73(20).

69. Xiong, G., U. Pal, and J.G. Serrano, *Correlations among size, defects, and photoluminescence in ZnO nanoparticles.* Journal of Applied Physics, 2007. 101(2).

70. McCluskey, M.D. and S.J. Jokela, *Defects in ZnO.* Journal of Applied Physics, 2009. 106(7).

71. Oba, F., et al., *Point defects in ZnO: an approach from first principles.* Science and Technology of Advanced Materials, 2011. 12(3).

72. Thévenot, F., *Boron carbide-A comprehensive review.* Journal of the European Ceramic Society, 1990. 6(4): p. 205-225.

73. Annenkov, M., et al., *Boron carbide nanoparticles for high-hardness ceramics: Crystal lattice defects after treatment in a planetary ball mill.* Journal of the European Ceramic Society, 2017. 37(4): p. 1349-1353.

74. Avcioglu, S., et al., *Processing and properties of boron carbide ($B_4C$) reinforced LDPE composites for radiation shielding.* Ceramics International, 2020. 46(1): p. 343-352.

75. Avcıoğlu, S., et al. (2021). Chapter 20 - Synthesis of nuclear-grade nano-sized boron carbide powders and its application in LDPE matrix composites for neutron shielding. In I.-M. Low & Y. Dong (Eds.), *Composite Materials* (pp. 543-579). Elsevier.

76. Vast, N., J. Sjakste, and E. Betranhandy, *Boron carbides from first principles.* 16th International Symposium on Boron, Borides and Related Materials (ISBB 2008), 2009. 176.

77. Ektarawong, A., et al., *First-principles study of configurational disorder in $B_4C$ using a superatom-special quasirandom structure method.* Physical Review B, 2014. 90(2).

78. Chang, Y.K., et al., *Application of hard ceramic materials $B_4C$ in energy storage: Design $B_4C$@C core-shell nanoparticles as electrodes for flexible all-solid-state micro-supercapacitors with ultrahigh cyclability.* Nano Energy, 2020. 75.

79. Kakiage, M., et al., *Synthesis of boron carbide powder in relation to composition and structural homogeneity of precursor using condensed boric acid-polyol product.* Powder Technology, 2012. 221: p. 257-263.

80. Bragg, W.L., *The diffraction of short electromagnetic Waves by a Crystal.* Scientia, 1929. 23(45).

81. Watts, J.L., et al., *Morphology control in high yield boron carbide.* Ceramics International, 2017. 43(2): p. 2650-2657.

82. Chen, X.W., et al., *Effect of glycerine addition on the synthesis of boron carbide from condensed boric acid-polyvinyl alcohol precursor.* Rsc Advances, 2016. 6(11): p. 9338-9343.

83. Wade, B., et al., *Synthesis and Characterization of Processable Polyborate Precursors.* Journal of Sol-Gel Science and Technology, 1995. 5(1): p. 15-25.

84. El-Sheikh, S.M., et al., *Influence of reaction temperature and time on nanoboron carbide morphology and its thermal stability, optical and electronic properties.* Journal of the Australian Ceramic Society, 2018. 54(3): p. 501-512.

85. Tahara, N., et al., *Effect of addition of tartaric acid on synthesis of boron carbide powder from condensed boric acid-glycerin product.* Journal of Alloys and Compounds, 2013. 573: p. 58-64.

86. Mondal, S. and A.K. Banthia, *Low-temperature synthetic route for boron carbide.* Journal of the European Ceramic Society, 2005. 25(2-3): p. 287-291.

87. Lamoreaux, R.H., D.L. Hildenbrand, and L. Brewer, *High-Temperature Vaporization Behavior of Oxides II. Oxides of Be, Mg, Ca, Sr, Ba, B, Al, Ga, in, Tl, Si, Ge, Sn, Pb, Zn, Cd, and Hg.* Journal of Physical and Chemical Reference Data, 1987. 16(3): p. 419-443.

88. Dacic, B.Z., et al., *Thermodynamics of gas phase carbothermic reduction of boron-anhydride.* Journal of Alloys and Compounds, 2006. 413(1-2): p. 198-205.

89. H. K. Clark, and J. L. Hoard, *The crystal structure of boron carbide.* Journal of the American Chemical Society, 1943. 65(11): p. 2115-2119.

90. Najafi, A., F. Golestani-Fard, and H.R. Rezaie, *Sol-gel synthesis and characterization of* $B_4C$ *nanopowder.* Ceramics International, 2018. 44(17): p. 21386-21394.

91. Pimenta, M.A., et al., *Studying disorder in graphite-based systems by Raman spectroscopy.* Physical Chemistry Chemical Physics, 2007. 9(11): p. 1276-1291.

92. Vast, N., et al., *Atomic structure and vibrational properties of icosahedral alpha-boron and $B_4C$ boron carbide.* Computational Materials Science, 2000. 17(2-4): p. 127-132.

93. Domnich, V., et al., *Boron Carbide: Structure, Properties, and Stability under Stress.* Journal of the American Ceramic Society, 2011. 94(11): p. 3605-3628.

94. Tallant, D.R., et al., *Boron-Carbide Structure by Raman-Spectroscopy.* Physical Review B, 1989. 40(8): p. 5649-5656.

95. Werheit, H., et al., *Optical Interband-Transitions of Boron-Carbide.* Physica Status Solidi B-Basic Solid State Physics, 1992. 172(2): p. K81-K86.

96. Ghosh, D., et al., *Strain-induced formation of carbon and boron clusters in boron carbide during dynamic indentation.* Applied Physics Letters, 2007. 91(6).

97. Kakazey, M.G., et al., *Electron paramagnetic resonance in boron carbide.* Journal of Applied Physics, 2002. 91(7): p. 4438-4446.

98. Chauvet, O., et al., *Spin susceptibility of boron carbides: Dissociation of singlet small bipolarons.* Physical Review B, 1996. 53(21): p. 14450-14457.

99. Janotti, A. and C.G. Van de Walle, *New insights into the role of native point defects in ZnO.* Journal of Crystal Growth, 2006. 287(1): p. 58-65.

100. Kappers, L.A., et al., *EPR and optical study of oxygen and zinc vacancies in electron-irradiated ZnO.* Nuclear Instruments & Methods in Physics Research Section B-Beam Interactions with Materials and Atoms, 2008. 266(12-13): p. 2953-2957.

101. Sancier, K.M., *Temperature dependence of the electron spin resonance spectra of zinc oxide powder.* The Journal of Physical Chemistry, 1972. 76(18): p. 2527-2529.

102. Yu, B.L., et al., *Electron spin resonance properties of ZnO microcrystallites.* Materials Letters, 1998. 33(5-6): p. 247-250.

103. Evans, S.M., et al., *Further characterization of oxygen vacancies and zinc vacancies in electron-irradiated ZnO.* Journal of Applied Physics, 2008. 103(4).

104. Hu, Y. and H.J. Chen, *Preparation and characterization of nanocrystalline ZnO particles from a hydrothermal process.* Journal of Nanoparticle Research, 2008. 10(3): p. 401-407.

105. Jakes, P. and E. Erdem, *Finite size effects in ZnO nanoparticles: An electron paramagnetic resonance (EPR) analysis.* Physica Status Solidi-Rapid Research Letters, 2011. 5(2): p. 56-58.

106. Koudelka, L., J. Horak, and P. Jariabka, *Morphology of Polycrystalline Zno and Its Physical-Properties.* Journal of Materials Science, 1994. 29(6): p. 1497-1500.

107. Wei, W.F., *$F^+$ center in ZnO.* Physical Review B, 1977. 15(4): p. 2250-2253.

108. Zhang, L.Y., et al., *Origin of Visible Photoluminescence of ZnO Quantum Dots: Defect-Dependent and Size-Dependent.* Journal of Physical Chemistry C, 2010. 114(21): p. 9651-9658.

109. Walters, A.B., et al., *Distinguishing surface and bulk electron charge carriers for ZnO powders.* Journal of Molecular Catalysis a-Chemical, 2000. 162(1-2): p. 287-295.

110. Werheit, H., *Present knowledge of electronic properties and charge transport of icosahedral boron-rich solids.* 16th International Symposium on Boron, Borides and Related Materials (Isbb 2008), 2009. 176.

111. Werheit, H., et al., *IR-Active phonons and structure elements of isotope-enriched boron carbide.* Journal of Solid State Chemistry, 2000. 154(1): p. 79-86.

112. Gogotsi, Y. and R.M. Penner, *Energy Storage in Nanomaterials - Capacitive Pseudocapacitive, or Battery-like?* Acs Nano, 2018. 12(3): p. 2081-2083.

113. Xiang, C.C., et al., *Reduced graphene oxide/titanium dioxide composites for supercapacitor electrodes: shape and coupling effects.* Journal of Materials Chemistry, 2012. 22(36): p. 19161-19167.

114. Wang, Y., et al., *$CeO_2$ nanoparticles/graphene nanocomposite-based high performance supercapacitor.* Dalton Transactions, 2011. 40(24): p. 6388-6391.

115. Bio-Logic Science Instruments. (2014). *Application Note #51: Supercapacitor characterization by galvanostatic polarization method*. [Brochure]. https://www.biologic.net/wp-content/uploads/2019/08/dc-characterizations_supercapacitor-an51.pdf

116. Gourdin, G., et al., *Investigation of the impact of stacking pressure on a double-layer supercapacitor.* Journal of Power Sources, 2011. 196(1): p. 523-529.

117. P. Simon, T. Brousse, & F. Favier, (2017). *Supercapacitors based on carbon or pseudocapacitive materials.* Wiley.

118. Toufani, M., et al., *Synergy of nano-ZnO and 3D-graphene foam electrodes for asymmetric supercapacitor devices.* Nanoscale, 2020. 12(24): p. 12790-12800.

119. Buldu-Akturk, M., O. Balci-cagiran, and E. Erdem, *EPR investigation of point defects in* $HfB_2$ *and their roles in supercapacitor device performances.* Applied Physics Letters, 2022. 120(15).

## APPENDIX

Table A1. Equivalent circuit parameters and corresponded circuit models used to fit the experimental data in Fig. 33.

| **Circuit Elements** | **SC1** | **SC2** |
|---|---|---|
| **R1** | 0.58 Ohm | 10.85 Ohm |
| **Q2/C2** | $46.44\text{x}10^{-6}$ F.$s^{(a2-1)}$ | $42.55\text{x}10^{-6}$ F |
| **a2** | 0.8157 | - |
| **R2** | 8,74 Ohm | 50,75 Ohm |
| **Q3** | $14.38\text{x}10^{-6}$ F.$s^{(a3-1)}$ | $28.76\text{x}10^{-6}$ F.$s^{(a3-1)}$ |
| **a3** | 0.82 | 0.66 |
| **R3** | 1,36 Ohm | 543,41 Ohm |
| **C4** | $0.18\text{x}10^{-3}$ F | - |
| **R4** | 12,28 Ohm | - |
| **Equivalent circuit:** | R1+Q2/R2+Q3/R3+C4/R4<br>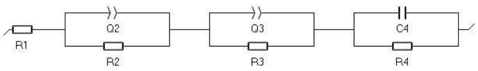 | R1+C2/R2+Q3/R3<br>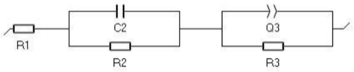 |

Table A2. Equivalent circuit parameters and corresponded circuit models used to fit the experimental data in Fig. 34.

| **Circuit Elements** | **SC3** | **SC4** |
|---|---|---|
| **R1** | 0.60 Ohm | 18.47 Ohm |
| **Q1/C1** | 5.18x10$^{-6}$ F.s$^{(a1-1)}$ | 45.37x10$^{-6}$ F |
| **R2** | 238,44 Ohm | 1.85x10$^{6}$ Ohm |
| **C3/Q3** | 23.83x10$^{-6}$ F | 1.32x10$^{-6}$ F.s$^{(a3-1)}$ |
| **a1/a3** | 0.8291 | 0.7964 |
| **R3** | 85,58 Ohm | 457.8 Ohm |
| **Q4** | - | 11.26x10$^{-6}$ F.s$^{(a4-1)}$ |
| **a4** | - | 0.709 |
| **R4** | - | 1,503 Ohm |
| **Equivalent circuit:** | R1+Q1/(R2+C3/R3)<br>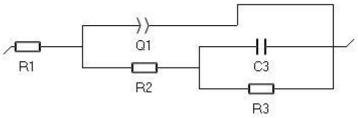<br> | R1+C1/R2/(Q3+R3)/(Q4+R4)<br>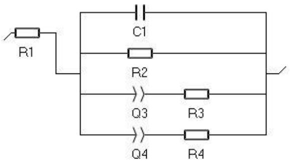<br> |

Table A3. Equivalent circuit parameters and corresponded circuit models used to fit the experimental data in Fig. 35.

| **Circuit Elements** | **SC5** | **SC6** |
|---|---|---|
| **R1** | 0.55 Ohm | 19.96 Ohm |
| **Q1/C1** | 22.66x10$^{-6}$ F.s$^{(a1-1)}$ | 0.32x10$^{-21}$ F |
| **R2** | 71,176 Ohm | 0.21x10$^{33}$ Ohm |
| **C3/Q3** | 0.11x10$^{-3}$ F | 9.63x10$^{-6}$ F.s$^{(a3-1)}$ |
| **a1/a3** | 0.7611 | 0.6127 |
| **R3** | 55,354 Ohm | 0.38x10$^{-15}$ Ohm |
| **Q4** | - | 13.29x10$^{-6}$ F.s$^{(a4-1)}$ |
| **a4** | - | 0.7029 |
| **R4** | - | 1,497 Ohm |
| **Equivalent circuit:** | R1+Q1/(R2+C3/R3)<br>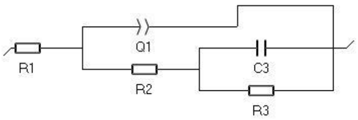 | R1+C1/R2/(Q3+R3)/(Q4+R4)<br>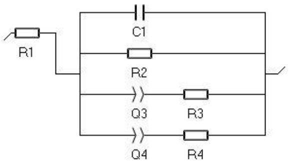 |

Table A4. Equivalent circuit parameters and corresponded circuit models used to fit the experimental data in Fig. 37.

| **Circuit Elements** | **ASC1** | **ASC2** |
|---|---|---|
| **R1** | 0.86 Ohm | 12 Ohm |
| **C1** | 33.88x10$^{-6}$ F | - |
| **C2** | - | 53.27x10$^{-6}$ F |
| **R2** | 105,499 Ohm | 1.913x10$^{6}$ Ohm |
| **C3** | 18.45x10$^{-6}$ F | 11.30x10$^{-6}$ F |
| **R3** | 69.81x10$^{9}$ Ohm | 238.9 Ohm |
| **C4** | 2.671x10$^{-6}$ F | - |
| **R4** | 103.3 Ohm | - |
| **Equivalent circuit:** | R1+C1/R2/(C3+R3)/(C4+R4)<br>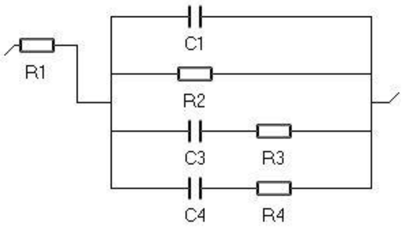 | R1+C2/R2+C3/R3<br>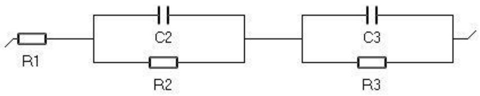 |

Table A5. Equivalent circuit parameters and corresponded circuit models used to fit the experimental data in Fig. 38.

| **Circuit Elements** | **ASC3** | **ASC4** |
|---|---|---|
| **R1** | 1.08 Ohm | 10.12 Ohm |
| **C1/C2** | $79.77 \times 10^{-6}$ F | $27.67 \times 10^{-6}$ F |
| **R2** | 260,554 Ohm | 566,727 Ohm |
| **C3** | $1.904 \times 10^{-6}$ F | - |
| **Q3** | - | $14.37 \times 10^{-6}$ F.s$^{(a3-1)}$ |
| **a3** | - | 0.768 |
| **R3** | 5.87 Ohm | 56.42 Ohm |
| **Q4** | $1.275 \times 10^{19}$ F.s$^{(a4-1)}$ | $3.301 \times 10^{-24}$ F.s$^{(a4-1)}$ |
| **a4** | 0.01518 | 0.4417 |
| **R4** | - | 86.69 Ohm |
| **Equivalent circuit:** | R1+C2/R2+C3/R3+Q4<br>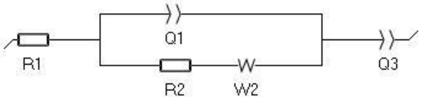 | R1+C1/R2/(Q3+R3)/(Q4+R4)<br>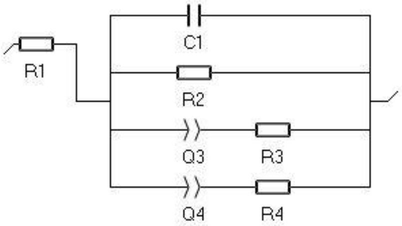 |

Table A6. Equivalent circuit parameters and corresponded circuit models used to fit the experimental data in Fig. 39.

| **Circuit Elements** | **ASC5** | **ASC6** |
|---|---|---|
| **R1** | 0.91 Ohm | 10.62 Ohm |
| **C1** | 0.91x10$^{-6}$ F | 1,347 F |
| **R2** | 364,189 Ohm | 20.42x10$^{15}$ Ohm |
| **Q3** | 41.02x10$^{-6}$ F.s$^{(a3-1)}$ | 0.50x10$^{-3}$ F.s$^{(a3-1)}$ |
| **a3** | 0.701 | 0.295 |
| **R3** | 7.44 Ohm | 37,333 Ohm |
| **C4/Q4** | 35.47x10$^{-6}$ F | 3.90x10$^{-6}$ F.s$^{(a4-1)}$ |
| **a4** | - | 0.8405 |
| **R4** | 1,024 Ohm | 32.96 Ohm |
| **Equivalent circuit:** | R1+C1/R2/(Q3+R3)+C4/R4<br>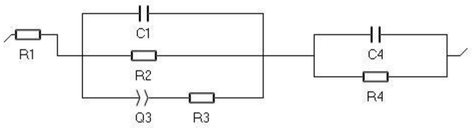 | R1+C1/R2/(Q3+R3)/(Q4+R4)<br>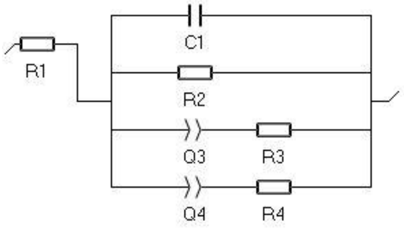 |